Current developments in laser ablation - inductively coupled plasma - mass spectrometry for use in geology, forensics, and nuclear nonproliferation research

by

Joshua D. Messerly

A dissertation submitted to the graduate faculty

in partial fulfillment of the requirements for the degree of

DOCTOR OF PHILOSOPHY

Major: Analytical Chemistry

Program of Study Committee:
R. S. Houk, Major Professor
Paul Spry
Patricia Thiel
Jacob Petrich
Hans Stauffer

Iowa State University

Ames, IA

TABLE OF CONTENTS

CHAPTER 1. INTRODUCTION 1

LA-ICP-MS 1
ICP-MS Instrumentation 2
Drawbacks of Solution Measurement 4
Laser ablation Instrumental Details 6
Applications of LA-ICP-MS 7
Dissertation Organization 8
References 10
Figures 13

CHAPTER 2. DISCRIPTION OF METAMORPHIC AND METASOMATIC PROCESSES AT THE BROKEN HILL LEAD-ZINC-SILVER DEPOSIT: RARE EARTH ELEMENT SIGNATURES OF GARNET-RICH ROCKS 15

Abstract 15
Introduction 16
Samples and Methods 24
Major, Metallic, and Rare Earth Element Studies 27
Discussion 31
Conclusions 41
Acknowledgments 41
References 42
Tables and Figures 54
Appendix 72

CHAPTER 3. ELEMENTAL ANALYSIS OF AUTOMOTIVE FILLER AND CAULK BY LASER ABLATION – INDUCTIVELY COUPLED PLASMA – MASS SPECTROMETRY AND PRINCIPAL COMPONENTS ANALYSIS FOR USE IN FORENSICS 74

Abstract 74
Introduction 74
Methods 76
Results and Discussion 77

Conclusions 80
Acknowledgements 81
References 82
Tables and Figures 83

CHAPTER 4. DETERMINATION OF URANIUM ISOTOPE RATIOS IN PARTICLE ENSEMBLES 94

Summary 94
Introduction 94
Experimental 97
Results and Discussion 100
Conclusions 103
Acknowledgements 104
References 104
Tables and Figures 106

CHAPTER 5. CONCLUSIONS 117

ACKNOWLEDGEMENTS 120

CHAPTER 1 - Introduction

Laser Ablation Inductively Coupled Plasma Mass Spectrometry

The inductively coupled plasma (ICP) has been used as both an emission source and an ion source for analytical instrumentation. It is an atmospheric pressure discharge produced by a radiofrequency (RF) power generator. Radiofrequency plasmas were studied extensively by Greenfield and associates [1], and Wendt and Fassel [2] in the 1960s. It was the work of Fassel and his co-workers [3] which brought the ICP into use as an emission source for multielement analysis in the early 1970s. The technique of ICP atomic emission spectroscopy (ICP-AES) is still a very widely used tool for elemental analysis.

The ICP as an emission source was useful, but the problem of spectral overlap reduced its utility for many elements and matrices. The high ion density in atmospheric plasmas gave rise their possible use as an ion source for mass spectrometry. The use of a DC discharge for the introduction of ions to mass spectrometry was investigated in the middle 1970's by Gray [4]. The use of the ICP as an ion source was investigated by Houk et al. [5]. By the early 1980's, it had been successfully developed into a technique for elemental analysis, inductively coupled plasma mass spectrometry (ICP-MS).

The ICP as an ion source has been successfully incorporated into instrumentation with a wide array of mass analyzers. Some of these instruments include quadrupole mass analyzers, double focusing magnetic sector-electrostatic sector mass analyzers, and time of flight mass analyzers. The versatility of ICP-MS instrumentation has made the technique widely used for elemental analysis. Many fields rely on ICP-MS as a reliable and sensitive method of elemental analysis. Some of these fields include geology, forensics, and environmental science. The

semiconductor industry uses ICP-MS in assessing the purity of silicon wafers used to produce computer chips.

The strengths of ICP-MS include high sensitivity, low detection limits, and a large dynamic range. Another advantage of ICP-MS is the ability to perform an analysis for multiple elements, almost simultaneously. The number of elements is governed by the mass analyzer and application. The use of ICP-MS for solution-based analysis has been successful due to these strengths.

ICP-MS Instrumentation

The ICP is usually formed using Ar gas. The Ar is made to flow through a torch that is made from three concentric tubes, usually made from quartz (Figure 1). The gas is sent through each of the tubes at different flow rates. The highest flow rate (usually around 15 L/min) is in the outer tube. This gas flow is responsible for sustaining the plasma and also for cooling the torch. The torch would melt without sufficient outer gas flow. The next tube contains a lower flow rate used to position the plasma and keep it from melting the innermost tube. This intermediate tube usually contains a flow rate of between 0.7 L/min and 1.5 L/min. The final tube is in the center of the torch. This tube usually contains the sample aerosol gas flow. This sample aerosol can be either nebulized liquid aerosols or particles from laser ablation. The flow rate is most often between 0.5 L/min and 3 L/min. It is optimized according to the specific instrument for the needs of the experiment being performed.

The plasma is produced in the Ar stream from the torch by a copper induction coil. This coil is attached to the RF generator. The generator provides a power of between 600 and 2000 watts to the load coil. The frequency of the generator is usually 27 MHz or 40 MHz. Some

systems use free running generators where the frequency is changed to adjust the impedance matching. The coil induces a current in the Ar stream, and the plasma is formed when the stream is seeded with electrons. The magnetic field produced by the load coil causes the electrons to be accelerated in circular orbits. A cascade of ionization produces the Ar plasma. Most of the energy supplied to the plasma is coupled into the outer induction region of the plasma. Heating of the induction region occurs due the large numbers of collisions at atmospheric pressure. The outer regions of the plasma can reach temperatures near 10,000 K. When the sample gas is introduced to the plasma, it creates a hole in the central channel of the plasma. The temperature in this center region reaches around 6000 K (Figure 1).

The sample gas carries either nebulized solution or laser ablation aerosols into this channel. As the gas carries the aerosol toward the plasma, the aerosol becomes desolvated if the sample is a nebulized solution. The aerosol is then vaporized and atomized. These atoms are ionized due to the presence of large numbers of high-energy free electrons in the plasma.

The ions produced by ICP-MS need be transferred to a mass analyzer. Mass analysis must be accomplished in a high vacuum of 10^{-6} to 10^{-8} Torr. Since the plasma is operated at atmospheric pressure, it must be sampled and the ions transferred to the vacuum region of the instrument. This is accomplished in steps using a differential pumping system. The plasma is sampled by a water cooled metal sampler cone with a circular orifice in its tip. The orifice is usually 1 mm in diameter. The area behind the sampler cone is pumped to a pressure of approximately 1 Torr. The sampled plasma undergoes a supersonic expansion in this region. The supersonic jet is itself sampled by another cone that usually has a smaller orifice than the sampler cone. The skimmer cone, as it is called, usually has an orifice of around 0.8 mm. The ions that make it through the interface are transmitted by ion lenses to the mass analyzer.

Drawbacks of Solution Measurement

Solution-based analysis has its limitations. The sample to be analyzed must usually be in a liquid form. Solid samples need to be dissolved or digested to form a solution before analysis. Due to the sensitivity of ICP-MS, the solutions created from these solid samples may need to be diluted before analysis. Samples are usually diluted and analyzed in a nitric acid solution. This sample preparation is time consuming and can introduce errors during the dissolution and dilution steps. Contamination is also a problem with sample dissolution as analytes may be present in the acids used to digest or dissolve the sample. The solvents used in the dilution step are also sources of contamination. These concerns sometimes require the use of expensive ultra-clean acids and containers which further add to the costs of analysis.

The drawbacks of the analysis of solid samples by solution measurements precipitated the study of other more direct methods of sample introduction for ICP-MS. One of these methods uses a laser to directly vaporize solid samples for transport into the ICP. The use of lasers as a sampling method for ICP-MS, called laser ablation inductively coupled plasma mass spectrometry (LA-ICP-MS) was studied starting in the mid 1980s. Laser ablation for sample introduction was first studied by Thompson et al. for use with ICP-AES [6] and later used with ICP-MS by Gray [7]. The use of laser ablation as a sample introduction method expanded throughout the 1990's.

One problem with this method of sample introduction is the need for matrix matched calibration standards for quantitative analysis. The amount of ablated material per shot varies by material based on its laser absorption characteristics. As the use of laser ablation increased, the amount of standards also increased. Solid calibration standards became better defined as to their

properties in relation to laser ablation. Becker [8], Aeschliman and Houk [9], and Guenther et al [10] investigated the use of nebulized liquid standards for quantification without the use of matrix matched solid standards.

Another problem with laser ablation is the issue of elemental fractionation when an element or several elements are not accurately represented in the data obtained from a laser ablation experiment. The element may be over or under represented. One reason for this is that some elements can be preferentially vaporized by the laser ablation event. Another cause of fractionation is the generation of large particles that are incompletely atomized and ionized in the plasma. Matrix matching can alleviate this problem, as both the sample and matrix matched standard may respond similarly to ablation.

Other ways to combat the problem are to move to shorter wavelength lasers, and to use lasers with homogenized radial beam profiles. The move to wavelengths farther into the UV, such as 266 nm and 193 nm, creates smaller particles due to the fact that the laser penetrates less into the sample. This increases the energy per unit volume. A larger amount of energy in a unit of volume causes less melting and recombination of particles. It also lessens the amount of large particles ejected from the surface. Vaporization is more thorough.

Homogenization of the beam profile creates a level energy profile across the beam surface. Beam homogenization was investigated by Guenther et al. [11] and a method for creating a level energy profile was created. A normal laser beam usually has a Gaussian radial energy distribution. The energy is greatest in the center of the beam, and is the least at the edge of the beam. This profile causes the center of the laser ablation crater to get more energy than the edges. This energy profile in turn promotes the problems of melting, recombination, and ejection of large particles discussed above. The Gaussian distribution of energy can combine

with the optics used to transmit the beam to the sample surface to create localized “hot spots” where the focusing of the optics creates a localized point of high laser energy. These “hot spots” exacerbate the problems associated with large particle formation. They also cause melting along the sides of the crater, which are then ablated by subsequent laser shots. The elemental composition of the melted material may have been changed.

Laser Ablation Instrumental Details

The usual use of laser ablation is the sampling of solids. Several different types of laser have been studied and developed for use in LA-ICP-MS. Some examples include excimer, solid-state Nd:YAG, and even gaseous CO_2 lasers. The applications of laser ablation that are presented later in this work use a Nd:YAG laser frequency quadrupled to 266 nm. This is one of the most common lasers used in LA-ICP-MS.

The laser beam in a laser ablation system is sent through optics to set the beam size and focus. The beam is focused on the sample surface, usually helped by a camera system. A diagram of a LA-ICP-MS apparatus is shown in Figure 2. In the most common setup, the sample is placed inside an enclosed ablation cell. The cell has a sample gas entrance port where Ar can flow into the cell. The Ar gas passes through the cell, over the sample, and then leaves via an exit port. The aerosol is then sent to the ICP. The cell is purged with Ar to keep the laboratory atmosphere from entering the cell. Once the cell is purged, the laser is fired onto the surface to create the sample aerosol. The laser beam can ablate at different points on the sample, usually by moving the ablation cell. Movement of the laser over a stationary sample would require more a more complex optical arrangement.

The laser is controlled from a computer where settings such as intensity, repetition rate, spot size, and ablation mode can be selected, depending on the system. Most systems have

several different ablation modes such as single spot, rastering, and trench ablation modes. The use of either ablating on a single spot or ablating a trench, or ablating in a pattern across the sample surface is dictated by the needs of the experiment. Adjustment of the laser ablation parameters mentioned above along with the choice of the ablation mode can greatly affect the rate of material removal. This is an important factor to consider in any analysis.

Applications of LA-ICP-MS

Analysis of Geological Samples by LA-ICP-MS

One of the major applications of LA-ICP-MS is in geology. The main advantage of laser ablation for geological work is the in situ, spatially resolved analysis that laser ablation provides. Specific areas of the material can be targeted and ablated without removing material from other areas that may not be of interest.

Another use of LA-ICP-MS in this field is to date materials using U-Pb ratios [12]. Inclusions in geological samples have been analyzed using laser ablation as the sampling method. Fluid inclusions are one of the varieties that have been investigated [13]. The laser is used to dig down to just above the inclusion. Then the laser ablates through the inclusion as the ICP-MS measures the elements of interest.

Forensic Uses of LA-ICP-MS

Forensic science is a field of study that tries to solve questions of interest to the legal system. Information is gained through the analysis of samples from crime scenes. One advantage of LA-ICP-MS in this field is the small amounts of material ablated for analysis. This leads to relatively non-destructive analysis of the sample. This is important in forensics as both

the defense and prosecution need to have access to evidence in a court case. It is also important if the item is valuable. The use of the technique to match evidence to a crime scene has been investigated. Materials such as glass [14], paint [15], and silver [16] have been investigated for matching purposes. Another matching application is authentication of items that may be antiques or have some other value.

Ratio Measurement in Particle Ensembles

The measurement of isotopic ratios in solid particulates is of interest in several fields such as environmental science, geology, and nuclear nonproliferation. Particulate ensembles can be individually separated, dissolved, and analyzed by solution based ICP-MS or thermal ionization mass spectrometry (TIMS) [17]. These methods are time consuming, labor intensive, and introduce the possibility of contamination. The small amounts of material in the particulate ensembles can cause results to be impacted by even small amounts of contamination. A spherical particle 100 μm in diameter only has a volume of 5.3×10^{-13} cm^3. This translates into a mass of 1.3×10^{-6} g of material in glass. If this particle was a NIST 610 glass standard with a nominal concentration of 500 ppm, it would contain 0.65 ng of analyte. This amount of analyte would produce a solution of only 0.65 ppb in 1mL total solution. Particles obtained from environmental sources may be even less concentrated.

The ability of LA-ICP-MS to look at solid samples directly with minimal or no sample preparation is of great advantage in analyzing particulate ensembles. If individual particles are to be resolved, some method must be found to fix them in place. The laser ablation event causes a shockwave in the solid which may propel particle ensembles other than the one targeted into

the sample gas. The shockwave travels through the solid and produces a trampoline effect on other particles.

One method of preparing particles for analysis is to press the particles into a pellet, with or without a binder. This method loses the ability to individually resolve the particles. Another method is to attach the particles to double-sided sticky tape. The particles are attached to the tape, which is then attached to the laser ablation stage. The problem with this method is that the adhesive and the tape itself are damaged by the laser. This can cause a loss of adhesion by particle ensembles other than the particle to be ablated. These unwanted particles can then be entrained in the sample gas. The ability to keep particles from other portions of the sample from becoming entrained in the sample aerosol is imperative when particles of interest are mixed with extraneous material.

Dissertation Organization

This dissertation is organized into chapters. These chapters focus on new applications of LA-ICP-MS. Chapters 2, 3, and 4 are scientific journal articles that are published or prepared for publication. Chapter 2 is a study of rare earth elemental profiles in garnets. These garnets are from the Broken Hill Deposit in New South Wales, Australia. The profiles in these garnets provide new information about the formation of this lead, nickel, and silver ore deposit which may be of use in exploration of new deposits. Chapter 3 is a forensics investigation of automotive putty and caulking material for possible use in the matching of evidence. A statistical method called Principal Components Analysis is used to interpret the data. The materials are investigated by manufacturer and lot number. Chapter 4 is an attempt to find new methods of fixing and analyzing individual particle ensembles. One method is to place the

ensembles onto a gelatin substrate. The other method investigated is to place the particles on filter paper and then coat them with collodion. The $^{235}U/^{238}U$ ratio is then determined in the particles selected for ablation. Enhancements to the ablation process are also studied. Chapter 5 is a conclusion section that contains a summary and directions for future research.

References

1. S. Greenfield, I.Ll. Jones, and C.T. Berry. High-pressure plasmas as spectroscopic emission sources, Analyst 89 (1964) 713-720.

2. R. H. Wendt, V. A. Fassel. Induction-coupled plasma spectrometric excitation source, Anal. Chem. 37 (1965) 920-2.

3. V. A. Fassel, R. N. Kniseley. Inductively coupled plasma. Optical emission spectroscopy, Anal. Chem. 46 (1974) 1110A-1111A, 1116A- 1120A.

4. A. L. Gray. Mass-spectrometric analysis of solutions using an atmospheric pressure ion source, Analyst 100 (1975) 289-99.

5. R. S. Houk, V. A. Fassel, G. D. Flesch, H. J Svec, A. L. Gray, C. E. Taylor. Inductively coupled argon plasma as an ion source for mass spectrometric determination of trace elements, Anal. Chem. 52 (1980) 2283-9.

6. M. Thompson, J. E. Goulter, F. Sieper. Laser ablation for the introduction of solid samples into an inductively coupled plasma for atomic emission spectrometry, Analyst 106 (1981) 32-9.

7. A. L. Gray. Solid sample introduction by laser ablation for inductively coupled plasma source mass spectrometry, Analyst 110 (1985) 551-6.

8. C. Pickhardt, J. S. Becker, H. J. Dietze. A new strategy of solution calibration in laser ablation inductively coupled plasma mass spectrometry for multielement trace analysis of geological samples, Fresen. J. Anal. Chem. 368 (2000) 173-81.

9. D. B. Aeschliman, S. J. Bajic, D. P. Baldwin, R. S. Houk. Spatially-resolved analysis of solids by laser ablation-inductively coupled plasma-mass spectrometry: trace elemental quantification without matrix-matched solid standards, J. Anal. At. Spectrom. 18 (2003) 872-7.

10. L. Halicz, D. Guenther. Quantitative analysis of silicates using LA-ICP-MS with liquid calibration, J. Anal. At. Spectrom. 19 (2004) 1539-1545.

11. M. Guillong, I. Horn, D. Guenther. Capabilities of a homogenized 266 nm Nd:YAG laser ablation system for LA-ICP-MS, J. Anal. At. Spectrom. 17 (2002) 8-14.

12. X. Xia, M. Sun, G. Zhao, H. Li, M. Zhou. Spot zircon U-Pb isotope analysis by ICP-MS coupled with a frequency quintupled (213 nm) Nd-YAG laser system, Geochem. J. 38 (2004) 191-200.

13. D. Guenther, A. Audetat, R. Frischknect, C. Heinrich. Quantitative analysis of major, minor, and trace elements in fluid inclusions using laser ablation-inductively coupled plasma mass spectrometry, J. Anal. At. Spectrom. 13 (1998) 263-270.

14. S. J. Bajic, D. B. Aeschliman, N. J. Saetveit, D. P. Baldwin, R. S. Houk. Analysis of glas fragments by laser ablation-inductively coupled plasma-mass spectrometry and principal component analysis, J. Fornesic Sci. 50 (2005) 1123-27.

15. A. L. Hobbs, J. R. Almirall. Trace elemental analysis of automotive paints by laser ablation-inductively coupled plasma-mass spectrometry (LA-ICP-MS), Anal. Bioanal. Chem. 376 (2003) 1265-71.

16. W. Devos, Ch. Moor, P. Lienemann. Determination of impurities in antique silver objects for authentication by laser ablation inductively coupled plasma mass spectrometry (LA-ICP-MS), J. Anal. At. Spectrom. 14 (1999) 621-626.

17. M. Wallenius, A. Morgenstern, C. Apostolidis, K. Mayer. Determination of the age of highly enriched uranium, Anal. Bioanal. Chem. 374 (2002) 379-84.

Figure 1

Diagram of an ICP Torch

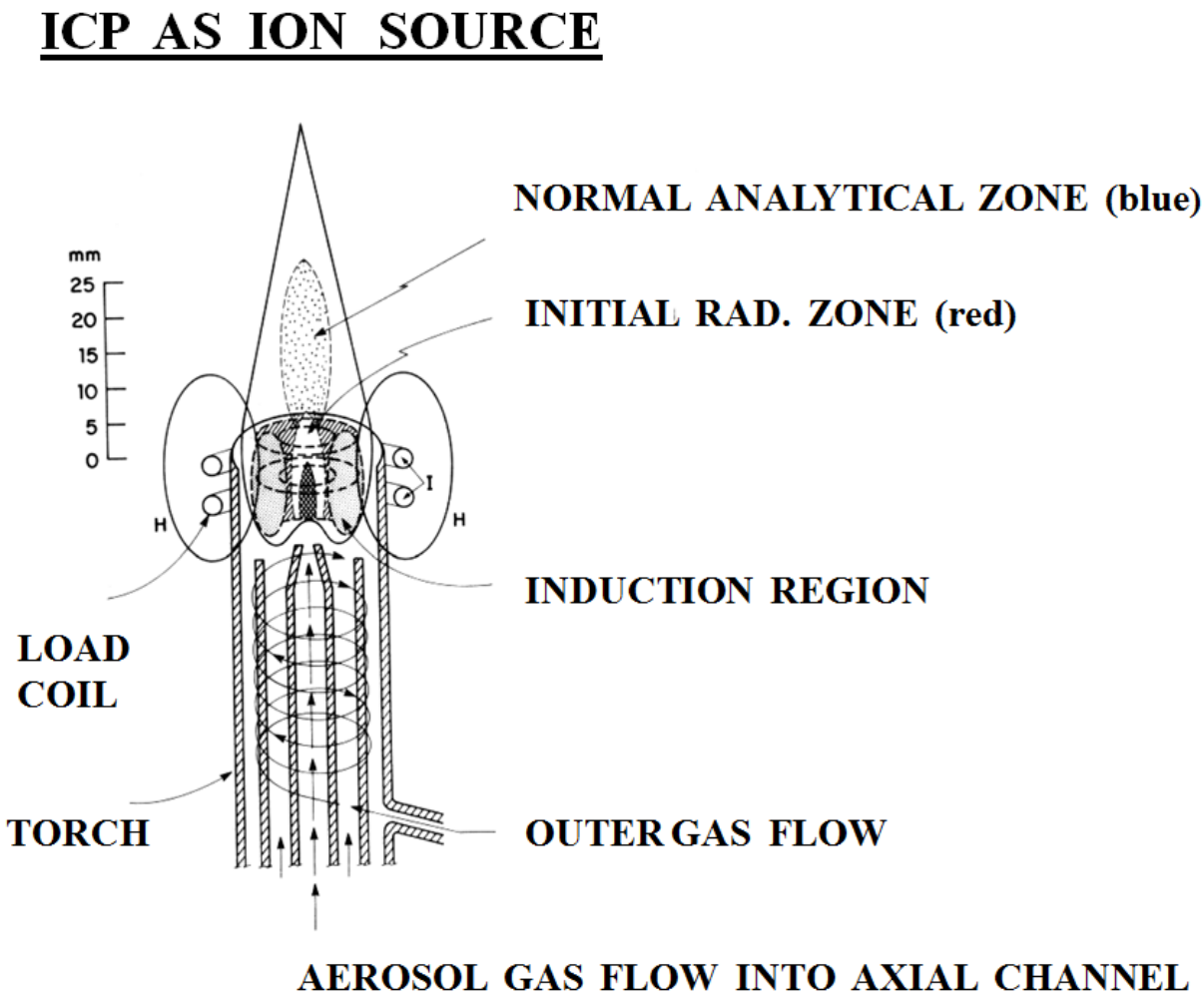

Figure 2

Experimental setup of LA-ICP-MS

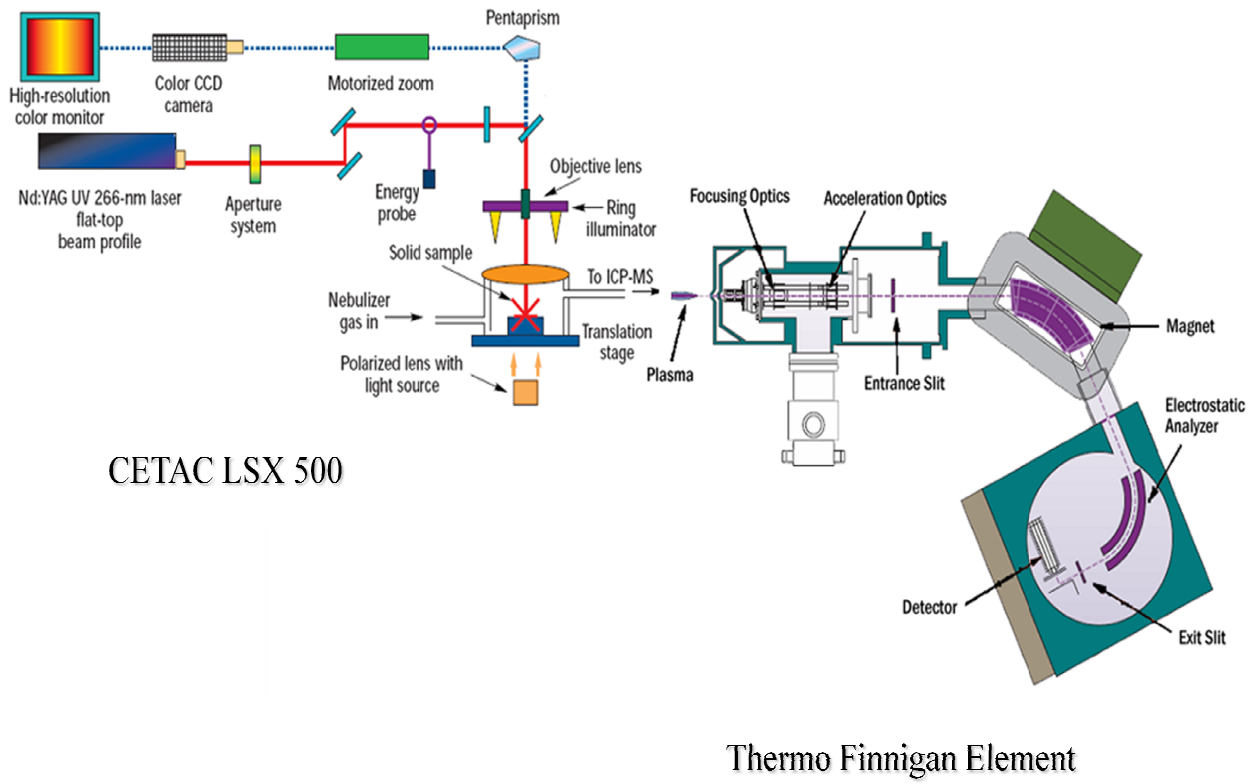

CHAPTER 2

Discrimination of Metamorphic and Metasomatic Processes at the Broken Hill Pb-Zn-Ag Deposit, Australia: Rare Earth Element Signatures of Garnet-Rich Rocks

A paper published in *Economic Geology*

Paul G. Spry, Adriana Heimann, Joshua D. Messerly, R. S. Houk

Abstract

Garnet occurs in a variety of rock types spatially related to the giant stratiform Paleoproterozoic Broken Hill lead-zinc-silver deposit, Australia. The deposit was metamorphosed to granulite facies conditions and subjected to at least five periods of deformation (D_1-D_5). Sulfides at Broken Hill are commonly associated with quartz garnetite, garnetite, and blue quartz gahnite-garnet rock (BQGGR). The origin of quartz garnetite and garnetite is controversial. Proposed models include: metamorphism of manganiferous sediments formed by submarine hydrothermal processes that mixed with aluminous pelagic sediments; metamorphism of an original detrital sediment; metasomatic mobilization of Mn between the sulfide lenses and the wall rocks either syn-peak (D_1-D_2) or post-peak metamorphism (D_3), and reaction of Mn derived from partially melted sulfide orebodies with the surrounding pelitic gneisses.

REE patterns of whole-rock samples of garnetite and quartz garnetite show high light rare earth element/heavy rare earth element (LREE/HREE) ratios. Chondrite-normalized REE patterns, based on analyses of garnet in garnetite and quartz-garnetite and some samples of BQGGR using laser ablation-inductively coupled plasma-mass spectrometry (LA-ICP-MS) techniques generally show very low LREE/HREE ratios, flat HREE signatures, and low overall REE contents (< 100 ppm). HREEs are incorporated in garnet, whereas LREEs likely occur in intergranular material between garnet grains and in monazite, zircon, and apatite inclusions in garnet or along grain boundaries. Garnetite and fine-grained quartz garnetite show positive and negative Eu anomalies, respectively. Coarse metasomatic garnet

surrounding D_3 quartz veins, and metasomatic garnet in quartz garnetite halos around lead-rich orebodies, remobilized quartz garnetite and some BQGGR, show positive and negative Eu anomalies, variable HREEs, low to moderate LREE/HREE ratios, and arcuate patterns. The REE signature of garnet in garnetite and quartz garnetite is characteristic of metamorphic garnet with Eu anomalies reflecting relative inputs of detrital to hydrothermal components in a premetamorphic protolith, fO_2 conditions and temperature, whereas arcuate HREE signatures are characteristic of metasomatic garnet that formed post-peak metamorphism. The REE chemistry of garnet is consistent with mineralogical, petrological and structural studies that demonstrate garnetite and quartz garnetite are metamorphosed sediments that formed by submarine hydrothermal processes.

Introduction

The stratiform Paleoproterozoic Broken Hill deposit, located in the Broken Hill Domain of the Curnamona Province, Australia, is the largest accumulation of lead-zinc-silver mineralization in the world (280 million tons at 10% Pb, 8.5% Zn, and 148 g/t Ag) (Fig. 1). It is spatially associated with a wide variety of rock types, the most common being the so-called “lode horizon” rocks that consist of quartz garnetite, garnetite, blue quartz-gahnite ($ZnAl_2O_4$) lode, and lode pegmatite (Johnson and Klingner, 1975). These rocks are also spatially associated with over 400 minor Broken Hill-type (BHT) deposits throughout the Curnamona Province and constitute a primary empirical exploration tool for ores of this type (Barnes et al., 1983). Despite the obvious spatial relationship of these rock types to sulfide mineralization, their origin is steeped in controversy, and the way these rocks can be used as exploration guides to BHT deposits in the Curnamona Province is yet to be determined. However, exploration criteria are, in part, dependent on our knowledge of how these rocks formed.

Several models have been proposed to explain the origin of quartz garnetite and garnetite in the main Broken Hill lode. These include (1) metamorphism of manganiferous exhalites mixed with aluminous pelagic sediments (e.g., Richards, 1966; Stanton, 1976b; Plimer, 1984; Wiggins, 1988; Spry and Wonder, 1989; Lottermoser, 1989; Parr, 1992; Spry et al., 2000), (2 metamorphism of an original manganiferous detrital sediment (e.g., Segnit, 1961; Haydon and McConachy, 1987; Wright et al., 1987; Webster, 2006), (3) metasomatic movement of Mn from the sulfide orebodies into the aluminous wall rocks (e.g., Henderson, 1953; O'Driscoll, 1953; Stillwell, 1959; Hodgson, 1975; Prendergast et al., 1998), and (4) a reaction between Mn derived from partially melted orebodies with the surrounding pelitic gneisses (Frost et al., 2002; Mavrogenes et al., 2004). Wright et al. (1987) proposed that garnet-quartz rocks were originally high energy, detrital manganiferous sands, which acted as host for the mineralizing fluids. Hodgson (1975) suggested that the metasomatic event occurred during the granulite-grade metamorphic event, whereas Prendergast et al. (1998) suggested that the event was syn- to late-tectonic.

As a way to understand the origin of the garnet-rich rocks, bulk-rock rare earth element (REE) studies of quartz garnetite, garnetite, and blue quartz gahnite rocks in the Broken Hill Domain, including at the Broken Hill deposit, were conducted by Lottermoser (1989), and by Parr (1992) on the second largest BHT deposit, the Pinnacles deposit. Rare earth element analyses of individual garnets in garnetite from the Broken Hill lode were obtained by Lottermoser (1988) and Wiggins (1988) using instrumental neutron activation analyses (INAA), whereas secondary ion mass spectrometry (SIMS) analyses of REEs were obtained by Schwandt et al. (1993).

On the basis of bulk-rock REE studies of garnetite, quartz garnetite, quartz-gahnite rock, and feldspar-, calcite-, and magnetite-rich lithologies, proximal (i.e. intimately associated with base metal ore) and distal to the Broken Hill deposit (i.e., greater than several hundred meters), Lottermoser (1989) proposed that these rocks were isochemically metamorphosed exhalites. Lottermoser showed that meta-exhalites proximal to BHT mineralization, including the main Broken Hill lode, are enriched in light

REEs (LREE: La to Sm) and Eu similar to what is observed for metalliferous sediments and hydrothermal fluids from the Red Sea and East Pacific Rise (Courtois and Treuil, 1977). He also argued that meta-exhalites distal to BHT mineralization exhibited LREE and heavy REE (HREE: Gd to Lu) enrichments, as well as negative Eu and Ce anomalies. However, Lottermoser's (1989) study was limited in scope because he only analyzed five samples of exhalite proximal to the Broken Hill orebodies and three samples of sulfide ore. The remaining ten samples analyzed were of exhalites distal to the Broken Hill deposit. It should be noted that Wright et al. (1993) questioned the proximal versus distal classification of samples Lottermoser (1989) and suggested that some of the samples classified as distal should be considered proximal, whereas others described as proximal should be considered distal. Wright et al. (1993) specifically noted that several of the samples considered in Lottermoser (1989), although distal to the Broken Hill ores, were proximal to other sulfide locations along the main Line of Lode.

Parr (1992) analyzed 28 samples of garnetite, quartz-garnetite, sulfide-rich garnet-gahnite-bearing rocks and unmineralized metapelite spatially associated with the Pinnacles deposit, located 15 km southwest of Broken Hill. She found that quartz garnetite and garnetite in the footwall to the sulfide zones possess negative Eu anomalies and steep LREE-enriched patterns, whereas similar rocks in the hanging wall to the ores exhibit zero or positive Eu anomalies and less LREE-enriched patterns. Heavy rare earth element concentrations are fairly uniform in these rocks across the deposit, but they may be depleted in some samples. The metapelite is slightly enriched in LREE and shows negative Eu anomalies. Although their REE patterns are generally flat, some samples showed slight HREE depletions. Parr (1992) considered all of these rocks, except for the pelites, to be meta-exhalites. She suggested that the variations in REE patterns are stratigraphically related and were due to fluctuations in REE concentrations in the primary exhalative fluids. These fluctuations were apparently produced by variations in the temperature and fO_2 of the exhalative fluid.

Secondary ion mass spectrometry studies by Schwandt et al. (1993) of the REE content of garnet in four samples of garnetite proximal and distal to the Broken Hill deposit showed that garnet has low LREE and high HREE contents, typical of garnet in metamorphic terranes elsewhere (e.g., Hickmott et al., 1987; Schwandt et al., 1996). Garnet located proximal to sulfide mineralization showed positive Eu anomalies whereas garnet in a single distal sample exhibited a negative Eu anomaly. These patterns contrast with those obtained by Lottermoser (1988) and Wiggins (1998) for garnet in garnetite from the deposit. The garnets analyzed by Lottermoser (1988) and Wiggins (1988) show LREE enrichment and overall patterns similar to those of the bulk-rock REE analyses of garnetite obtained by Lottermoser (1989). Schwandt et al. (1993) attributed the difference between the patterns obtained in their study and those determined by Lottermoser (1988) as being due to the way Lottermoser prepared his samples for analysis. Lottermoser (1988) measured the REE content of individual garnets using INAA after they had been leached in 2 M HCl. Schwandt et al. (1993) deduced that the elevated LREE values obtained by Lottermoser were the result of the incomplete removal of LREE-enriched grain boundary material or intergranular film from the surface of garnet. A transmission electron microscopy investigation of this intergranular material by Schwandt et al. (1993) showed that it consisted of a gel-like phase with a composition similar to garnet that also contained S, Cu, and Zn, as well as chlorite, potassium and sodium chlorides, and a titanium-rich phase. Qualitative SIMS analysis of this material by Schwandt et al. (1993) revealed that it had very high LREE/HREE ratios.

Highly precise in-situ REE analysis of garnet by laser ablation-inductively coupled plasma mass spectrometry in several studies (e.g., Jackson et al., 1992; Norman et al., 1996; Prince et al., 2000), coupled with the limited number of SIMS data obtained by Schwandt et al. (1993) (rim and centers of one garnet each in four garnetite samples only), prompted a more comprehensive LA-ICP-MS study of garnet in garnet-rich rocks from the Broken Hill deposit. The REE data obtained from individual garnet analyses are coupled with thirty-five new whole-rock analyses of garnet-rich rocks in and adjacent to the Broken

Hill orebodies (i.e., proximal, using the terminology of Lottermoser, 1989) to provide information concerning the origin of garnet and its host rock, and to attempt to identify a REE fingerprint for garnet-rich rocks and individual garnets in and adjacent to ore that can be used as an exploration guide for BHT mineralization in the Curnamona Province and elsewhere.

Geology of the Broken Hill Deposit

The Broken Hill deposit occurs in the Broken Hill Domain of the Paleoproterozoic to Mesoproterozoic southern Curnamona province (Page et al., 2005a, b). Geochronological studies by Page et al. (2005b) suggest a temporal correlation between rocks in the Curnamona province and those spatially associated with the Carpentaria zinc belt in northern Australia, which hosts the Mount Isa and McArthur River base metal deposits. It has been proposed by, for example, Giles et al. (2002) that the Mt. Isa and Curnamona provinces were once adjacent to each other. White et al. (1995, 1996) suggested that the Broken Hill Domain formed part of a fold and thrust belt but this has met with some opposition (e.g., Stevens, 1996). The Broken Hill deposit occurs in a distinctive suite of metamorphosed rocks in the Broken Hill Group within the Willyama Supergroup (7-9 km thick), which consists of psammopelites, pelites, psammites, mafic and quartzofeldspathic rocks, and chemical sediments (Fig. 1) (Willis et al., 1983; Parr and Plimer, 1993). The package of rocks at Broken Hill has been interpreted as forming in an epicontinental basin or an intracontinental rift (Parr and Plimer, 1993; Page et al., 2005a).

The Hores Gneiss, which hosts the Broken Hill deposit, is constrained to an age of 1685 ± 3 Ma (Page et al. 2005a). The generally accepted view is that the Broken Hill Domain and the Broken Hill deposit underwent at least three periods of deformation (D_1, D_2, and D_3) (Laing et al., 1978; Willis et al., 1983; Gibson, 2000), with five periods of deformation (D_1-D_5) being reported by Plimer (2006). D_1 is manifested as a penetrative schistosity and as rare isoclinal folds (Laing et al., 1978). D_2 and D_3 fabrics,

which are inseparable within the interval 1597 ± 3 to 1591 ± 5 Ma (Page et al., 2005a), are related to the development of mesoscopic folds. Folds associated with D_3 are coaxial with D_2 folds and are most prominent adjacent to major D_3 shear zones. In the Broken Hill area, peak metamorphic conditions reached granulite facies at approximately 780°-800°C and 5-6 kb (Phillips, 1980; Phillips and Wall, 1981), although P-T conditions greater than 850°C and 5-7 kb were proposed by Frost et al. (2005) for an area 5 km east of the mine area. Retrograde metamorphic minerals associated with D_3, formed at approximately 550°-600°C and 5.0-5.5 kb (Phillips, 1980; Stevens, 1986; Plimer, 2006)

The Broken Hill deposit is 7 km long and consists of six separate orebodies (the A, B, and C lodes and the 1, 2, and 3 lenses), with some orebodies being sub-divided into at least two massive sulfide lenses. Sulfide ores consist primarily of argentiferous galena and sphalerite with lesser pyrrhotite, chalcopyrite, and arsenopyrite. Each orebody possesses a characteristic metal (Pb, Zn, and Ag) content and gangue mineralogy, consisting predominantly of various combinations of quartz, garnet, gahnite, fluorite, calcite, rhodonite, bustamite, hedenbergite, and apatite. The A, B, and C lodes and the 1 lens are generally enriched in Zn, Cu, and Ca, whereas the 2 and 3 lenses contain higher proportions of Pb, Ag, and Mn (Johnson and Klingner, 1975; Plimer, 1984). Laing et al. (1978) suggested that the orebodies were overturned during deformation and that the Pb-rich lodes (Pb>Zn) lie stratigraphically above the Zn-rich lodes (Zn>Pb) (Fig. 2). Over the strike length of 7 km the orebodies are stratiform, but locally the ore zones can be either stratiform, stratabound or controlled by D_1, D_2, D_3 or later events. It is relevant to the present study to note that the C lode and, in places, the B lode are characterized by broad (up to 150m by 400m) stratabound blue quartz-gahnite stringer mineralization that has an apparent crosscutting relationship to stratigraphy. In places, the C lode appears to be located in the axial plane of D_2 folds. However, recent structural studies by Webster (2006) proposed that the C lode represents the structurally offset and attenuated distal end of B lode. For the purposes, of the present study the two sulfide zones will be referred to as the B and C lodes.

The origin of the Broken Hill deposit remains in doubt due to the granulite facies metamorphism that has affected the ore, recrystallization of the ore, and the resultant lack of primary sulfide depositional textures (Large, 2003). Models for the genesis of the deposit include metamorphism of a syngenetic, stratiform volcanic-exhalative sea floor deposit (Stanton, 1976a; Parr and Plimer, 1993), compactive expulsion of metal-bearing brines during accumulation of a thick sedimentary pile and subsequent metamorphism (Haydon and McConachy, 1987; Wright et al., 1987), metamorphism of a synsedimentary or syndiagenetic ore deposit (Large, 2003), syntectonic introduction of metals during peak metamorphism (Ehlers et al., 1996; Nutman and Ehlers, 1998; Rothery, 2001; Gibson and Nutman, 2004), and a magmatic-hydrothermal model in which ore-bearing fluids and metals were derived from concordant Fe-rich tholeiites (Crawford, 2006).

The Pinnacles BHT deposit was metamorphosed to granulite facies and was considered by Parr (1992) to be located in the Cues Formation, approximately 700 m stratigraphically below the Broken Hill deposit. Approximately 2 Mt of base metal sulfides in the main stratabound lead lode (average grade of 6 to 11% Pb; 2.5 % Zn, 300-500 g/t Ag and approximately 1 % Pb, 10-15 % Zn, and 30 g/t Ag) in three small zinc lodes have been mined (Parr, 1994). The ore is hosted in a sequence of metapelites interbedded with psammopelites, quartz garnetite, garnetite and quartz-gahnite rocks.

Garnet-Rich Rocks associated with the Broken Hill Orebodies

Three types of garnet-rich rock are recognized at Broken Hill (Johnson and Klingner, 1975; Spry and Wonder, 1989; Plimer, 2006) and were termed quartz-garnetite, garnetite, and garnet envelope by Spry and Wonder (1989), with quartz-garnetite being by far the most common of the three rock types. A detailed discussion of the garnet composition, mineralogy, texture, and the spatial relationship of these

rocks to the ore is given in Spry and Wonder (1989) and Plimer (2006), and is only briefly summarized here.

Quartz-garnetite consists of massive or laminated rocks that contain between 10 and 80% garnet with varying amounts of several minerals including quartz, biotite, apatite, gahnite, sphalerite, pyrrhotite, plagioclase, orthoclase, hedenbergite, and wollastonite. Quartz-garnetite is spatially associated with all orebodies but is most abundant in and adjacent to the 2 and 3 lenses. This rock may extend for hundreds of meters with laminations between 0.2 and 10 cm thick that parallel bedding (S_0) and the first foliation (S_1). Laminae are defined by alternations of garnet and quartz, garnet and sulfide, variations in the color and size of garnet, and alternations of garnet with other silicates (Fig. 3a). At least seven different varieties of quartz-garnetite were identified by Spry and Wonder (1989) and distinguished on the basis of mineralogy. It is noted here that the "quartz-gahnite garnetite" of Spry and Wonder (1989) is present in and adjacent to sulfides in B and C lodes where it grades into a more abundant blue quartz-gahnite rock. These rocks are massive and parallel S_0, S_1, and S_2. One particular variety of massive quartz-garnetite, which Spry and Wonder (1989) termed "remobilized quartz-garnetite" consists of coarse spessartine garnet, up to 1 cm in diameter, and quartz that cross-cut massive and laminated varieties of quartz-garnetite and garnetite (Fig. 3b). This rock type probably formed during D_3.

Garnetite is a metamorphic rock that contains >80% by volume of orange-brown and pink garnet (Fig. 3b). It occurs mainly on the margins of the 1, 2, and 3 lenses and the A lode, as pods or blocks in ore, and stratigraphically along strike from ore. Furthermore, it can grade into quartz-garnetite (Fig. 3c). Garnetite is finely laminated with laminae up to 3 mm thick defined by alternations between garnet and quartz and different colors and sizes of garnet. Plimer (2006) described the laminations as being mostly parallel to S_0 and S_1, but in places garnetite contains chaotic folds unrelated to these schistosities. Garnetite and quartz garnetite consist of many of the same minerals and both possess granoblastic textures (Figs. 3c, d).

A garnet envelope occurs on the margins of Pb-rich orebodies as garnet stringers discordant to S_0 and S_1, generally parallel to S_3, or it surrounds D_3 quartz and quartz-fluorite veins that cross-cut massive quartz garnetite (Fig. 3e). Garnet in these garnet envelopes is generally orange-brown in color, but can be red, and is coarse-grained (up to 1 cm in diameter). The garnet envelopes formed during D_3 and superficially resembles the remobilized quartz garnetite described by Spry and Wonder (1989).

Samples and Methods

Samples were collected from underground locations at the former North Broken Hill (now Perilya's North mine), and the Zinc Corporation and New Broken Hill Consolidated mines (now Perilya's Southern Operations) and are documented in Spry (1978). These samples have been supplemented by drill core from the Southern Operations and CIML7, surface samples from CIML7, and from the collection of Steve Scott (University of Toronto). A summary of sample location, rock type, and mineralogy is given in Table 1, and sample locations are also shown in Figure 4. Polished and polished-thin sections of garnet-rich rocks were examined with an Olympus BX-60 dual reflected-transmitted light microscope and the back-scattered electron (BSE) mode of a Hitachi S 2460 reduced vacuum scanning electron microscope (SEM) at Iowa State University (ISU), at an accelerating voltage of 20 kV. Electron probe microanalyses (EPMA) of garnet were obtained at the University of Minnesota, using a JEOL 8900 Electron Probe Microanalyzer at an accelerating voltage of 15 kV and a beam current of 20 nA, using a range of mineral standards including pyrope (Si, Al, Mg), hornblende (Ti), ilmenite (Fe), spessartine (Mn), and apatite (Ca). The composition of garnet in some samples was reported

previously by Spry and Wonder (1989), in which details of the operating conditions of the electron microprobe for their study are given.

Major elements (SiO_2, Al_2O_3, Fe_2O_3, CaO, MgO, Na_2O, K_2O, MnO, TiO_2, P_2O_5, Cr_2O_3, LOI) of whole-rock samples were determined following $LiBO_2$ fusion and measured by ICP-AES techniques. C and S were measured by LECO analysis, and rare earth elements (La, Ce, Pr, Nd, Sm, Eu, Gd, Tb, Dy, Ho, Er, Tm, Yb, Lu) and Ba were obtained following $LiBO_2$ fusion and measured by ICP-MS techniques at Acme Analytical Laboratories (AAL). Base metal (Cu, Pb, and Zn) compositions were obtained by dissolving the sample in aqua regia and analyzing with an ICP-MS. Standards used by AAL were accurate to within ±5 ppm for the trace elements and to within ±2 percent for major elements.

Laser ablation-inductively coupled plasma-mass spectrometry (LA-ICP-MS) analyses of garnet were carried out using a CETAC LSX-500 laser ablation module coupled to a ThermoFinnigan ELEMENT1 ICP-MS instrument at ISU and an Agilent 7500 laser ablation system interfaced with a Merchantek EO-UV laser ablation system at Macquarie University, Sydney. The CETAC laser ablation module is equipped with a Q-switched Nd:YAG laser, frequency quadrupoled to 266 nm. Samples were ablated with 100 shots at a pulse energy of 6.3 mJ, a repetition rate of 2 Hz, and a spot diameter of 100 μm. A time-resolved plot of signal for each element was integrated and concentrations computed using Geopro software by CETAC. Operating conditions for the ThermoFinnigan ICP-MS instrument were: low resolution, power (~1200 W), and sample gas flow rate (~1.3 l/min Ar) adjusted to maximize atomic ion signal. The Merchantek instrument uses a Quantel Nd:YAG laser, frequency quadrupoled to 266 nm. Samples were ablated with a 100 shots at a pulse energy of 1 mJ, a repetition rate of 5 Hz, and a spot diameter of ~50 μm. An internal standard (^{43}Ca) was used for both instruments for CaO concentrations of >1wt. % CaO. For the Merchantek EO-UV laser ablation system for CaO concentrations of <1wt. %

CaO, ^{27}Al was used as the internal standard. NIST 610 glass (Pearce et al., 1997) was used an external standard for both instruments, and Mongolian garnet MU5388 (Norman et al., 1996) and USGS basaltic glass standard (BCR2g) were used as internal standards for the instrument at Macquarie University. The carrier gas for the LA system at ISU was Ar, whereas at Macquarie University a mixture of He and Ar was used. The raw ICP-MS data for the Macquarie instrument were exported in ASCII format and processed using GLITTER! (van Achterberg et al., 2001), an in-house data reduction program.

The REE data were normalized to chondrite values after McDonough and Sun (1995) rather than a shale standard such as Post-Archean Australian Shale (PAAS). The main reason for doing this is that all previously published REE plots of garnet-rich rocks in the southern Curnamona Province (Lottermoser, 1988, 1989; Wiggins, 1989; Parr, 1992; Spry et al., 2000; Schwandt et al., 1993) were normalized to chondrite and it is easier to make comparisons with these data. Furthermore, there is still considerable debate concerning the origin of virtually all rock types in the Broken Hill area (i.e. sedimentary protoliths versus igneous protoliths), and the source of the ore-forming components. For example, Plimer (1985) argued that the ore-forming components were derived from mantle metasomatism, which supports the contention that the REE data should be plotted relative to chondrite rather than PAAS. Moreover, the REE compositions of quartz garnetites that appear in the literature from worldwide localities are almost always normalized to chondrite regardless of the host rocks (see Spry et al., 2000 and references therein).

Major, Metallic and Rare Earth Element Studies

Major, metallic and rare earth element compositions of garnet-rich rocks

Major, metallic (Cu, Pb, Zn, and Ba), and rare earth element compositions were obtained from 35 samples (11 garnetites, 8 massive and laminated quartz-garnetites, 7 remobilized quartz garnetites and garnet envelopes, 7 garnet-gahnite-quartz rocks from the B and C lodes, one hedenbergite garnet rock, and one sillimanite gneiss) (Table 2). For all but three of the 11 samples of garnetite (Kintore 3, 532-139, and Blackwood 4), the REE patterns for whole-rock samples of garnetite are enriched in chondrite-normalized LREEs and depleted in HREEs (Fig. 5a). Seven of the remaining eight samples show positive Eu anomalies (Eu/Eu* = 1.47 to 5.12) whereas samples 532-117, 532-139, and Kintore 3, exhibit negative Eu anomalies (Eu/Eu* = 0.11 to 0.49). Samples Kintore 3, 532-139, and Blackwood 4 show relatively flat REE patterns and are not enriched in LREEs. A hedenbergite-garnet rock (sample 532-285) also exhibits a flat REE pattern and a very weak positive Eu anomaly (Eu/Eu* = 1.09) (Fig. 5b).

Like most samples of garnetite, samples of the sillimanite gneiss (532-222B) that occurs adjacent to the Broken Hill orebody (Fig. 5b), laminated and massive quartz garnetite (Fig. 5c), remobilized quartz garnetite and garnet envelopes (Fig. 5d) are enriched in LREEs and depleted in HREEs. These garnet-bearing rocks can show positive or negative Eu anomalies and there does not appear to be any significant correlation between the nature of the Eu anomaly and the sulfur or base metal content of the sample. Some samples contain several percent S and >1% combined Cu+Pb+Zn and have negative or positive Eu anomalies.

Although the REE patterns of blue quartz-garnet-gahnite rocks from the B and C lodes superficially resemble those of other garnet-bearing rocks in and adjacent to the Broken Hill deposit, they all have prominent negative Eu anomalies (Eu/Eu* = 0.13-0.43) and flat HREE patterns (Fig. 5e). Several other garnet-bearing samples also have flat HREE values, but many show a gradual decrease or

increase in the normalized HREE values for elements heavier than Gd. The Ce/Ce* values for all garnet-bearing rocks range from 0.87 to 1.18, which indicates that they possess only weak Ce anomalies.

Major element compositions of garnet in garnet-rich rocks

Although there are exceptions, electron microprobe analyses show that garnets from garnetite and quartz garnetite from the 2 and 3 lenses are generally enriched in the grossular and spessartine components, respectively whereas those from the A lode show both elevated spessartine and grossular components (Fig. 6, Table 3). By contrast, garnet in quartz garnetite and blue quartz-garnet-gahnite rocks from the B and C lodes is generally depleted in the spessartine and grossular components and enriched in the almandine component. Garnet in one sample of quartz garnetite from the 1 lens also shows enrichment in the almandine component. The composition of garnets obtained here reconfirms observations made previously by Spry and Wonder (1989), Spry et al. (2003), and Plimer (2006) that the composition of garnet in garnetite, quartz garnetite, and blue quartz-garnet-gahnite rocks reflects the overall bulk composition of the individual orebodies described by Johnson and Klingner (1975). Most garnets in these rocks and remobilized quartz garnetite are homogeneous in composition and show no discernible zoning. Exceptions to this are sharp compositional breaks in garnet from the garnet envelopes and rarely in garnetite. In both these rock types, orange colored spessartine-grossular overgrowths occur on earlier formed garnet (Fig. 3f). Similar overgrowths were reported previously by Spry and Wonder (1989) and Gregory et al. (2004).

Rare earth element compositions of garnet in garnet-rich rocks

One hundred and forty eight REE analyses of garnet in 32 samples were obtained using LA-ICP-MS techniques. The entire data set is available as an electronic supplement to this paper at http: _____." Representative compositions are given in Table 4. The bulk rock REE content was also determined for seventeen of these samples (Table 2).

Up to six ablations of garnet per sample were obtained. Although attempts were made to evaluate whether compositional zoning occurred within individual grains of garnet, this effort was thwarted by the presence of micromineral inclusions (silicates, mainly quartz, and sulfides) in many grains. Where possible, the cores of garnet grains were chosen for most analyses to minimize the chances of hitting late-stage or post peak metamorphic overgrowths. Moreover, the areas that were ablated were those that showed no visible mineral inclusions.

Chondrite-normalized REE abundances of garnet are presented in Figures 7 to 9. Care was taken to ensure that micromineral inclusions were not analyzed. This was of greater concern with the LA-ICP-MS instrument used at ISU, which had a beam spot twice the diameter of that at Macquarie University. La could not be plotted in samples where values were below the detection limit.

Garnetite and quartz garnetite: LA-ICP-MS analyses reveal that garnet in garnetite and laminated and massive varieties of quartz garnetite exhibit very low LREE/HREE values. In general, garnetite and massive or laminated varieties of quartz garnetite show flat HREE patterns (Figs. 7 and 8). Garnet in seven out of eleven samples of garnetite show weak to strongly positive Eu anomalies (Figs. 7a-g), whereas the remaining samples (Figs. 7h-k) have negative Eu anomalies. Sample 532-285, which consists essentially of friable garnet and hedenbergite, but is not by definition a garnetite (i.e., contains > 80% garnet), exhibits a pattern identical to that of garnetite. It has a positive Eu anomaly, a flat HREE distribution, and a very low LREE/HREE ratio (Fig. 7l).

Garnet in five of six samples of massive or laminated quartz garnetite exhibits negative Eu anomalies; sample 532-284, a massive quartz garnetite from the A lode, shows a weak positive Eu anomaly. No discernible Ce anomaly is present in any sample of garnetite or, massive and laminated quartz garnetite, which is consistent with the findings of Schwandt et al. (1993) for garnet in garnetite. Sample 532-298 was analyzed at ISU and Macquarie University. The patterns were essentially identical and emphasize the robustness of the data using both instruments (Figs. 8a and b).

To compare the patterns of garnet in garnetite and quartz garnetite with those of garnet in aluminous metasedimentary rocks spatially associated with sulfide mineralization, garnet in samples of garnet sillimanite schist adjacent to the B lode (532-222B) and biotite-muscovite schist adjacent to the 3 lens (532-84) were also analyzed. The garnet in the two aluminous metasedimentary rocks have negative Eu anomalies and the same overall REE patterns as those exhibited by garnet in garnetite and in laminated and massive varieties of quartz garnetite (Figs. 8h, i).

Garnet envelope and remobilized quartz garnetite: Samples 532-1, 532-21, and 532-502 are from the garnet envelope at the margin of the Pb-rich orebodies, whereas 532-316 is an example of a garnet envelope that occurs on the margins of a D_3 quartz vein. REE patterns of these rocks are characterized by LREE depletion similar to that exhibited by garnet in garnetite and in massive and laminated quartz garnetite (Figs. 9a-d). They also have positive Eu anomalies, except for sample 532-1 which shows a weak negative Eu anomaly. However, unlike most examples of garnet in garnetite and massive and laminated quartz garnetite, garnet from the garnet envelope shows a decrease in normalized REE abundances from Eu to Lu. Furthermore, individual analyses of different garnets within a given sample generally show a much greater variability in their REE content than do those of garnet in garnetite and in massive and laminated quartz garnetite, which show little compositional variation. Garnet in two samples of remobilized (possible D_3) quartz-garnetite (532-68 and 532-241) shows a pattern almost identical to that of garnet in samples from the garnet envelope (Figs. 9e-f).

Blue quartz-garnet-gahnite rocks: REE patterns of garnet in blue quartz-garnet-gahnite rocks (samples 532-2, 532-19A, S77-11, 6925-89.1, and Z3293-77.9) and a garnet-biotite rock with minor gahnite and quartz (sample 532-17) from B and C lodes show patterns more similar to those of garnet in remobilized quartz garnetite and from the garnet envelope than to those of garnet in garnetite and in massive and laminated quartz garnetite (Figs. 10a-f). Garnet in blue quartz-garnet-gahnite rocks exhibits low LREE values and negative Eu anomalies. The HREE patterns for sample 532-17 and two analyses of samples 532-19A and Z3293-77.9 are not flat but show negative slopes for REEs heavier than Tb, although the Lu/La ratio is higher than that of garnet in remobilized quartz garnetite and from the garnet envelope. Individual analyses of garnet from all gahnite-bearing samples from the B and C lodes show the same degree of variability of heavy REEs as those exhibited by garnet from remobilized quartz garnetite and garnet envelope.

Discussion

The REE pattern of garnet in metamorphic rocks is dependent on several variables including the partitioning of elements among coexisting minerals, bulk-rock composition, crystal chemistry, aqueous speciation of REEs in the metamorphic fluid phase in equilibrium with garnet, metamorphic P-T regime, and fO_2 conditions, and can be used to help determine the origin of garnet and its host rock (e.g., Sverjensky, 1984; Lottermoser, 1988, 1989, 1992; Bau 1991; Van Westernen et al., 2000; Smith et al., 2004). The garnet-bearing samples studied here consist primarily of garnet or garnet and quartz; however, variable amounts of sulfides and accessory phases (feldspar, apatite, monazite as in Fig. 3d, zircon, and titanite) are also present (Spry and Wonder, 1989). Because quartz and sulfides are generally deficient in REEs, REE patterns for garnet are unlikely to be affected by the partitioning of REEs between garnet and these minerals. Garnetite and quartz garnetite can contain several percent apatite and feldspar (Spry and

Wonder, 1989). However, samples chosen for LA-ICP-MS studies excluded those with more than trace amounts of feldspar, monazite, zircon, and titanite. It could be argued that even where a trace amount of these minerals is present they may significantly affect the REE content of the rock. However, it has been shown by Stanton (1976b, 2004) that chemical diffusion in quartz garnetite and garnetite at Broken Hill is limited to distances of the order of 0.1 mm. This suggests that widespread diffusion of REE between REE minerals and garnet has not occurred.

Studies by Shimizu (1975), Irving and Frey (1978), and McKay (1989) demonstrated that the size of the dodecahedrally coordinated site and the size of the REE cations make the HREE more compatible than the LREE in garnet enriched in the almandine and spessartine (SPALM) components. Smith et al. (2004) showed that metasomatic garnet enriched in Ca contains elevated LREEs because of the similarity in size between Ca^{2+} and the trivalent LREE. Previous studies of metasomatic garnet have focused on Ca-rich garnets, which exhibit high LREE/HREE ratios and a wide range in chondrite-normalized abundances among point analyses within an individual grain of garnet (Nicolescu et al., 1998; Smith et al., 2004).

REE patterns of garnet in remobilized quartz-garnetite and garnet envelope

Garnet in the garnet envelopes and in remobilized quartz garnetite at Broken Hill was likely precipitated from a metamorphic fluid during post-peak metamorphism (D_3) because they occur in white D_3 quartz veins or irregular patches that cross-cut S_0/S_1 banding in wall-rock schists, quartz garnetite and garnetite. Garnet in the garnet envelope and remobilized quartz garnetite is generally enriched in the almandine and spessartine components, but in two samples (532-241 and 532-507) garnet is enriched in the grossular component (with up to 21 wt. % CaO). Garnet in these rocks also has low to moderately

low LREE/HREE ratios, which are markedly different from the high LREE/HREE ratios observed in metasomatic Ca-rich garnet from skarns (Nicolescu et al., 1998) and contact aureoles (Smith et al., 2004).

The REE patterns of garnet in remobilized garnet and in the garnet envelope typically show variable chondrite-normalized REE contents and a decrease in normalized REE abundances from Eu to Lu (Fig. 9). The following factors must be considered when evaluating these patterns (1) the major element composition of the garnet, (2) the composition of the metamorphic fluid, (3) the effects of speciation of the hydrothermal fluid, and (4) the nature of pre-existing phases that may have broken down to form garnet during the D_3 retrograde (amphibolite facies) metamorphic event. For garnets analyzed here, concentrations of major elements are uniform within and between grains. Therefore, the overall variations in the HREEs do not reflect differences in major element compositions. Although Ca-rich overgrowths were found in several samples from the garnet envelope, such grains were avoided during this study.

The only information pertaining specifically to the composition of metasomatic fluids associated with the formation of the garnet envelope and remobilized quartz garnetite is that given by Spry (1978), who conducted a preliminary fluid inclusion study of quartz and garnet in these rocks. Inclusions contain H_2O-CH_4-CO_2-bearing fluids with up to eight daughter crystals. Total homogenization temperatures (T_h) for fluid inclusions in garnet ranged from approximately 304° to 324°C, whereas those in quartz were up to 378°C. Daughter crystals included halite, calcium chloride, sylvite, unidentified Na-Ca-Fe-Cl and Mn-Ca-Fe-Cl salts, two Ca-S minerals (one of which is anhydrite), and dawsonite [$NaAl(CO_3)(OH_2)$]. No attempt was made to determine densities of the fluid because of its chemical complexity (H_2O-CH_4-CO_2-NaCl-$MgCl_2$-KCl-$CaSO_4$-etc), but the pressure-corrected temperatures are likely to be hundreds of degrees higher than T_h due to the high salinities, which is consistent with the amphibolite facies metamorphic conditions associated with D_3. Prendergast et al. (1998) and Williams et al. (1998) in evaluating syn- to late-tectonic metasomatic fluids (D_1-D_3?) associated with quartz-garnet-hedenbergite

rocks in the A lode showed that, based on fluid inclusion studies, they had high temperatures (300-500°C) and were saline, with characteristic daughter mineral assemblages consisting of halite, sylvite, pyrosmalite [$(Fe,Mn)_8Si_{16}O_{15}(OH,Cl)_{10}$], and an unidentified Pb-K chloride. This rock type contains the same minerals as the remobilized hedenbergite-quartz garnetite from the 2 lens that was described by Spry (1978). Although Prendergast et al. (1998) and Williams et al. (1998) did not specifically associate these fluids with a given deformation event, the fluid inclusion assemblages and temperature of formation that they reported resemble those that are associated with the formation of remobilized quartz garnetite and garnetite envelope during D_3.

Based on the calculations of Sverjensky (1984), Wood (1990) and Bau (1991), the positive Eu anomaly in garnet from remobilized quartz garnetite and from the garnet envelope is likely due to the dominance of Eu^{2+} relative to Eu^{3+} in the metamorphic fluid, owing to the high temperatures (D_3 fluids were 500°-550°C). However, it should be noted that the study of Sverjensky (1984) focused on crustal fluids between the fayalite-quartz-magnetite and magnetite-hematite buffers. A positive Eu anomaly is also generally associated with reducing fluids, which is consistent with the presence of methane in fluid inclusions in quartz and garnet in these rocks. It is also possible that the positive Eu anomaly could also be associated with the alteration of plagioclase-bearing rocks in the footwall of the deposit, but there is no microscopic evidence for the pervasive alteration of plagioclase.

As was pointed out by Wood (2003), the lack of experimental data at elevated temperatures and pressures limits the understanding of ligands that may complex with REE under metamorphic conditions. Based on the experimental studies of Gammons et al. (1996, 2002) and Migdisov and Williams-Jones (2002), it has been shown that REE complex with chlorides, rather than fluorides or hydroxides in submarine geothermal conditions. However, there is less certainty as to the importance of chloride complexes in chloride-rich continental thermal waters (Wood, 2003). Regardless of whether the formation of Broken Hill ores was associated with venting in a submarine environment (e.g., Stanton,

1976a, b) or in a continental rift lake setting (e.g., Plimer, 2006), it is likely that chloride complexes dominated over fluoride complexes in hydrothermal fluids associated with the formation of precursors to laminated and massive quartz garnetite and garnetite. Fluorite is a common gangue mineral in the 2 lens orebody, and it is also present in some samples of massive and laminated quartz garnetite, but as pointed out by, for example, Samson and Wood (2005), REE-fluoride complexes are likely to be less important because of the low solubility of fluorite. Chloride complexing would account for the decrease in REE abundances from Eu to Lu in several samples of remobilized quartz garnetite and garnet envelopes since the stability of REE-chloride complexes increases with atomic number (Wood, 1990; Haas et al., 1995).

Remobilized quartz garnetite and garnet from the garnet envelope commonly replaced earlier formed massive and laminated varieties of quartz garnetite and garnetite. Thus, it is likely that the REE patterns of garnet in remobilized quartz garnetite and garnet envelopes were, in part, derived from the breakdown of garnet in massive and laminated varieties of quartz garnetite and garnetite since. This could explain the depleted LREE content in the metasomatic Ca-rich garnet, which would otherwise be expected to be elevated and to posses La_n/Lu_n ratios >1 (Nicolescu et al., 1998; Smith et al., 2004).

REE patterns of garnet in garnetite and massive and laminated quartz garnetite

Garnets in garnetite have very low LREE/HREE ratios and REE patterns that are essentially identical to those obtained by Schwandt et al. (1993). Such patterns are typical of garnet enriched in the almandine and spessartine (SPALM) components found in regionally metamorphosed rocks elsewhere (Hickmott et al., 1987; Seifert and Chadima, 1989; Hickmott and Shimizu, 1990; Schwandt et al., 1996). Most samples of garnetite and massive and laminated varieties of quartz garnetite studied here were from the 3 lens, and contain garnet enriched in the spessartine component rather than the grossular component. Garnet in these rocks contains between 0.53 and 12.98 wt. % CaO. The amount of Ca in garnet does not

appear to have any major effect on the shape of the REE pattern. This observation is contrary to that by Schwandt et al. (1993) who reported that the most Ca-rich garnet in garnetite (13.1 wt. % CaO) in their study had higher concentrations of LREE than garnet in the other three samples (between 0.9 and 4.1 wt. % CaO). Moreover, they suggested that there was an excellent correlation among concentrations of Eu, total LREE (La, Ce, and Nd) and Ca (R^2 = 0.97). Despite this, only a poor correlation (R^2 = 0.06) was observed here between Ca and the total LREE.

Garnet in samples of massive and laminated quartz garnetite has essentially the same REE pattern as the garnet in garnetite. Garnets in nine samples of garnetite, a friable hedenbergite-garnet rock (sample 532-284), and one sample of massive quartz garnetite (sample 532-284) have positive Eu anomalies and possess the same patterns as those reported by Schwandt et al. (1993) for garnet in proximal garnetite. Two samples of garnetite and four samples of laminated or massive quartz garnetite show negative Eu anomalies that mimic patterns reported by Schwandt et al. (1993) for distal garnetite.

The REE data for garnet in garnetite and in massive and laminated varieties of quartz garnetite suggest that these rock types had a common origin that was not related to sulfide melt metasomatism during peak metamorphism (Mavrogenes et al., 2004) or to metasomatism during peak or post-peak metamorphism as a result of fluid-facilitated interaction between the orebody and the aluminous wall rocks (e.g., Jones, 1968; Hodgson, 1975). On the contrary, the REE patterns of garnet in garnetite and quartz garnetite are distinct from those of metasomatic garnet in remobilized quartz garnetite and garnetite and have patterns characteristic of metamorphic garnet. The most likely explanations for the REE patterns of garnet in garnetite are those proposed by Schwandt et al. (1993), who suggested that they are characteristic of either a metamorphosed Mn-rich sediment of exhalative origin or of a metamorphosed hydrothermally altered sediment. Schwandt et al. (1993) suggested that the positive Eu anomalies for garnet in garnetite reflect low fO_2 conditions in the protolith of garnetite that formed proximal to a hydrothermal vent. Garnet in samples of garnetite studied here also mostly have a positive

Eu anomaly and support the view of Schwandt et al. (1993) that these rocks formed proximal to a hydrothermal vent. The remaining samples of garnetite and most samples of laminated and massive quartz garnetite have negative Eu anomalies.

The close spatial relationship between garnetite and quartz garnetite, and the fact that they are essentially only distinguished on the basis of quartz content suggests that they formed by the same process under similar physical and chemical conditions. We suggest that both rock types are metamorphosed products of submarine hydrothermal processes that operated proximal to a vent site. The negative Eu anomaly in some samples could be explained by the high oxygen fugacity conditions associated with the protolith or a high detrital component of the precursor material (Peter and Goodfellow, 1996; Spry et al., 2000). This means that these samples did not necessarily form more distal to a hydrothermal vent than those with a positive Eu anomaly, as is implied by the studies of Lottermoser (1989) and Schwandt et al. (1993).

Although REE compositions of individual garnets were not obtained from the Pinnacles deposit, Parr (1992) showed that bulk-rock REE patterns of garnet-rich rocks were controlled by stratigraphic position and reflected relative degrees of detrital input. Such a stratigraphic dependence would preclude a scenario in which Mn-rich garnet rocks were formed by a reaction between the Mn-rich orebodies and the country rock (e.g., Mavrogenes et al., 2004), as a symmetrical zonation of the garnet-rich rocks around the ores would be expected.

The patterns observed for garnet in garnetite and quartz garnetite are virtually the same as those reported by Rozendaal and Stalder (2001) and Stalder and Rozendaal (2005) for garnet in Fe- and Mn-rich exhalites spatially associated with the large BHT Gamsberg Zn deposit, South Africa. Garnet in garnet-rich rocks in the ore from the Gamsberg deposit has a distinct positive Eu anomaly whereas that above, below and lateral to the ore has a negative Eu anomaly. However, in contrast to garnet in garnetite

and quartz-garnetite at Broken Hill, Ca-rich garnet in garnet-rich rocks at Gamsberg has elevated LREE. The reason for this difference is uncertain, but it may be related to the presence of monazite, apatite, zircon, and titanite in garnetite and quartz garnetite from Broken Hill, which can incorporate high concentrations of the LREE. Rozendaal and Stalder (2001) also reported weak negative Ce anomalies in garnet and suggested that they were caused by prolonged exposure of the protolith to seawater. Although the low La content of garnet in several samples of quartz garnetite and garnetite at Broken Hill precludes the determination of a Ce anomaly, it is noted that where there is detectable La no observable Ce anomaly is present in the samples studied.

REE patterns of garnet in blue quartz-garnet-gahnite rock from B and C lodes

Parts of the B and C lodes at Broken Hill are commonly discordant to S_0 and S_1, and this raises the question as to the relative timing of formation of these orebodies. They are both characterized by blue quartz-garnet-gahnite rocks, which can cross-cut laminated quartz garnetite. Similar rocks have been found elsewhere in the Curnamona Province and are generally concordant to S_0 and S_1, but they can also be discordant to these planar features (e.g., Nine Mile deposit). The spatial distribution of blue quartz-garnet-gahnite rocks suggests that they had a protracted history of formation and that discordant varieties were remobilized from concordant rocks. Three samples of blue quartz-garnet-gahnite rock (532-2, 532-17, 532-19A) and one sample of a garnet-biotite rock (532-17) are from a feature known as the “Western Longitudinal” (Fig. 2), which is a fault-controlled, remobilized, and in places drag-folded portion of the B lode. The REE pattern of garnet in these samples is consistent with the interpretation that these rocks are products of remobilization, as the pattern resembles that for garnet in remobilized quartz garnetite and garnet envelope. In particular, they have variable HREE contents and, in the case of samples 17 and 19A, a decrease in normalized REE abundances from Tb to Lu.

Implications for exploration

The studies of Lottermoser (1989), Parr (1992), and Bodon (1996) suggest that the REE pattern of rocks in or adjacent to the Broken Hill, Pinnacles, and Cannington BHT deposits reflects the composition of an exhalative precursor prior to metamorphism and that the REE were mobilized over very short distances during prograde metamorphism. As pointed out by Lottermoser (1989), the presence of synchysite [(Ce, La)$Ca(CO_3)_2F$] along the fractures of feldspathic gneiss at Broken Hill indicates mobilization of REE during retrograde metamorphism. However, this was likely localized because, as Lottermoser (1989) further pointed out, the total REE abundance and pattern of garnet-rich rocks in retrograde shear zones at Broken Hill have the same patterns as those unaffected by shearing.

Lottermoser (1989) suggested that the positive and negative Eu anomalies associated with feldspar-, gahnite-, calcite, magnetite-, and garnet-rich lithologies (so-called meta-exhalites) was essentially dictated by Eh, pH, and temperature, such that a positive Eu anomaly was indicative of close proximity to a hydrothermal vent and sulfide mineralization, whereas a negative Eu anomaly was characteristic of a meta-exhalite that formed distal to ore. A strong positive anomaly as well as LREE-enriched and HREE-depleted patterns were reported by Bodon (1996) for various styles of mineralization at the Cannington Ag-Pb-Zn deposit, Queensland. Lottermoser (1989) suggested that sulfide ores and proximal exhalites are enriched in LREEs and Eu similar to recent hydrothermal fluids and metalliferous sediments at mid-ocean ridges. Parr (1992) showed that garnet-rich rocks in the footwall of the Pinnacles deposit have negative Eu anomalies, whereas garnet-rich rocks in the hanging wall or in the orebody have no or positive Eu anomalies. This apparent stratigraphic control was assessed in terms of the same physical parameters discussed by Lottermoser (1989), with the added caveat that the HREEs in footwall

samples may reflect hydrothermal leaching of these elements during pre-metamorphic hydrothermal alteration.

At Broken Hill, whole-rock REE analyses of garnetite as well as individual REE analyses of garnet in garnetite show positive Eu anomalies. These data are consistent with the findings of Schwandt et al. (1993) who also showed positive Eu anomalies for garnet in garnetite. Although this relationship can be used to indicate close proximity to a hydrothermal vent and associated sulfides, it is not the case for other garnet-bearing rocks. Blue quartz-garnet-gahnite rocks and garnet contained therein from the B and C lodes in the stratigraphic footwall of the deposit have negative Eu anomalies. Whole-rock REE analyses of laminated and massive quartz garnetite as well as individual REE analyses of garnet in laminated and massive quartz garnetite have both positive and negative Eu anomalies. These REE data show that only the positive and negative Eu anomaly of garnetite and blue quartz-garnet-gahnite rock (and garnet contained therein), respectively, can be used as an exploration guide to ore but that the sign of this anomaly for laminated and massive quartz garnetite cannot be used in this manner.

Whole-rock REE patterns of garnetite and quartz garnetite and individual REE analyses of garnets in these rocks that formed distal to the Broken Hill deposit and in minor BHT elsewhere in the southern Curnamona Province, including the Olary Domain, are similar to those of garnetite and quartz garnetite at Broken Hill (Heimann et al., 2005, Heimann, 2006). Negative Eu anomalies are generally observed in garnet-rich rocks in minor BHT deposits and also in individual garnets from these same rocks. It should be noted that garnet in garnet-rich rocks closest to ore at the Gamsberg deposit has positive Eu anomalies and the largest Eu/Eu* values, whereas those distal to or stratigraphically above or below the deposit have negative Eu anomalies (Rozendaal and Stalder, 2001). Such patterns are similar to those described by Parr (1992) for garnet-rich rocks from the Pinnacles deposit.

Conclusions

The precursors to garnetite and massive and laminated varieties of quartz garnetite formed by submarine exhalative processes beneath the sea floor, whereas remobilized quartz garnetite and garnet envelopes surrounding quartz veins and the orebodies formed by metasomatic processes post-peak metamorphism (likely D_3). The chondrite-normalized REE patterns of metasomatic garnet at Broken Hill show positive and negative Eu anomalies, variable HREEs, low to moderate LREE/HREE ratios, and characteristic arcuate patterns. The REE signature of garnet in garnetite and quartz garnetite resembles that of metamorphic garnet with Eu anomalies reflecting fO_2 conditions, temperature, and relative inputs of detrital to hydrothermal components in a premetamorphic protolith. An arcuate HREE pattern is also evident for garnet in blue quartz-garnet-gahnite rocks that also likely formed post-peak metamorphism. Whether this means that all B and C lode mineralization formed post-peak metamorphism and did not form by submarine hydrothermal processes remains unclear.

Whole-rock REE patterns of garnetite and of garnet in garnetite generally show positive Eu anomalies, whereas whole-rock REE patterns of blue quartz-garnet-gahnite rock and of garnet in blue quartz-garnet-gahnite rock show negative Eu anomalies. These patterns suggest that the Eu anomaly of these rocks can be used as an indicator of close proximity to ore at Broken Hill. However, the whole-rock REE patterns of massive and laminated quartz garnetite and of garnet in these rocks have variably positive or negative Eu anomalies suggesting that Eu anomalies for these rocks are not reliable indicators to ore.

Acknowledgements

This study was supported through National Science Foundation Grant EAR 03-09627, a Society of Economic Geology Hugh E. McKinstry Student Research Grant, and an Iowa State University College

of Liberal Arts and Science Research Grant. The assistance of Ellery Frahm with electron microprobe analyses is greatly appreciated as is the help of Suzy Elhou and Simon Jackson with the collection and discussion of LA-ICP-MS data. Many fruitful discussions with Mark Fanning, Iain Groves, Wolfgang Leyh, John Mavrogenes, Ian Plimer, and Barney Stevens, and Graham Teale on various aspects of Broken Hill geology are much appreciated. We thank Perilya and Consolidated Broken Hill (especially Ian Plimer) for access to core. Steve Scott kindly provided samples for this study and communications with Martin Smith considerably helped our understanding of the REE systematics of garnets. CETAC provided the GeoPro software. The magnetic sector ICP-MS device was provided by the U.S. Department of Energy, Office of Nuclear Nonproliferation and Basic Energy Sciences. Ames Laboratory is operated by the U.S. Department of Energy by Iowa State University under Contract No. W-7405-Eng-82. We thank Mark Hannington, Scott Wood and an anonymous *Economic Geology* reviewer for constructive reviews of the manuscript and Todd Bonsall for assistance with drafting.

REFERENCES

Barnes, R.G., Stevens, B.P.J., Stroud, W.J., Brown, R.E., Willis, I.L., and Bradley, G.M., 1983, Zinc-, manganese-, and iron-rich rocks and various minor rock types, *in* Stevens, B.P.J., and W.J. Stroud, eds., Rocks of the Broken Hill Block: their classification, nature, stratigraphic distribution, and origin: Records of the Geological Survey of New South Wales, v. 21 (1), p. 289-323.

Bau, M., 1991, Rare-earth element mobility during hydrothermal and metamorphic fluid-rock interaction and the significance of the oxidation state of europium: Chemical Geology, v. 93, p. 219-230.

Bodon, S., 1996, Genetic implications of the paragenesis and rare-earth element geochemistry at the Cannington-Ag-Pb-Zn deposit, Mt. Isa Inlier, northwest Queensland, *in* Pongratz, J., and Davidson, G.J., eds., New developments in Broken Hill-type deposits: Centre for Ore Deposit and Exploration Studies Special Publication v. 1, p. 132-144.

Burton, G.R., 1994, Metallogenic studies of the Broken Hill and Euriowie Blocks, New South Wales. 3. Minerals deposits of the south-eastern Broken Hill Block: Bulletin of the Geological Survey of New South Wales, v. 32 (3), 100 p.

Courtois, G., and Treuil, M., 1977, Distribution des terres rares et de quelques éléments en trace dans les sédiment récents des fosses de la Mer Rouge: Chemical Geology, v. 20, p. 57-72.

Crawford, A.J., 2006, A magmatic-hydrothermal origin for the Broken Hill orebodies? Geoscience Australia Record, v. 2006/21, p. 34-35.

Ehlers, K., Foster, J., Nutman, A.P., and Giles, D., 1996, New constraints on Broken Hill geology and mineralization, *in* Pongratz, J., and Davidson, G.J., eds., New developments in Broken Hill-type deposits: Centre for Ore Deposit and Exploration Studies Special Publication v. 1, p. 73-87.

Frost, B.R., Mavrogenes, J.A., and Tomkins, A.G., 2002, Partial melting of sulfide ore deposits during medium- and high-grade metamorphism: Canadian Mineralogist, v. 40, p. 1-18.

Frost, B.R., Swapp, S.M., and Gregory, R.W., 2005, Prolonged existence of sulfide melt in the Broken Hill orebody, New South Wales, Australia: Canadian Mineralogist, v. 43, p. 479-493.

Gammons, C.H., Wood, S.A., and Williams-Jones, A.E., 1996, The aqueous geochemistry of the rare earth elements and yttrium: VI. Stability of neodymium chloride complexes at 25°C to 300°C. Geochemica et Cosmochimica Acta, v. 60, p. 4615-4630.

Gammons, C.H., Wood, S.A., and Li, Y., 2002, Complexation of the rare earth elements with aqueous chloride at 200°C and 300°C and saturated water vapor pressure *in* Hellman, R., and Wood, S.A., eds., Water-rock interaction, ore deposits, and environmental geochemistry: A tribute to David A. Crerar: Geochemical Society Special Publication, v. 7, p. 191-207.

Gibson, G., 2000, Tectonic evolution of the Paleoproterozoic Willyama Supergroup, Broken Hill: The early years [abs.]: Australian Geological Survey Organisation Record 2000/10, p. 45-47.

Gibson, G.M., and Nutman, A.P., 2004, Detachment faulting and bimodal magmatism in the Palaeoproterozoic Willyama Supergroup, south central Australia: keys to recognition of a multiply deformed Precambrian metamorphic core complex: Journal of the Geological Society, London, v. 161, p. 55-66.

Giles, D., Betts, P., and Lister, G., 2002, Far-field continental backarc setting for the 1.80-1.67 Ga basins of northeastern Australia: Geology, v. 30, p. 823-826.

Gregory, R.W., Swapp, S.M., and Frost, B.R., 2004, Late-stage metasomatic garnet growth adjacent to the Broken Hill Pb-Zn-Ag sulfide ore body [abs.]: Geological Society of America Abstracts with Programs, v. 36, no. 5, p. 355.

Haas, J.R., Shock, E.L., and Sassani, D.C., 1995, Rare earth elements in hydrothermal systems: estimates of standard partial molar thermodynamic properties of aqueous complexes of the aqueous rare earth elements at high pressures and temperatures: Geochimica et Cosmochimica Acta, v. 59, p. 4329-4350.

Haydon, R.C., and McConachy, G.W., 1987, The stratigraphic setting of Pb-Zn-Ag mineralization at Broken Hill: ECONOMIC GEOLOGY, v. 82, p. 826-856.

Heimann, A., 2006, Geochemical keys for the genesis of Proterozoic garnet-rich rocks and minor metasediment-hosted Pb-Zn-Ag mineralization, southern Curnamona province, Australia. Unpublished Ph.D. dissertation, Ames, Iowa State University, 296 p.

Heimann, A., Spry, P.G., Teale, G.S., Conor, C.H.H., and Pearson, N.J., 2005, Major and rare-earth element chemistry of garnet-rich rocks in the Curnamona Province, Australia: Implications for Broken Hill-type mineralization [abs.]: Geological Society of America Abstracts with Programs, v. 37, no. 7, p. 452.

Henderson, Q.J., 1953, North Broken Hill mine, *in* Edwards, A.B., ed., Geology of Australian ore deposits: Australasian Institute of Mining and Metallurgy, v. 1, 627-649.

Hickmott, D.D., and Shimizu, N., 1990, Trace element zoning in garnet from the Kwoiek area, British Columbia: disequilibrium partitioning during garnet growth?: Contributions to Mineralogy and Petrology, v. 104, p. 619-630.

Hickmott, D.D., Shimizu, N., Spear, F.S. and Selverstone, J., 1987, Trace-element zoning in a metamorphic garnet: Geology, v. 15, p. 573-576.

Hodgson, C.J., 1975, The geology and geological development of the Broken Hill lode in the New South Wales Consolidated mine, Australia. III. Petrology and petrogenesis: Journal of the Geological Society of Australia, v. 22, p. 159-213.

Irving, A.J., and Frey, F.A., 1978, Distribution of trace elements between garnet megacrysts and host volcanic liquids of kimberlitic to rhyolitic composition: Geochimica et Cosmochimica Acta, v. 42, p. 771-787.

Jackson, S.E., Longerich, H.P., Dunning, G.R., and Fryer, B.J., 1992, The application of laser-ablation microprobe-inductively coupled plasma-mass spectrometry (LAM-ICP-MS) to in situ trace-element determinations in minerals: Canadian Mineralogist, v. 30, p. 1049-1064.

Johnson, I.R., and Klingner, G.D., 1975, The Broken Hill ore deposit and its environment, *in* Knight, C.L., ed., Economic geology of Australia and Papua New Guinea: Australasian Institute of Mining and Metallurgy Monograph, v. 5, p. 476-495.

Jones, T.R., 1968, Garnet sandstone and garnet rims at orebody contacts at Broken Hill, *in* M. Radmanovich, M., and Woodcock, J.T., eds., Broken Hill mines -1968: Australasian Institute of Mining and Metallurgy Monograph Series 3, p. 171-178.

Laing, W.P., Marjoribanks, R.W., and Rutland, R.W.R., 1978, Structure of the Broken Hill mine area and its significance for the genesis of the orebodies: Economic Geology, v. 73, p. 1112-1136.

Large, R.R., 2003, BHT deposits: Part of the spectrum of stratiform sediment hosted Zn-Pb-Ag deposits: Australian Geological Survey Organisation Record 2000/10, p. 93-96.

Lottermoser, B.G., 1988, Rare earth element composition of garnets from the Broken Hill Pb-Zn-Ag orebodies, Australia: Neues Jahrbuch fur Mineralogie Montatshefte, v. 9, p. 423-431.

_____ 1989, Rare earth elements study of exhalites within the Willyama Supergroup, Broken Hill Block, Australia: Mineralium Deposita, v. 24, p. 92-99.

_____ 1992, Rare earth elements and hydrothermal ore formation processes: Ore Geology Reviews, v. 7, p. 25-41.

Mavrogenes, J., Kalinowski, A., Sparks, H.A., and Frost, R., 2004, Sulfide melt metasomatism: Metamorphic alteration at Broken Hill, Australia [abs.]: Eos Transactions of the American Geophysical Union, Joint Assembly Supplement, v. 85, no. 17, p. JA 493.

McDonough, W.F., and Sun, S.-S., 1995, The composition of the Earth: Chemical Geology, v. 120, p. 223-253

McKay, G.A., 1989, Partitioning of rare earth elements between major silicate minerals and basaltic melts: Reviews in Mineralogy, v. 21, p. 45-77.

Migdisov, A.A., and Williams-Jones, A.E., 2002, A spectrophotometric study of neodymium(III) complexation in chloride solutions: Geochemica et Cosmochimica Acta, v. 66, p. 4311-4323.

Nicolescu, S., Cornell, D.H., Södervall, U., and Odelius, H., 1998, Secondary ion mass spectrometry analysis of rare earth elements in grandite garnet and other skarn related silicates: European Journal of Mineralogy, v. 10, p. 251-259.

Norman, M.D., Pearson, N.J., Sharma, A., and Griffin, W.L., 1996, Quantitative analysis of trace elements in geological materials by laser ablation ICPMS: Instrumental operating conditions and calibration values of NIST glasses: Geostandards Newsletter, v. 20, 247-261.

Nutman, A.P., and Ehlers, K., 1998, Evidence for multiple Paleoproterozoic thermal events and magmatism adjacent to the Broken Hill Pb-Zn-Ag orebody, Australia: Precambrian Research, v. 90, p. 203-238.

O'Driscoll, E.S., 1953, The Zinc Corporation and New Broken Hill Consolidated mines, *in* Edwards, A.B., ed., Geology of Australian ore deposits. Australasian Institute of Mining and Metallurgy, v. 1, p. 658-673.

Page, R.W., Stevens, B.P.J., and Gibson, G.M., 2005a, Geochronology of the sequence hosting the Broken Hill Pb-Zn-Ag orebody: ECONOMIC GEOLOGY, v. 100, p. 633-661.

Page, R.W., Conor, C.H.H., Stevens, B.P.J., Gibson, G.M., Priess, W.V., and Southgate, P.N., 2005b, Correlation of Olary and Broken Hill Domains, Curnamona province," possible relationship to Mount Isa and other north Australia Pb-Zn-Ag bearing successions: ECONOMIC GEOLOGY, v. 100, p. 663-676.

Parr, J.M., 1992, Rare-earth element distribution in exhalites associated with Broken Hill-type mineralisation at the Pinnacles deposit, New South Wales, Australia: Chemical Geology, v. 100, p. 73-91.

_____, 1994, The geology of the Broken Hill-type Pinnacles Pb-Zn-Ag deposit, western New South Wales, Australia: ECONOMIC GEOLOGY, v. 89, p. 778-790.

Parr, J.M., and Plimer, I.R., 1993, Models for Broken Hill-type lead-zinc-silver deposits, *in* Kirkham, R.V., Sinclair, W.D., Thorpe, R.I., and Duke, J.M., eds., Mineral deposit modeling: Geological Association of Canada Special Paper 40, p. 253-288.

Pearce, N.J.G., Perkins, W.T., Westgate, J.A., Gorton, M.P., Jackson, S.E., Neal, C.R., and Cheney, S.P., 1997, New data for National Institute of Standards and Technology 610 and 612 glass reference materials: Geostandards Newsletter, v. 21, p. 115-144.

Peter, J.M., and Goodfellow, W.D., 1996, Mineralogy, bulk and rare earth element geochemistry of massive sulphide associated hydrothermal sediments of the Brunswick horizon, Bathurst mining camp, New Brunswick: Canadian Journal of Earth Sciences, v. 33, p. 252-283.

Phillips, G.N., 1980, Water activity changes across an amphibolite-granulite facies transition, Broken Hill, Australia: Contributions to Mineralogy and Petrology, v. 75, p. 377-386.

Phillips, G.N., and Wall, V.J., 1981, Evaluation of prograde regional metamorphic conditions; their implication for the heat source and water activity during metamorphism in the Willyama Complex, Broken Hill, Australia: Bulletin Minéralogie, v. 104, p. 801-810.

Plimer, I.R., 1984, The mineralogical history of the Broken Hill lode, N.S.W: Australian Journal of Earth Sciences, v. 31, p. 379-402.

_____, 1985, Broken Pb-Zn-Ag deposit – A product of mantle metasomatism: Mineralium Deposita, v. 20, p. 147-153.

_____ , 2006, Manganoan garnet rocks associated with the Broken Hill Pb-Zn-Ag orebody, Australia: Mineralogy and Petrology, v. 88, p. 443-478.

Prendergast, K., Stansfield, S., and Williams, P.J. 1998, Syn-late tectonic metasomatism in Western A-lode, Broken Hill [abs]: Geological Society of Australia Abstracts, no. 49, p. 364.

Prince, C.I., Kosler, J., Vance, D., and Günther, D., 2000, Comparison of laser ablation ICP-MS and isotope dilution REE analyses – implications for Sm-Nd garnet geochronology: Chemical Geology, v. 168, p. 255-274.

Richards, S.M., 1966, The banded iron formations at Broken Hill, Australia, and their relationship to the zinc-lead orebodies: ECONOMIC GEOLOGY, v. 61, p. 257-274.

Rothery, E., 2001, Tectonic origin of the shape of the Broken Hill lodes supported by their structural setting in a high-grade shear zone: Australian Journal of Earth Sciences, v. 48, p. 201-220.

Rozendaal, A., and Stalder, M., 2001, REE geochemistry of garnet associated with the Gamsberg Zn-Pb deposit. South Africa., *in* Piestrzyñski, A. et al., eds., Mineral deposits at the beginning of the 21st century: Lisse, A.A. Balkema, p. 325-328.

Samson, I.M., and Wood, S.A., 2005, The rare earth elements: Behaviour in hydrothermal fluids and concentrations in hydrothermal mineral deposits, exclusive of alkaline settings *in* Linnen, R.L., and Samson, I.M., eds., Rare-element geochemistry and mineral deposits: Geological Association of Canada Short Course Notes, v. 17, p. 269-297.

Schwandt, C.S., Papike, J.J., and Shearer, C.K., 1996, Trace element zoning in pelitic garnet of the Black Hills, South Dakota: American Mineralogist, v. 81, p. 1195-1207.

Schwandt, C.S., Papike, J.J., Shearer, C.K., and Brearley, A.J., 1993, Crystal chemical control of REE incorporation in garnets from the Broken Hill Pb-Zn-Ag orebodies, Australia: Canadian Mineralogist, v. 31, p. 371-379.

Segnit, E.R., 1961, Petrology of the zinc lode, New Broken Hill Consolidated Ltd., Broken Hill, New South Wales: Proceedings of the Australasian Institute of Mining and Metallurgy, v.199, p. 87-112.

Seifert, K.E., and Chadima, S.A., 1989, Depletion of heavy rare-earth elements in metamorphic minerals from Adirondack anorthosites: Geology, v. 17, p. 1004-1006.

Shimizu, N., 1975, Rare earth elements in garnets and clinopyroxenes from garnet lherzolite nodules in kimberlites: Earth and Planetary Science Letters, v. 25, p. 26-32.

Smith, M.P., Henderson, P., Jeffries, T.E.R., Long, J., and Williams, C.T., 2004, The rare earth elements and uranium in garnets from the Beinn an Dudhaich aureole, Skye, Scotland, UK: Constraints on processes in a dynamic hydrothermal systems: Journal of Petrology, v. 45, p. 457-484.

Spry, P.G., 1978, The geochemistry of garnet-rich lithologies associated with the Broken Hill orebody, N.S.W., Australia: Unpublished M.S. thesis, Adelaide, University of Adelaide, 129 p.

Spry, P.G., and Wonder, J.D., 1989, Manganese-rich garnet rocks associated with the Broken Hill lead-zinc-silver deposit, New South Wales, Australia: Canadian Mineralogist, v. 27, p. 275-292.

Spry, P.G., Peters, J., and Slack, J.F., 2000, Meta-exhalites as keys in the search for metamorphosed ore deposits: Reviews in Economic Geology, v. 11, p. 163-201.

Spry, P.G., Teale, G.T., and Heimann, A., 2003, Speculations concerning the origin and exploration significance of lode rocks in the Curnamona Province: Geoscience Australia Record 2003/13, p. 162-165.

Stalder, M., and Rozendaal, A., 2005, Trace and rare earth element garnet and apatite as discriminant for Broken Hill-type mineralization, Namaqua Province, South Africa, *in* Mao, J. and Bierlein, F.P., eds., Mineral Deposit Research: Meeting the Global Challenge: Berlin, Springer, p. 699-702.

Stanton, R.L., 1976a, Petrochemical studies of the ore environment at Broken Hill, NSW: 4. Environmental synthesis: Transactions of the Institute of Mining and Metallurgy, v. 85, B477-B480.

_____1976b, Speculations on the chemical metasediments of Broken Hill, New South Wales, Australia: Transactions of the Institution of Mining and Metallurgy, v. 85, B221-B233.

_____2004, Exhalative metasediments – clues to the real nature of regional metamorphic processes: Mineralogy and Petrology, v. 80, p. 111-122.

Stevens, B.P.J., 1986, Post depositional history of the Willyama Supergroup in the Broken Hill Block, N.S.W.: Australian Journal of Earth Science, v. 33, p. 73-98.

_____1996, Broken Hill area, Australia, as a Proterozoic fold and thrust belt: implications for the Broken Hill base-metal deposit – discussion. Transactions of the Institution of Mining and Metallurgy, v. 105, B89-B90.

Stillwell, F.L., 1959, Geology of the Broken Hill lode and its bearing on ore genesis: Proceedings of the Australasian Institute of Mining and Metallurgy, v. 190, p. 1-84.

Sverjensky, D.A., 1984, Europium redox equilibria in aqueous solution: Earth and Planetary Science Letters, v. 67, p. 70-78.

Van Achterberg, E., Ryan, C.G., Jackson, S.E., and Griffin, W.L., 2001, Data reduction software for LA-ICP-MS: appendix, *in* Sylvester, P.J., ed., Laser ablation-ICP-mass spectrometry in the earth sciences: Principles and applications: Mineralogical Association of Canada Short Course Series, v 29, p. 239-243.

Van Westernen, W., Allan, N.L., Blundy, J.D., Purton, J.A., and Wood, B.J., 2000, Atomistic simulation of trace element incorporation into garnets – comparison with experimental garnet-melt partition data: Geochimica et Cosmochimica Act, v. 64, p. 1629-1639.

Webster, A.E., 2006, The geology of the Broken Hill deposit, New South Wales, Australia: Australian Research Council Centre of Excellence in Ore Deposits, University of Tasmania, CODES Monograph 1, 278 p.

White, S.H., Rothery, E., Lipps, A.L.W., and Barclay, T.J.R., 1995, Broken Hill area, Australia, as a Proterozoic fold and thrust belt: implications for the Broken Hill base-metal deposit: Transactions of the Institution of Mining and Metallurgy, v. 104, p. B1-B15.

_____ 1996, Broken Hill area, Australia, as a Proterozoic fold and thrust belt: implications for the Broken Hill base-metal deposit – reply: Transactions of the Institution of Mining and Metallurgy, v. 105, B90-B98.

Wiggins, J., 1988, Studies of exhalite mineral chemistry and structure within Blackwoods open-cut: Unpublished B.Sc. Honours thesis, Newcastle, New South Wales, University of Newcastle, 276 p.

Williams, P.J., Dong, G., Pollard, P.J., Ryan, C.G., Chapman, L.H., Prendergast, K., 1998., Two-stage, dual source origin of Broken Hill-type Pb-Zn-Ag deposits [abs.]: Geological Society of Australia Abstracts, no. 49, p. 470.

Willis, I.L., Brown, R.E., Stroud, W.J., and Stevens, B.P.J., 1983, The Early Proterozoic Willyama Supergroup: stratigraphic subdivisions and interpretations of high- to low-grade metamorphic rocks in the Broken Hill Block, New South Wales: Journal of the Geological Society of Australia, v. 30, p. 195-224.

Wood, S.A., 1990, The aqueous geochemistry of rare earth elements and yttrium. Part II. Theoretical predictions of speciation in hydrothermal solutions to 350°C at saturated water vapor pressure: Chemical Geology, v. 88, p. 99-125.

_____, 2003, The geochemistry of rare earth elements and yttrium in geothermal waters *in* Simmons, S.F., and Graham, I., eds., Volcanic, geothermal, and ore-forming fluids: Rulers and witnesses of processes with the Earth: Society of Economic Geologists Special Publication No. 10, p. 133-158.

Wright, J.V., Haydon, R.C., and McConachy, G.W., 1987, Sedimentary model for the giant Broken Hill Pb-Zn deposit, Australia: Geology, v. 15, p. 598-602.

_____1993, Sedimentary analysis and implications for Pb-Zn mineralisation at Broken Hill, Australia: James Cook University Economic Geology Research Unit Contribution 48, 93 p.

TABLE 1. Lithology, Location and Mineralogy of Garnet-Bearing Rocks Analyzed for REE Studies

Sample	Lithology	Location	Mineralogy[1]	Accessory and trace minerals[1]
Blackw1[2]	Garnetite	Blackwoods pit, hanging wall of 3 lens[5]	Gr., qtz	Mgt, ilm, hem
Blackw4[4]	Garnetite	Blackwoods pit, hanging wall of 3 lens[6]	Gr.	Qtz, gn, po, ccp, sp, td, hem
Blackw5[4]	Garnetite	Blackwoods pit, hanging wall of 3 lens[7]	Gr.	Qtz, kfs, hm
Blackw8[4]	Garnetite	Blackwoods pit, hanging wall of 3 lens[8]	Gr.	Qtz, gn, po, ccp, sp
Kintore 3[2]	Garnetite	Kintore pit, adjacent to 3 lens[9]	Gr.	Qtz
Kintore 4[2]	Garnetite	Kintore pit, adjacent to 3 lens[10]	Gr.	Qtz
532-29[2]	Garnetite	27 level, 3 lens, 15N stope (NM)[11]	Gr.	Qtz, gn, ap, sp, ccp, td
532-83[4]	Laminated garnetite	27 level, 3 lens, 13N stope (NM)[12]	Gr.	Qtz, gn, ilm, po, ccp
532-45[3]	Garnetite	27 level, 3 lens, 16 stope (NM)[13]	Gr., sp, qtz	Apy, po, ccp, gn
532-104[3]	Garnetite	27 level, 3 lens, 16 stope (NM)[14]	Gr., sp	Qtz, ccp, gn, py, po
532-117[2]	Garnetite	19 level, 3 lens, 13 stope (NBHC)[15]	Gr.	Qtz, chl, bt, ilm, gn, hem
532-119[3]	Garnetite	19 level, 3 lens, 13 stope (NBHC)[16]	Gr.	Qtz
532-139[2]	Laminated garnetite	28 level, 3 lens, 14 stope (NM)[17]	Gr.	Qtz, po, bt, ilm, ccp, sp, gn, apy
S76-254[3]	Garnetite in ore	27 level, 3 lens, 13 stope (NM)[18]	Gr., gn	Qtz, sp, ccp, apy, po, td
532-283[3]	Garnetite in ore	17 sub-level, A lode, 6 stope (NBHC)[19]	Gr.	Qtz, sp, po, gn, ccp
532-313[3]	Garnetite	12 level, A lode (ZC)[20]	Gr., qtz	Sp, gn, po, ccp
6844-47.8[2]	Garnetite	Section 63, 2 lens (NBHC)[21]	Gr.	Qtz, bt, ilm, ap
532-285[4]	Hedenbergite-garnet-rock	17 sub-level, A lode, 6 stope (NBHC)[22]	Hd, grt	Qtz, sp, gn, ccp, po, apy, ilm
532-335[2]	Laminated quartz-cummingtonite-garnet rock	17 level, 2 lens (ZC)[23]	Qtz, grt, cum, sp, gn	Wo, cal, ccp, po
532-228B[3]	Massive quartz garnetite	18 level, B lode, H stope (NBHC)[24]	Qtz, grt, bt	St, po, ccp, zrn, ilm, py
532-231[2]	Massive quartz garnetite	28 level, 2 lens (NM)[25]	Qtz, grt	Gn, cal, ep, bt, chl, ap, py, ilm
532-284[3]	Massive quartz garnetite	16 level, A lode (NBHC)[26]	Gr., qtz	Gn
532-298[4]	Massive quartz garnetite	Drill hole 2275 61.2 feet, C lode[27]	Qtz, grt	Gn, po, ilm, gah, ccp, apy
532-303[3]	Massive quartz garnetite	12 level, 1 lens, (ZC)[28]	Qtz, grt	Bt, sp, gn, cp, po, py, hm
532-304[2]	Massive quartz garnetite	12 level, 1 lens, (ZC)[29]	Qtz, grt	Ilm, bt, sp, gn, po, ccp
532-311[4]	Massive quartz garnetite	12 level, B lode (ZC)[30]	Qtz, grt	Ilm, gn
532-343[4]	Laminated quartz garnetite	20 level, 1 lens, 24 E stope (NBHC)[31]	Gr., qtz	Ccp, ilm, po, sp, gn
532-599[4]	Laminated quartz garnetite	36 level, 2 or 3 lens (NM)[32]	Qtz, grt	Ilm, gn, cp
S76-283[2]	Massive quartz garnetite	13 level, B lode (NBHC)[33]	Qtz, grt,	Bt, po, ms
532-2[3]	Quartz-gahnite-garnet rock	13 level, B lode, W Long (NBHC)[34]	Qtz, gah, grt	Bt, sp, apy, ccp, gn, po
532-17[3]	Garnet-biotite rock	13 level, B lode, W Long (NBHC)[35]	Gr., bt	Gah, qtz, sp, gn, po, ccp, apy
532-19A[4]	Gahnite-garnet-quartz rock	13 level, B lode, W Long (NBHC)[36]	Gah, grt, qtz	Bt, po, sp, ccp, ilm
S77-11[4]	Quartz-garnet-gahnite rock	13 level, B lode, W Long (NBHC)[37]	Qtz, grt, gah	Bt, mgt, po, ccp, apy, chl, ilm
6925-89.1[4]	Quartz-garnet-gahnite rock	Section 41, C lode (NBHC)[38]	Qtz, grt, gah	Bt, ilm, sp, po, gn, ccp, hm
6930-48.4[2]	Garnet-biotite-gahnite rock	Section 41, C lode (NBHC)[39]	Gr., bt, gah	Qtz, sp, po, gn, ccp
Z3293-63.0[2]	Quartz-gahnite-garnet rock	Section 36, C lode (NBHC)[40]	Qtz, grt, gah	Bt, kfs, ms, st, ilm, py, ccp, sp
Z3293-77.9[2]	Quartz-gahnite-garnet rock	Section 36, C lode (NBHC)[41]	Gr., qtz, gah	Bt, ms, ilm, gn, po, ccp
Z3512-67.7[2]	Quartz-gahnite-garnet rock	Section 30, C lode (ZC)[42]	Qtz, grt, gah	Sp, gn, ilm, ccp, po
Z3512-120.2[2]	Quartz-gahnite-garnet rock	Section 30, C lode (ZC)[43]	Qtz, grt, gah	Gn, ccp, po, sp, ilm
532-68[4]	Remobilized quartz garnetite	28 level, 3 lens 15 stope (NM)[44]	Gr., qtz, bt, gn, sp	Ilm, bt, sp, po
532-107[2]	Remobilized quartz garnetite	27 level, 3 lens, 12 stope (NM)[45]	Gr., qtz	Bt, chl, cal, ap, apy, ilm, po
532-241[4]	Remobilized quartz garnetite	28 level, 2 lens (NM)[46]	Gr., qtz	Sp, gn, ccp
532-334[2]	Remobilized quartz garnetite	17 level, 2 lens (ZC)[47]	Gr., qtz, bt	Gn, cp, sp, po
532-500[3]	Remobilized quartz garnetite	28 level, 3 lens, 15 stope (NM)[48]	Gr., qtz	
532-1[4]	Garnet envelope	21 level, lead lode 21 W stope (NBHC)[49]	Gr., qtz, bt, ms	Ilm
532-21[4]	Garnet envelope	27 level, 3 lens 16 stope (NM)[50]	Gr., qtz	Ilm, ap
532-316[3]	Garnet envelope	36 level, 1 lens (NM)[51]	Gr., qz	Mgt, hem
532-502[2]	Garnet envelope	28 level, 3 lens (NM)[52]	Gr., qtz, sp	Td, ccp, gold
S76-221[4]	Garnet envelope	19 level, 2 lens (ZC)[53]	Qtz, grt, bt	Ccp, ilm, po, apy, sp, gn
532-222B[4]	Garnet-sillimanite schist	15 level, B Lode (NBHC)[54]	Gr., sil, bt, qz, st	Ap, ms, po, cp, ilm
532-84[3]	Biotite-muscovite schist	27 level, 3 lens, 13N stope (NM)[55]	Bt, ms, grt, qtz	

[1] Listed in approximate order of abundance; all mineral abbreviations are after Kretz (1983); gah = gahnite; NM = North Broken Hill mine; NBHC = New Broken Hill Consolidated mine; ZC = Zinc Corporation mine; W Long = Western Longitudinal

[2] Whole rock major and REE analysis

[3] LA-ICP-MS analysis of REE in garnet

[4] Whole rock major and REE analysis and LA-ICP-MS analysis of REE in garnet

[5-55] Locations shown in Figure 4

TABLE 2. Major, Metallic, and Rare Earth Element Compositions of Garnet-Bearing Rocks in the Broken Hill Deposit

Sample no.[1]	532-222B	532-334	532-298	532-343	532-599	S76-283	532-83	Blackw5	Blackw8	532-228B	S76-221	532-1
SiO_2	41.86	67.17	44.32	59.15	44.66	71.01	35.17	46.30	37.58	59.34	64.04	56.41
Al_2O_3	31.04	11.62	17.78	12.03	17.35	8.80	10.96	17.33	20.68	13.32	16.06	10.76
Fe_2O_3	19.67	15.00	12.46	23.12	23.22	16.03	11.47	15.48	9.63	22.10	6.27	7.66
MgO	2.79	1.25	0.80	2.18	1.10	2.03	0.24	0.26	0.11	2.48	0.59	1.78
CaO	0.40	0.79	4.45	0.40	1.89	0.41	5.67	2.40	4.87	0.27	3.97	2.45
Na_2O	0.06	0.16	0.02	0.02	0.01	0.03	0.01	0.01	0.01	0.07	0.67	0.44
K_2O	1.67	2.38	0.09	0.25	0.05	0.35	0.04	0.04	0.04	1.12	4.28	3.91
TiO_2	1.02	0.52	0.24	0.40	0.56	0.37	0.37	0.59	0.42	0.49	0.66	0.71
P_2O_5	0.13	0.21	0.49	0.08	0.73	0.09	1.38	0.17	0.07	0.05	0.09	0.05
MnO	1.13	1.16	19.32	2.31	11.94	1.07	25.37	17.49	26.40	1.12	1.90	4.83
LOI	0.1	0.1	0.1	0.1	0.1	0.1	0.2	0.1	0.1	0.1	1.1	1.8
Total C	0.01	0.03	0.05	0.02	0.02	0.03	0.12	0.02	0.02	0.01	0.04	0.01
Total S	0.14	0.10	0.08	1.23	0.06	0.04	0.59	0.05	0.03	1.01	0.32	0.01
Total[2]	99.97	99.57	99.85	98.95	99.92	99.69	99.75	99.66	99.58	99.78	99.65	99.82
La	92.6	18.4	13.2	32.3	16.3	18.6	104.7	38.8	32.0	44.5	57.0	150.1
Ce	200.6	40.8	29.2	71.1	33.9	43.3	220.9	67.0	60.5	93.1	122.9	303.2
Pr	22.22	4.85	3.70	8.16	3.72	4.99	24.71	8.08	8.06	10.38	13.77	32.46
Nd	87.9	19.8	19.0	31.5	16.3	19.1	97.2	32.1	32.7	36.5	49.1	117.1
Sm	14.7	5.1	5.3	6.7	4.9	3.6	14.4	10.2	6.6	6.5	8.7	20.1
Eu	1.90	0.84	2.30	0.84	2.38	0.80	19.55	6.37	7.72	0.99	2.04	4.48
Gd	9.49	5.87	15.92	5.54	6.16	2.84	7.61	11.98	5.36	5.55	7.32	15.29
Tb	1.38	1.15	3.21	1.01	1.10	0.50	0.96	1.66	0.88	0.76	1.30	2.50
Dy	9.03	6.53	17.15	5.93	6.35	2.62	5.00	7.61	5.10	4.52	7.59	11.29
Ho	2.20	1.15	3.04	1.34	1.28	0.48	0.99	1.39	0.97	0.99	1.50	1.79
Er	6.27	3.06	6.56	3.68	3.67	1.36	2.94	3.76	2.68	3.25	4.77	3.97
Tm	0.86	0.43	0.86	0.56	0.56	0.23	0.50	0.59	0.44	0.54	0.75	0.49
Yb	5.04	3.11	5.14	3.39	3.39	1.70	3.17	4.26	3.03	3.04	4.36	2.63
Lu	0.79	0.46	0.66	0.54	0.55	0.30	0.46	0.63	0.51	0.64	0.74	0.35
Ba	193.2	523.3	32.2	23.4	53.8	29.1	4.7	55.1	4.1	230.1	923.1	1255.8
Cu	41.7	40.2	257.2	3470.5	13.1	25.3	200.0	186.6	29.6	564.8	187.7	28.1
Pb	778.1	579.9	263.6	936.6	1941.5	150.1	>10000	5035.4	3347.8	125	953.8	311.8
Zn	66	220	407	4474	93	160	1131	635	108	158	367	65
Eu/Eu*	0.46	0.47	0.60	0.41	1.32	0.71	5.12	1.75	3.83	0.49	0.76	0.75
Ce/Ce*	1.04	1.02	1.00	1.03	1.02	1.07	1.02	0.87	0.87	1.01	1.03	1.01

Sample no.[1]	S77-11	532-29	532-139	532-241	532-335	532-311	532-68	532-117	532-107	532-285	532-21	532-304
SiO_2	63.10	40.20	67.43	73.26	77.34	78.02	43.22	40.65	40.85	56.19	44.53	81.36
Al_2O_3	10.72	19.11	8.43	8.91	1.80	5.98	16.94	19.74	18.49	8.90	17.01	5.03
Fe_2O_3	14.31	10.29	17.67	5.33	4.49	12.03	14.67	30.16	12.88	13.46	13.28	10.13
MgO	1.44	0.22	2.03	0.15	0.12	0.62	2.43	2.60	0.43	1.47	0.75	0.75
CaO	0.28	5.18	0.30	7.95	7.78	0.70	4.24	1.72	5.89	9.21	4.66	0.45
Na_2O	0.07	0.10	0.11	0.05	0.01	0.01	0.07	0.08	0.15	0.12	0.07	0.09
K_2O	0.43	0.04	0.89	0.85	0.04	0.11	0.97	0.05	0.16	0.04	0.24	0.51
TiO_2	0.93	0.64	0.49	0.12	0.08	0.25	0.75	0.77	0.47	0.28	0.79	0.26
P_2O_5	0.04	0.41	0.03	0.08	0.28	0.07	0.05	0.03	0.05	0.00	0.27	0.02
MnO	0.83	23.51	1.30	3.17	3.83	0.97	15.53	5.91	20.41	6.70	18.33	0.84
LOI	1.1	0.1	0.6	0.1	1.2	0.1	0.8	0.1	0.1	0.1	0.1	0.1
Total C	0.04	0.02	0.01	0.02	0.17	0.01	0.01	0.01	0.07	0.01	0.01	0.01
Total S	3.05	0.30	2.00	0.06	1.82	0.70	0.02	0.01	0.03	1.08	0.03	0.61
Total[2]	93.25	99.78	99.26	99.98	97.05	98.57	99.68	99.74	99.83	96.54	100.04	99.55
La	9.3	62.0	5.7	18.0	5.6	3.8	50.6	71.2	96.1	8.6	91.5	5.5
Ce	23.5	156.2	15.4	37.9	13.7	10.0	87.8	149.3	172.4	22.6	174.3	10.9
Pr	2.81	16.43	1.72	4.16	1.72	1.16	9.23	16.6	17.06	3.06	18.52	1.15
Nd	10.0	69.3	6.8	15.5	6.4	4.6	33.1	58.0	59.0	13.4	63.0	4.8
Sm	2.6	12.3	1.8	3.0	1.6	0.8	7.5	12.7	10.0	3.2	11.3	0.7
Eu	0.23	9.76	0.45	1.61	2.12	0.20	7.55	0.45	9.25	1.36	6.83	0.30
Gd	3.03	8.31	2.08	2.37	1.60	0.81	8.20	11.03	10.54	4.53	8.57	0.57
Tb	0.89	1.34	0.56	0.44	0.29	0.13	1.26	3.10	1.79	0.98	1.51	0.08
Dy	6.50	7.03	3.47	2.26	1.26	0.77	5.64	27.19	7.99	5.87	7.91	0.70
Ho	1.67	1.36	0.88	0.52	0.30	0.22	1.02	7.47	1.39	1.30	1.50	0.20
Er	5.20	4.10	2.78	1.34	1.01	0.71	2.51	27.57	3.52	4.28	4.37	0.64
Tm	0.85	0.65	0.44	0.19	0.16	0.15	0.28	4.75	0.56	0.63	0.75	0.11
Yb	5.13	3.82	2.84	1.28	0.99	0.99	2.15	32.47	3.15	3.23	3.57	0.68
Lu	0.96	0.56	0.42	0.21	0.14	0.22	0.29	4.95	0.45	0.48	0.63	0.10
Ba	73.3	1.9	39.2	289.1	11.7	18.4	1288.4	21.2	252.6	4.8	121.1	14.4
Cu	1162.9	348.9	1449.5	13.1	307.0	165.2	2.7	1.8	2.0	1862.3	18.0	1034.8
Pb	>10000	>10000	436.2	794.7	>10000	2011.4	67.4	61.5	71.2	9912.3	1078.8	8722.2
Zn	>10000	964	1313	209	>10000	9933	187	194	59	>10000	247	3695

TABLE 2. *(Cont.)*

Sample no.[1]	S77-11	532-29	532-139	532-241	532-335	532-311	532-68	532-117	532-107	532-285	532-21	532-304
Eu/Eu*	0.25	2.78	0.71	1.78	3.93	0.75	2.92	0.11	2.73	1.09	2.03	1.40
Ce/Ce*	1.10	1.11	1.18	1.02	1.06	1.13	0.92	1.02	0.95	1.06	0.97	1.00

Sample no.[1]	Blackw4	Blackw1	Kintore4	Kintore3	6930-48.5	6925-89.1	Z3293-63.0	Z3512-67.7	6844-47.8m	Z3512-120.2	532-231	532-19
SiO_2	41.75	62.59	67.66	44.15	54.56	82.31	66.07	57.64	35.52	64.76	62.63	37.91
Al_2O_3	19.05	11.55	9.73	18.84	13.98	5.42	11.54	8.76	17.21	10.87	15.02	26.74
Fe_2O_3	13.14	10.71	8.37	12.69	23.05	7.47	14.69	16.58	11.53	16.15	7.37	19.84
MgO	0.34	0.82	0.64	0.68	2.40	1.23	1.44	1.23	1.34	1.84	1.11	1.97
CaO	4.08	2.38	2.00	2.53	0.75	0.34	0.36	0.99	9.68	0.71	5.13	0.89
Na_2O	0.06	0.05	0.03	0.04	0.16	0.22	0.21	0.1	0.09	0.23	0.28	0.2
K_2O	0.04	0.10	0.13	0.12	1.66	0.94	0.61	0.13	0.14	0.93	2.42	2.21
TiO_2	0.34	0.82	0.80	0.40	0.81	0.54	1.02	0.44	2.18	0.52	0.61	1.83
P_2O_5	0.11	0.11	0.05	0.07	0.20	0.04	0.07	0.11	0.30	0.18	0.06	0.03
MnO	20.25	10.05	9.96	20.37	1.70	0.66	0.72	1.93	14.39	1.12	3.74	1.41
LOI	0.6	0.3	0.5	0.1	0.1	0.3	0.1	1.4	0.1	0.3	1.5	0.1
Total C	0.01	0.04	0.05	0.03	0.01	0.01	0.01	0.01	0.04	0.01	0.04	0.01
Total S	0.91	0.05	0.17	0.02	0.78	0.11	0.03	3.71	1.58	1.42	0.06	0.57
Total[2]	99.76	99.48	99.89	99.99	98.78	99.47	96.43	89.31	92.31	97.62	99.87	92.75
La	6.6	53.7	50.7	3.0	23.2	1.6	78.0	8.3	157.6	9.8	101.3	47.1
Ce	15.7	113.9	102.6	7.2	58.6	3.6	191.2	22.0	340.3	23.9	208.5	118.0
Pr	2.74	13.57	11.57	0.97	7.35	0.51	22.7	3.21	38.09	3.21	22.79	13.89
Nd	13.5	51.2	42.7	5.5	29	2.4	83.2	11.5	133.8	13.3	83.6	50.3
Sm	5.1	13.0	9.7	4.6	6.4	0.6	16.6	3.3	25.9	3.6	14.2	10.2
Eu	5.80	8.19	4.58	1.00	0.25	0.06	0.59	0.29	8.03	0.48	3.04	1.40
Gd	5.93	12.49	8.96	8.27	5.50	1.12	11.17	4.23	21.19	3.67	10.05	9.28
Tb	1.00	2.16	1.55	1.49	1.20	0.34	1.69	0.80	3.44	0.73	1.59	2.09
Dy	5.25	12.12	8.29	8.28	7.01	2.53	9.37	4.33	20.99	4.70	8.19	14.59
Ho	0.99	2.41	1.67	1.37	1.43	0.60	1.99	0.84	4.41	0.95	1.41	3.20
Er	2.75	7.15	4.93	4.06	4.48	2.11	6.79	2.50	12.70	3.63	3.56	9.68
Tm	0.41	1.06	0.82	0.58	0.79	0.33	1.02	0.37	1.85	0.52	0.49	1.38
Yb	2.29	6.25	4.34	3.47	4.87	2.23	6.84	2.21	11.94	3.11	2.53	8.98
Lu	0.28	0.99	0.71	0.51	0.72	0.41	1.13	0.34	1.69	0.52	0.39	1.26
Ba	9.2	214.3	193.9	82.8	188.5	136.4	12626.4	49.9	136.3	149.6	745.9	286.1
Cu	143.2	113.8	218.7	8.8	459.7	75.1	7.9	403.8	4744.4	930.8	33.1	335.6
Pb	>10000	2201.2	323	162.3	1989.4	740.9	145.9	>10000	>10000	5014.1	285.3	1788.5
Zn	333	706	245	96	416	531	197	>10000	856	1570	69	708
Eu/Eu*	3.21	1.93	1.47	0.49	0.13	0.22	0.12	0.24	1.01	0.40	0.74	0.43
Ce/Ce*	0.89	1.00	0.99	1.02	1.08	0.96	1.09	1.03	1.03	1.03	1.01	1.10

Notes: Major elements in wt. % and trace elements in ppm.
[1] Sample description given in Table 1.
[2] Total is the sum of oxides and LOI only.

TABLE 3. Average Electron Microprobe Composition of Garnet from Garnet-Bearing Rocks Analyzed by LA-ICP-MS Techniques

Wt %	Blackw4 $n = 12$	Blackw5 $n = 9$	Blackw8 $n = 14$	532-83 $n = 82$	532-45 $n = 9$	532-104 $n = 13$	532-119 $n = 6$	S76-254 $n = 88$
SiO_2	37.11	37.10	37.11	36.71	36.44	37.33	37.09	36.76
TiO_2	0.10	0.05	0.09	0.10	0.10	0.05	0.09	0.07
Al_2O_3	21.50	21.16	21.65	21.08	20.32	21.30	20.19	20.97
FeO	11.64	13.71	8.09	10.00	15.09	16.21	9.30	8.79
MnO	25.54	14.54	29.25	28.26	23.41	23.60	26.28	30.80
MgO	0.41	0.48	0.10	0.21	1.10	0.94	0.26	0.15
CaO	4.27	12.98	4.40	3.82	3.56	1.96	6.34	1.93
Total	100.57	100.02	100.69	100.18	100.02	101.39	99.55	99.47
Number of atoms in formulae (oxygen basis 12)								
Si	2.989	2.962	2.988	2.992	2.970	2.998	2.993	3.011
Ti	0.006	0.007	0.006	0.005	0.006	0.003	0.006	0.004
Al	2.041	1.992	2.054	2.025	1.952	2.015	1.932	2.025
Fe	0.784	0.915	0.545	0.667	1.028	1.088	0.640	0.602
Mn	1.743	0.983	1.995	1.943	1.615	1.605	1.820	2.137
Mg	0.050	0.114	0.012	0.026	0.133	0.112	0.033	0.018
Ca	0.368	1.110	0.379	0.330	0.314	0.169	0.599	0.169
Total	7.981	8.083	7.979	7.988	8.018	7.990	8.023	7.966

Wt %	532-283 $n = 9$	532-313 $n = 4$	6844-47.8 $n = 6$	532-285 $n = 9$	532-284 $n = 4$	532-298 $n = 4$	532-303 $n = 4$	532-311 $n = 4$
SiO_2	36.99	36.56	37.56	37.37	36.76	37.17	36.94	36.99
TiO_2	0.10	0.11	0.05	0.04	0.12	0.05	0.04	0.03
Al_2O_3	21.00	21.21	21.64	20.77	21.02	21.53	21.06	21.39
FeO	16.74	18.55	11.42	12.40	11.00	33.34	35.22	33.85
MnO	17.86	19.94	19.13	18.51	21.99	3.43	2.43	3.37
MgO	0.87	1.23	1.32	0.18	0.36	3.26	2.14	2.55
CaO	6.85	2.84	9.18	10.50	8.80	1.59	2.07	1.95
Total	100.41	100.44	100.30	99.77	100.05	100.37	99.90	100.13
Number of atoms in formulae (oxygen basis 12)								
Si	2.982	2.975	2.984	3.007	2.969	2.978	2.995	2.982
Ti	0.006	0.007	0.003	0.002	0.007	0.003	0.003	0.002
Al	1.986	2.011	2.027	1.970	2.000	2.032	2.012	2.032
Fe	1.128	1.262	0.759	0.834	0.742	2.233	2.385	2.281
Mn	1.219	1.374	1.287	1.262	1.503	0.233	0.167	0.230
Mg	0.104	0.140	0.156	0.022	0.043	0.390	0.258	0.306

TABLE 3. *(Cont.)*

Wt %	532-68 $n = 23$	532-241 $n = 6$	532-500 $n = 72$	532-1 $n = 4$	532-21 $n = 7$	532-316 $n = 5$	532-502 $n = 12$	S76-221 $n = 2$
Ca	0.592	0.247	0.781	0.905	0.761	0.136	0.178	0.168
Total	8.017	8.016	8.000	8.002	8.025	8.005	7.998	8.001

Wt %	532-343 $n = 11$	532-599 $n = 11$	532-2 $n = 18$	532-17 $n = 28$	532-19a $n = 14$	S77-11 $n = 6$	6925-89.1 $n = 10$	Z3293-77.9 $n = 13$
SiO_2	38.03	36.73	37.61	38.04	37.81	37.46	37.45	37.86
TiO_2	0.05	0.03	0.02	0.02	0.02	0.03	0.01	0.02
Al_2O_3	20.01	21.00	21.53	21.68	21.75	21.74	21.82	22.08
FeO	34.18	24.75	34.16	32.55	33.19	33.86	32.67	34.60
MnO	4.65	15.26	4.29	4.82	5.67	4.36	6.02	3.57
MgO	2.88	1.17	3.12	3.85	3.08	2.90	2.82	2.98
CaO	0.53	1.00	0.66	0.68	0.71	0.85	1.02	0.85
Total	100.33	99.94	101.39	101.64	102.23	101.20	101.81	101.96
Number of atoms in formulae (oxygen basis 12)								
Si	3.065	2.995	2.990	2.998	2.983	2.983	2.971	2.985
Ti	0.003	0.002	0.001	0.001	0.001	0.002	0.000	0.001
Al	1.901	2.018	2.018	2.014	2.023	2.041	2.040	2.052
Fe	2.303	1.687	2.271	2.145	2.191	2.255	2.169	2.281
Mn	0.317	1.055	0.289	0.324	0.379	0.294	0.404	0.241
Mg	0.346	0.142	0.368	0.453	0.362	0.344	0.332	0.35
Ca	0.046	0.088	0.057	0.038	0.060	0.072	0.087	0.072
Total	7.981	7.987	7.994	7.973	7.999	7.991	8.003	7.982

Wt %	532-68 $n = 23$	532-241 $n = 6$	532-500 $n = 72$	532-1 $n = 4$	532-21 $n = 7$	532-316 $n = 5$	532-502 $n = 12$	S76-221 $n = 21$
SiO_2	36.57	37.75	36.99	36.81	37.05	36.78	37.45	37.64
TiO_2	0.17	0.09	0.11	0.10	0.21	0.31	0.10	0.02
Al_2O_3	20.51	20.93	21.24	20.76	21.32	20.68	21.68	21.77
FeO	14.72	11.00	8.41	16.30	11.71	18.39	11.44	11.00
MnO	23.87	8.95	29.98	21.78	25.27	19.09	16.04	15.19
MgO	0.38	0.28	0.15	2.11	0.21	0.80	0.48	0.71
CaO	4.21	21.19	3.39	2.39	4.69	4.11	13.07	13.48
Total	100.43	100.19	100.27	100.25	100.46	100.16	100.26	99.81
Number of atoms in formulae (oxygen basis 12)								
Si	2.957	2.970	3.047	2.977	2.99	2.989	2.97	2.981
Ti	0.010	0.005	0.007	0.006	0.001	0.019	0.006	0.002
Al	2.031	1.940	2.030	1.978	2.028	1.977	2.027	2.032
Fe	0.994	0.723	0.600	1.091	0.79	1.248	0.759	0.732
Mn	1.609	0.596	2.087	1.492	1.728	1.314	1.078	1.019
Mg	0.046	0.032	0.019	0.254	0.026	0.098	0.057	0.085
Ca	0.359	1.785	0.295	0.207	0.405	0.358	1.111	1.141
Total	8.006	8.051	8.085	8.005	7.968	8.003	8.008	7.992

Wt %	532-222B $n = 8$	532-84 $n = 19$
SiO_2	37.00	36.71
TiO_2	0.08	0.02
Al_2O_3	20.94	19.51
FeO	35.62	31.24
MnO	3.01	9.33
MgO	2.78	1.16
CaO	0.63	1.08
Total	100.06	99.05
Number of atoms in formulae (oxygen basis 12)		
Si	2.992	3.005
Ti	0.002	0.002
Al	1.996	1.973
Fe	2.409	2.135
Mn	0.207	0.647
Mg	0.334	0.141
Ca	0.055	0.095
Total	7.995	7.998

TABLE 4. Representative Rare Earth Element Concentrations (in ppm) by LA-ICP-MS of Garnet and Apatite in Garnet-Rich Rocks at Broken Hill

Sample no.	La	Ce	Pr	Nd	Sm	Eu	Gd	Tb	Dy	Ho	Er	Tm	Yb	Lu	Eu/Eu*
Blackw4[1]	0.006	0.372	0.012	0.558	1.632	3.418	4.413	0.959	5.475	0.989	2.592	0.312	2.274	0.347	3.657
Blackw5[2]	0.132	0.679	0.501	8.290	20.770	1.768	43.300	7.680	48.580	9.520	27.190	3.980	27.820	3.840	0.923
Blackw6[1]	0.172	0.486	0.066	0.568	0.925	2.794	1.331	0.447	3.388	1.001	2.931	0.304	3.023	0.410	7.672
532-83[3]	0.049	0.236	0.150	1.910	2.020	6.530	3.740		4.430	0.958	2.690	0.464	3.190	0.499	1.178
532-45[1]	0.073	0.397	0.338	7.862	15.622	1.858	26.098	5.540	38.104	8.912	27.770	4.303	30.720	4.647	0.275
532-104[1]	0.014	0.076	0.084	1.642	4.990	0.538	14.510	3.310	24.310	5.310	16.450	2.490	18.330	2.790	0.179
532-110[1]	0.071	0.837	0.258	2.753	2.768	3.205	5.241	1.376	8.387	2.070	5.546	0.863	5.414	0.830	2.500
S76-254[1]	0.009	0.031	0.025	0.249	0.596	1.532	1.383	0.397	1.743	0.415	0.908	0.132	0.835	0.232	4.958
532-283[2]	0.54	1.55	0.263	4.14	2.84	3.21	7.29		8.17	1.91	5.39	0.85	5.66	0.97	2.043
532-313[3]	0.208	0.528	0.136	1.880	2.660	0.638	5.660		13.470	3.440	10.320	1.477	9.400	1.249	1.142
6844-47.8[2]	0.055	0.562	0.215	2.8	3.32	1.739	9.29	2.133	18.57	4.22	12.63	2.001	13.57	1.956	0.894
532-285[3]	0.003	0.172	0.067	1.765	4.370	3.524	13.547	3.489	23.578	5.278	15.122	2.033	13.376	1.849	1.283
532-284[2]	0.158	0.586	0.145	1.810	2.770	2.820	11.910		31.290	7.370	22.850	3.060	18.690	1.840	1.275
532-298[1,2]	0.007	0.106	0.052	1.408	4.325	0.224	14.957	4.544	33.206	6.044	13.525	1.696	10.103	1.280	0.069
532-298[3]	0.020	0.136	0.113	1.770	4.810	0.198	13.400		25.140	5.110	12.940	1.662	10.790	1.444	0.070
532-303[2]	0.030	0.210	0.094	1.717	1.588	0.311	2.150	0.386	2.460	0.623	2.060	0.328	2.350	0.414	0.513
532-311[1]	<0.026	0.087	0.102	1.720	2.070	0.344	2.400		3.260	0.745	2.260	0.454	3.290	0.559	0.469
532-343[3]	<0.0106	0.011	0.009	0.170	0.449	0.293	3.690	1.474	12.970	3.130	9.380	1.315	9.380	1.546	0.482
532-599[3]	0.0243	0.0705	0.0257	0.494	2.037	2.74	4.63	0.696	3.11	0.343	0.414	0.0306	0.115	0.0099	2.629
532-599[2]	0.090	0.112	0.020	0.290	0.846	0.301	4.529	1.250	9.970	2.272	6.630	1.031	7.470	1.196	0.376
532-2[1]	0.063	0.064	-0.016	0.031	0.732	0.172	2.305	0.984	5.435	1.391	3.443	0.496	2.843	0.651	0.370
532-17c[4]	<0.0102	<0.0143	0.009	0.122	0.464	0.275	1.553	0.312	1.366	0.166	0.261	0.032	0.195	0.013	0.883
532-17e[4]	<0.0129	<0.0116	<0.0104	0.168	0.488	0.308	2.100	0.406	2.180	0.306	0.565	0.058	0.212	0.016	0.799
532-10A[1]	<0.047	0.100	<0.047	0.340	1.040	0.920	10.850		12.000	1.000	5.250	0.698	4.050	0.560	0.431
S77-11[2]	<0.0092	0.015	0.023	0.481	1.836	0.406	7.950	3.170	36.490	10.720	35.420	5.670	40.340	6.090	0.275
6025-80.12[2]	<0.046	0.050	0.041	0.670	2.050	0.189	9.320	2.680	19.500	4.120	11.370	1.610	10.610	1.645	0.111
Z3293-77.9[2]	<0.038	<0.038	<0.029	0.231	1.141	0.091	4.48	1.143	8.84	1.723	4.68	0.612	4.3	0.656	0.107
532-68[2]	<0.0256	0.096	0.085	0.900	4.940	4.000	11.260		5.260	0.640	1.510	0.207	1.040	0.170	2.860
532-241[1]	<0.0200	0.042	0.014	0.167	1.135	1.518	3.640		4.160	0.656	1.490	0.208	1.272	0.135	2.077
532-500[3]	0.014	0.076	0.039	0.634	2.310	2.730	5.090	0.746	2.930	0.269	0.388	0.055	0.183	0.021	2.354
532-1[1]	0.070	0.107	0.047	0.530	3.687	1.290	7.783	1.484	9.680	1.903	4.349	0.540	3.050	0.319	0.716
532-21[1]	0.108	0.674	0.155	1.788	6.889	8.745	9.735	1.340	6.854	1.368	3.362	0.563	3.531	0.583	3.254
532-316[3]	0.030	0.278	0.278	5.277	11.912	8.081	11.718	1.702	4.534	0.609	0.841	0.074	0.592	0.054	2.060
532-502[3]	0.006	0.111	0.005	0.000	2.414	5.318	9.668	2.149	14.220	2.959	6.889	1.012	5.419	0.783	2.911
S76-221[1]	4.196	7.430	0.935	4.935	5.045	0.584	24.886	7.970	69.455	19.451	66.691	10.975	82.959	13.412	0.130
532-222B[2]	<0.051	<0.040	<0.045	0.541	1.150	0.17	5.67	1.784	17.75	4.30	11.62	1.488	9.04	1.197	0.167
532-84[1]	0.008	0.030	0.022	0.510	2.341	0.204	12.215	3.904	33.491	8.411	27.638	4.228	31.009	4.527	0.094

Notes: c = center of garnet grain; e = edge of garnet grain

[1] Garnet analyzed at Iowa State University

[2] Garnet analyzed at Macquarie University

[3] Apatite inclusion in garnet analyzed at Macquarie University

Figure 1
Geological map of the Broken Hill deposit. Abbreviations: N.B.H.C = New Broken Hill Consolidated mine (currently part of Southern Operations operated by Perilya Broken Hill Limited), Z.C. = Zinc Corporation mine (currently part of Southern Operations operated by Perilya Broken Hill Limited), B.H.S. = Broken Hill South mine (currently CML7 operated by New Broken Hill Consolidated Limited), and N.B.H. = North Broken Hill mine (currently North mine operated by Perilya Broken Hill Limited).

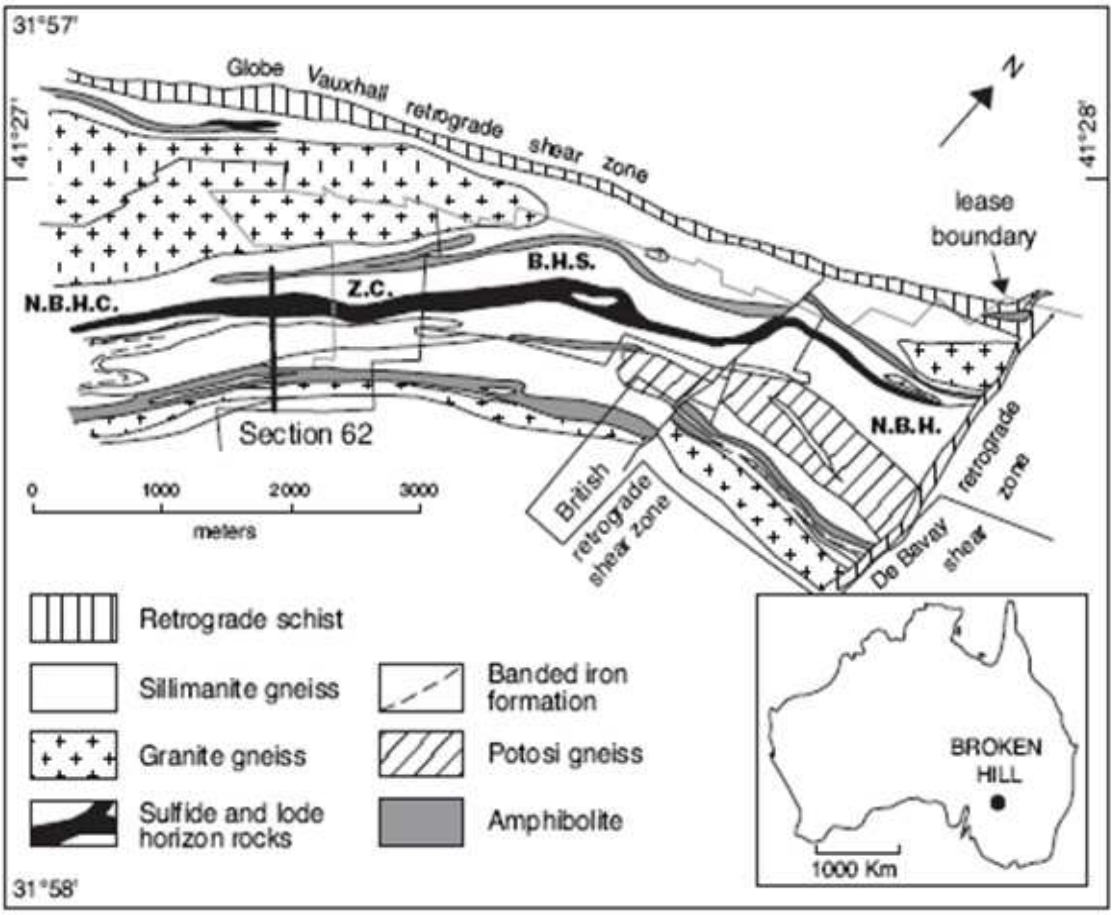

Figure 2
Cross-section (No. 62) though the Broken Hill deposit. The location of the cross-section is shown in Figure 1.

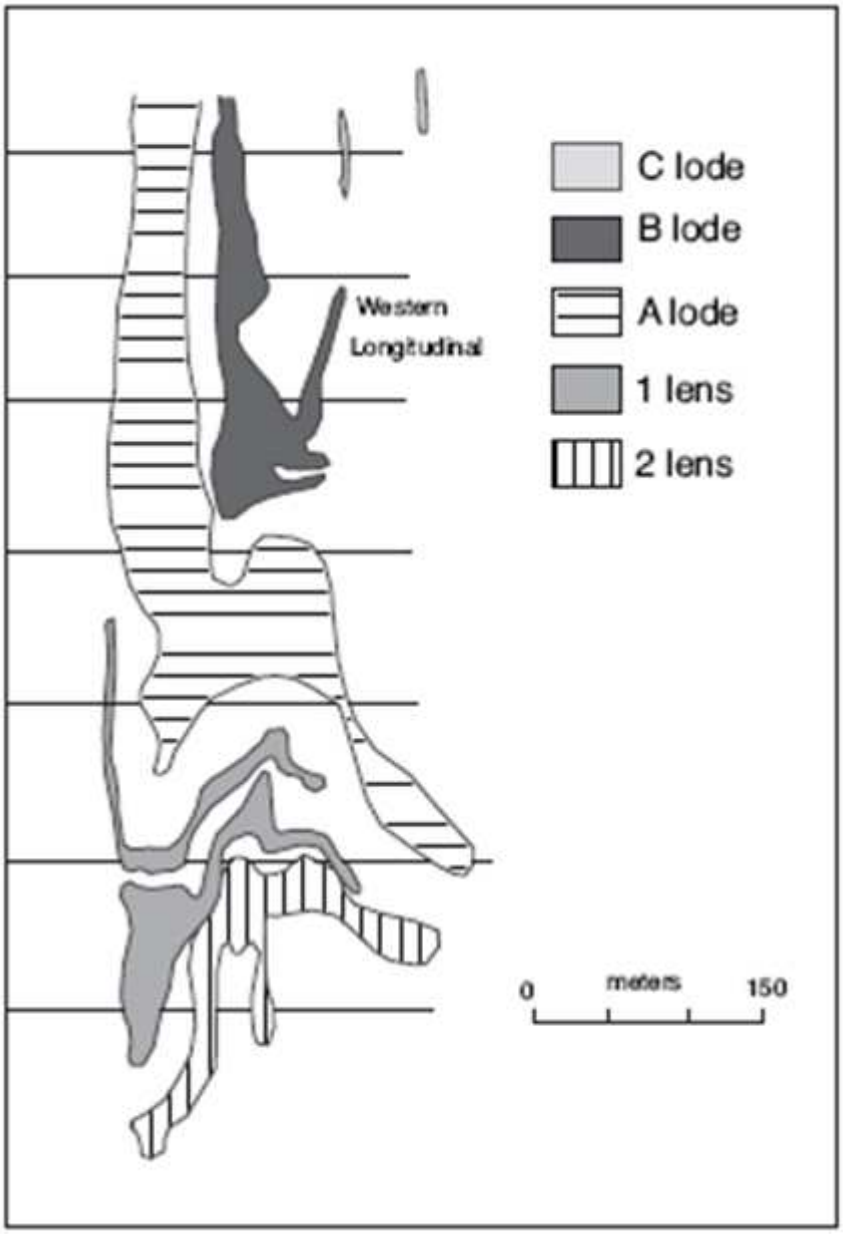

Figure 3

a. Photograph of laminated quartz garnetite (3 lens, North mine, 26 level), b. Photo of massive garnetite (G) cross-cut by later formed "remobilized" quartz garnetite. Garnet in garnetite is < 1 mm in diameter whereas garnet in remobilized quartz garnetite is up to 1 cm in diameter (3 lens, North mine, 26 level), c. Plane polarized photomicrograph of garnetite showing foam textured garnets in contact with quartz-garnetite. The opaque minerals are primarily galena and sphalerite (3 lens, North mine, 27 level), d. Back-scattered electron image of garnets in garnetite. Inclusion in garnet is monazite (Mnz) whereas pyrophanite (Pyf) and chlorite (Chl) occur along grain boundaries (sample 532-29, 3 lens, North mine, 27 level), e. Garnet envelope (GE) surrounding D_3 quartz fluorite vein (Qtz-fl vein) that cross-cuts massive quartz garnetite (MQG) (sample 532-316, 1 lens, North mine, 36 level), and f. Garnets of quartz garnetite showing late-stage metasomatic rims on garnet cores (1 lens, 20 level, New Broken Hill Consolidated mine). The matrix consists of quartz (Qtz) with interspersed sericite (Sc).

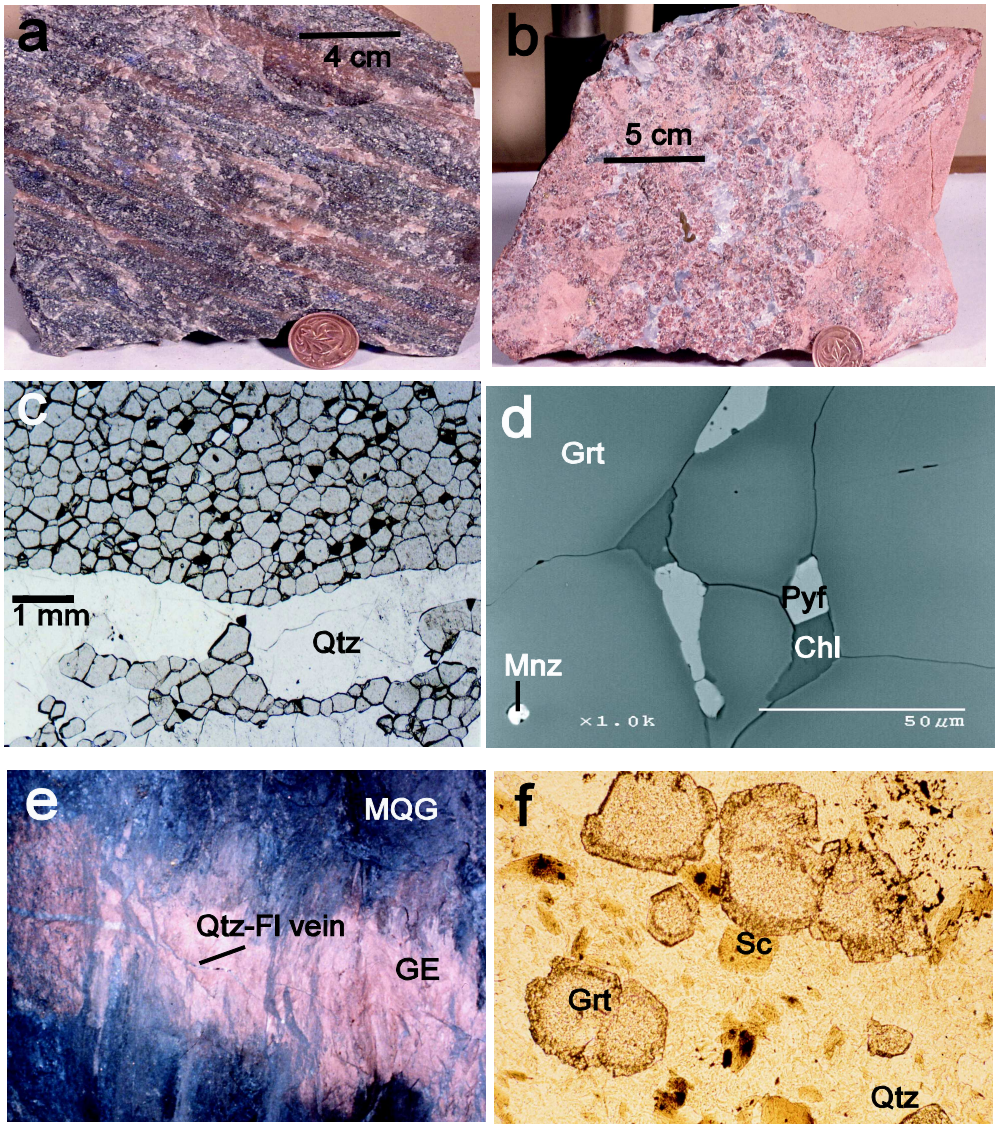

Fig. 4 Spry et al.

Figure 4
Longitudinal projection of the Broken Hill Main Lode showing major ore zones and sample locations that are listed in Table 1 (modified after Burton 1994).

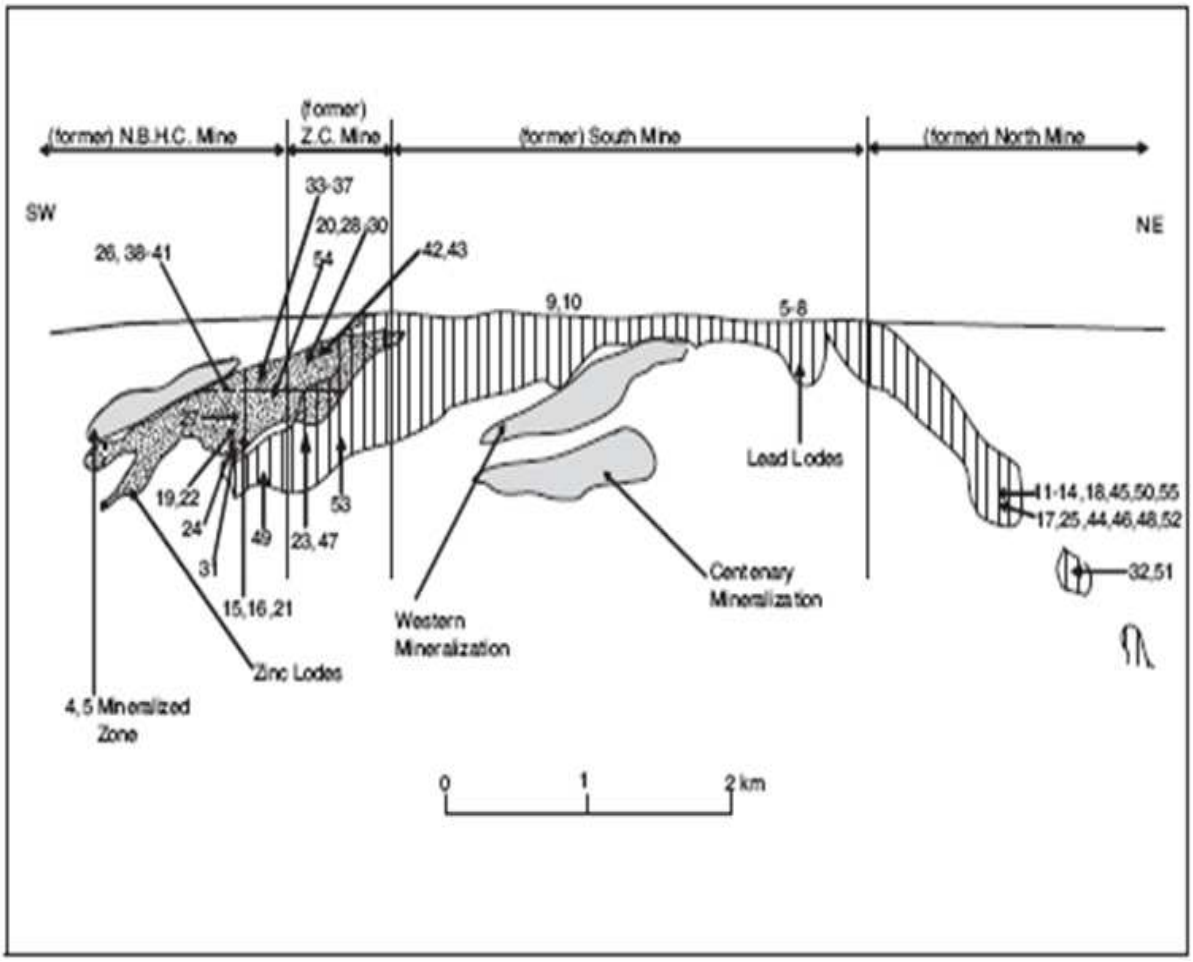

Figure 5

Chondrite-normalized rare earth element patterns of garnet-rich rocks from the Broken Hill deposit. Sample descriptions are given in Table 1. a. Garnetite; b. Garnet-hedenbergite rock (sample 532-285), quartz-garnet-cummingtonite rock (532-335) and sillimanite gneiss (532-222b); c. Massive or laminated quartz garnetite; d. Remobilized quartz garnetite and garnet envelope; e. Blue quartz garnet-gahnite rock from B or C lodes.

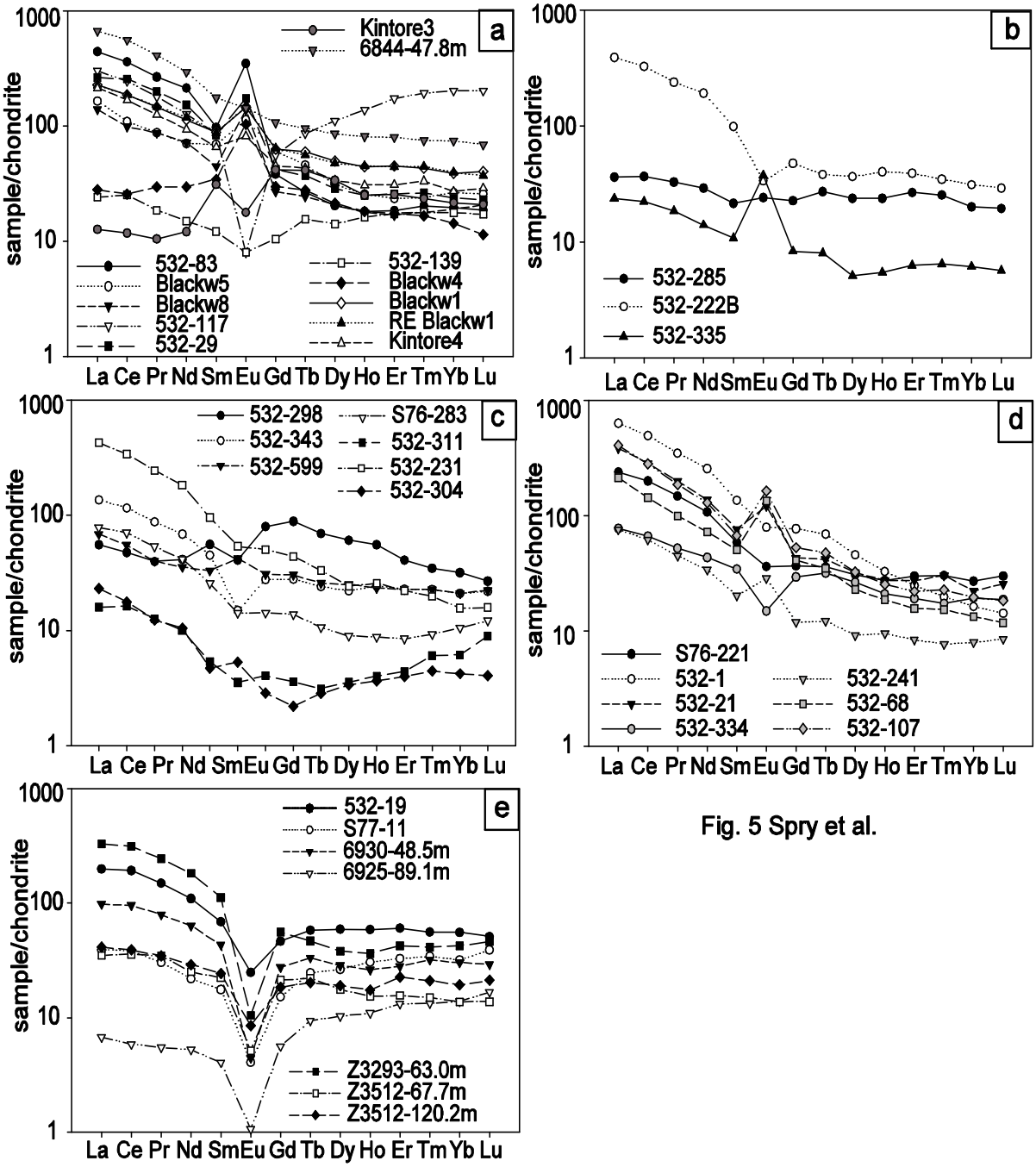

Fig. 5 Spry et al.

Figure 6
Ternary plot of average garnet compositions (EPMA) in terms of spessartine, grossular, and andradite for garnet analyzed by LA-ICP-MS techniques for rare earth elements.

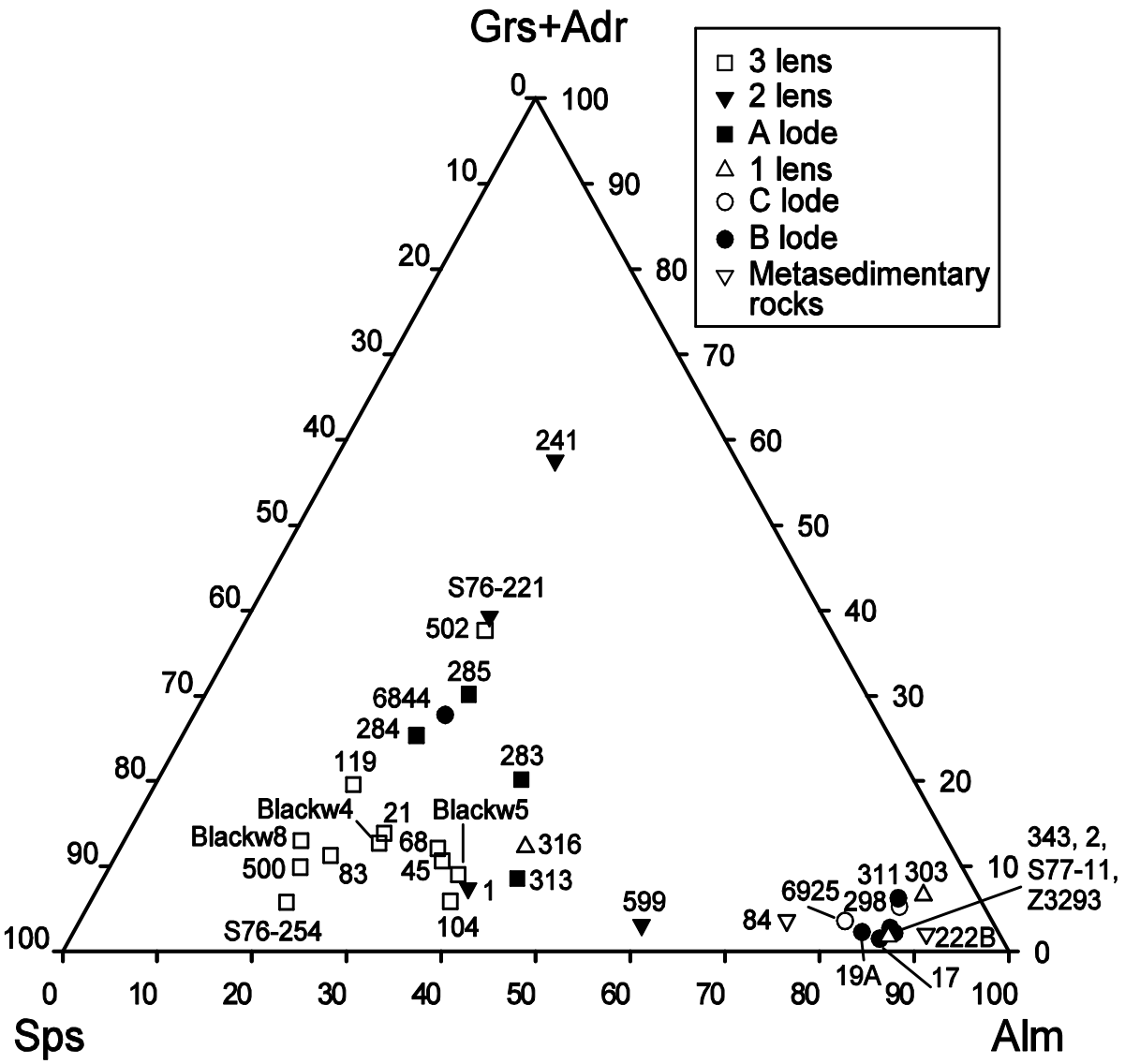

Figure 6 Spry et al.

Figure 7
Chondrite-normalized rare earth element patterns of garnet in garnetite from the Broken Hill deposit. Samples analyzed at Iowa State University are designated by (I) after the sample number whereas those analyzed at Macquarie University are designated by (M). Sample descriptions are given in Table 1.

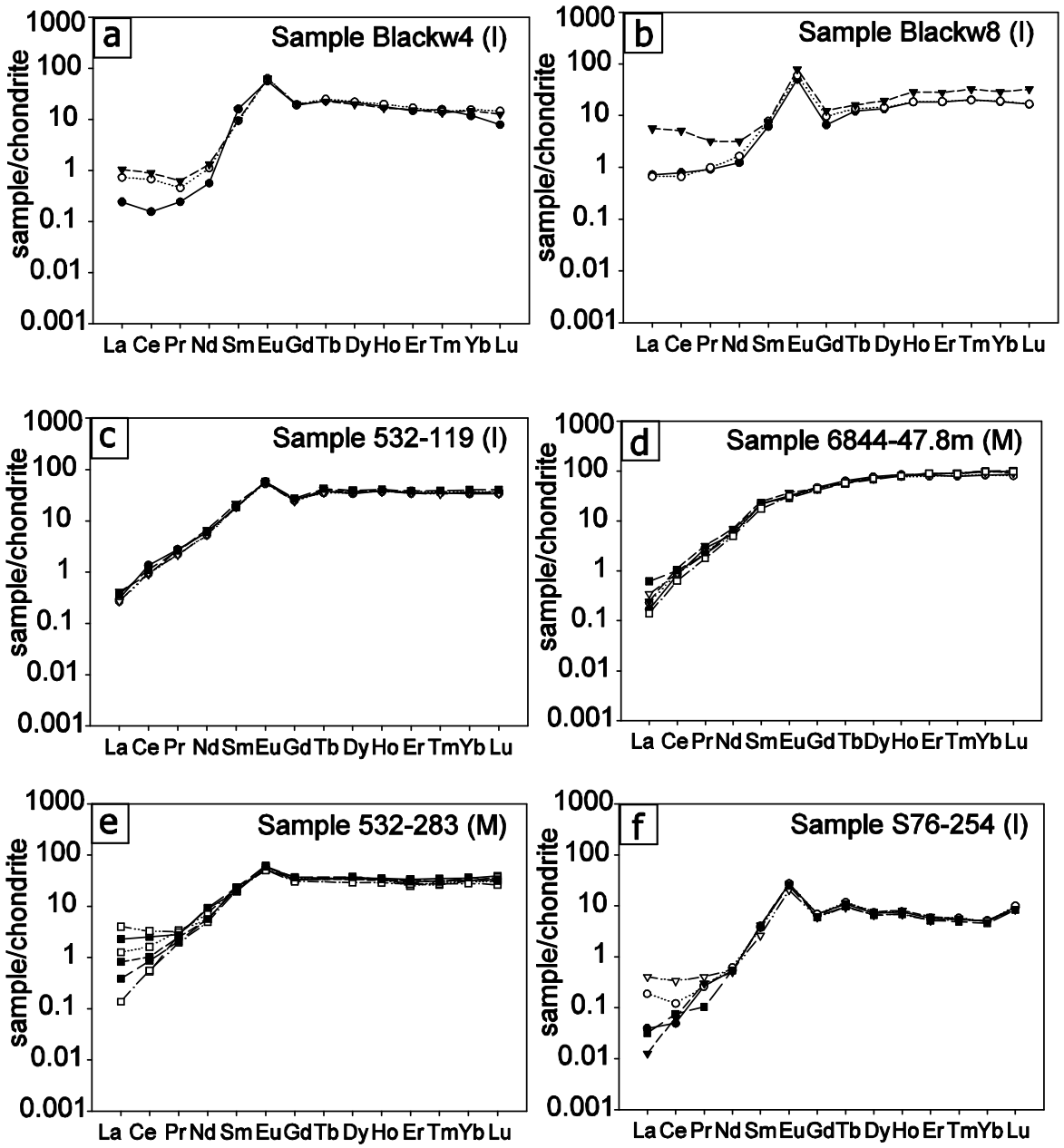

Fig. 7 Spry et al.

Figure 7 (cont)

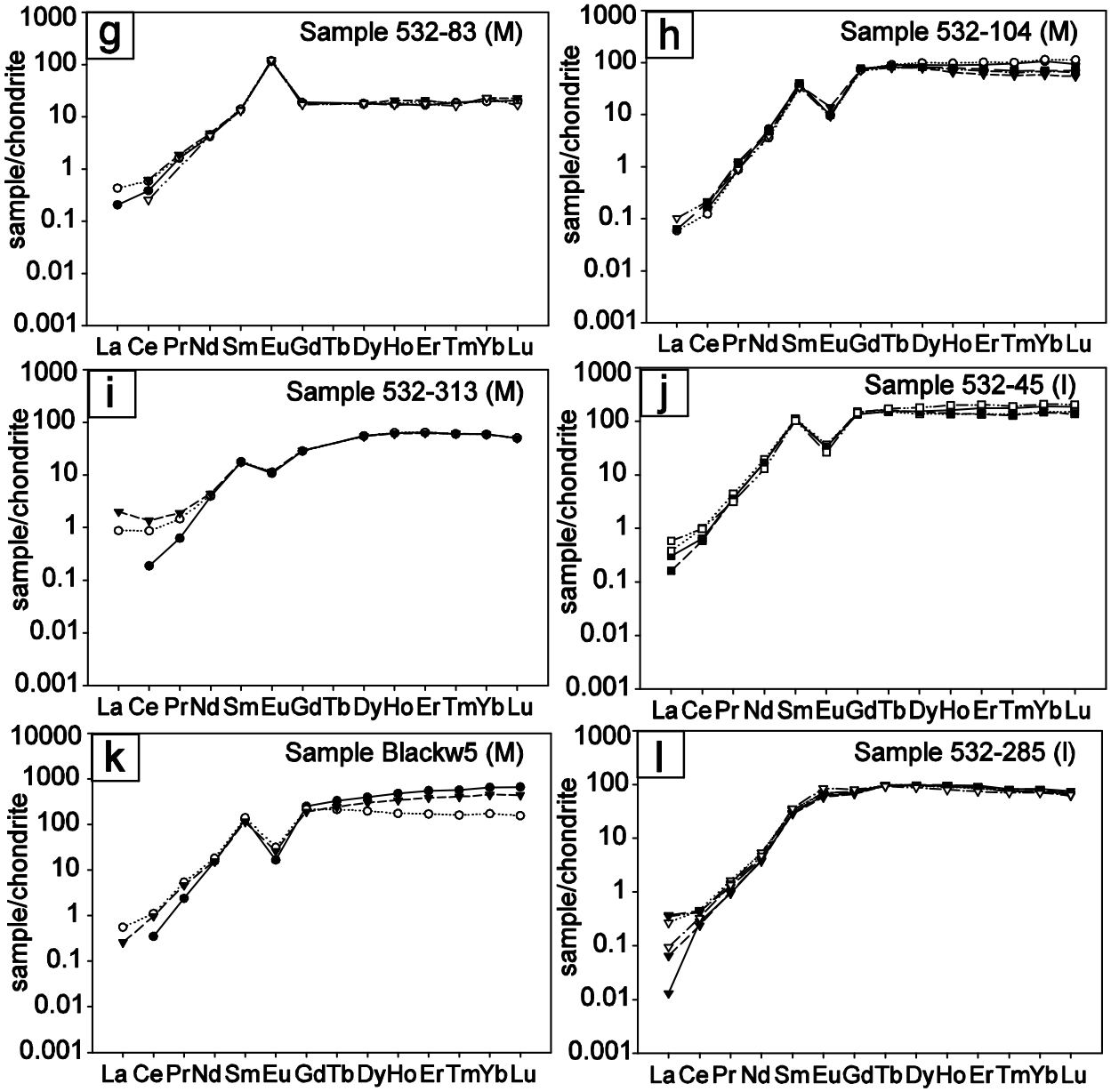

Fig. 7 (cont) Spry et al.

Figure 8
Chondrite-normalized rare earth element patterns of garnet in massive and laminated quartz garnetite and wall rock metasediments (532-222B and 532-84) from the Broken Hill deposit. Sample descriptions are given in Table 1.

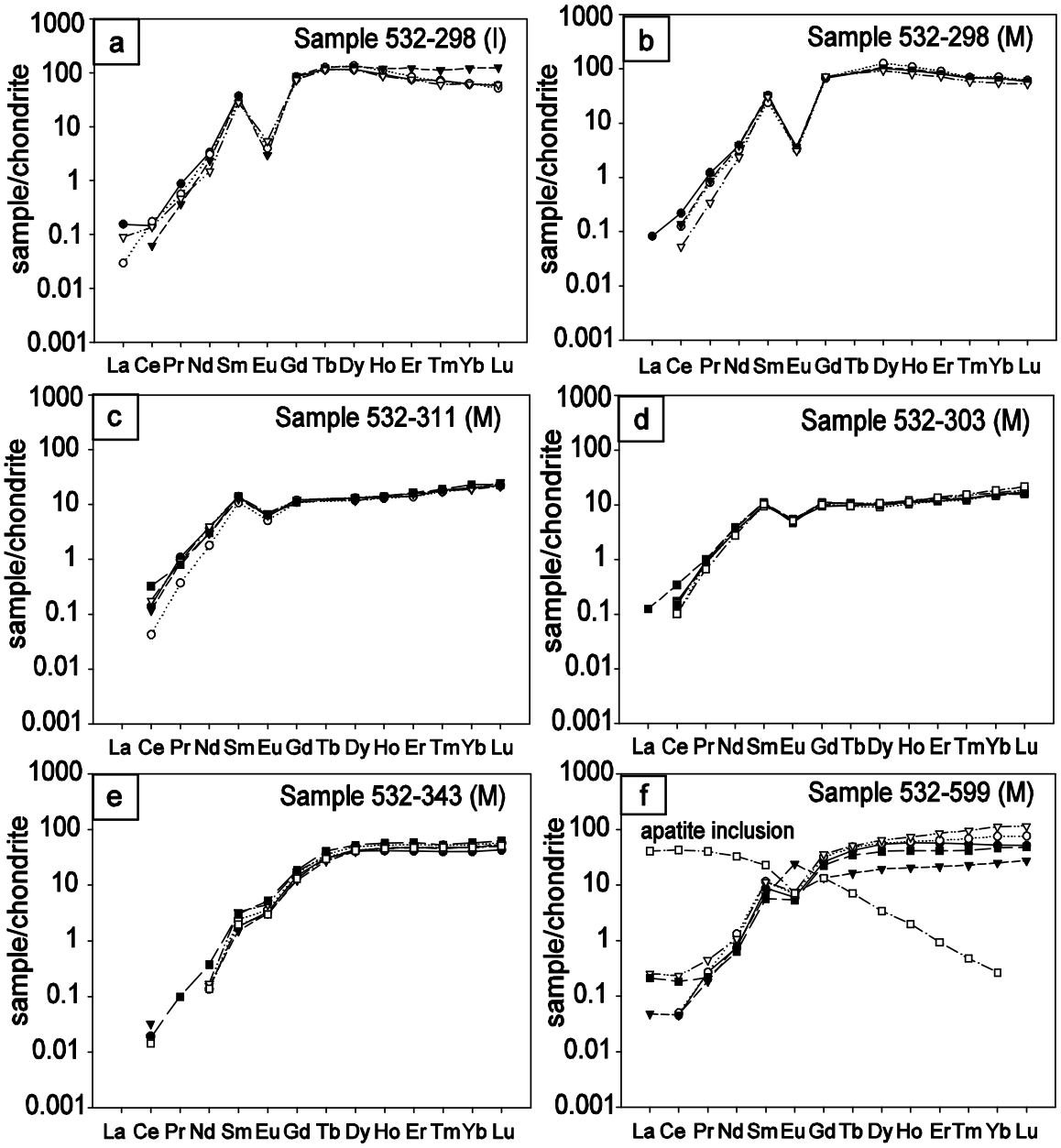

Fig. 8 Spry et al.

Figure 8 (cont)

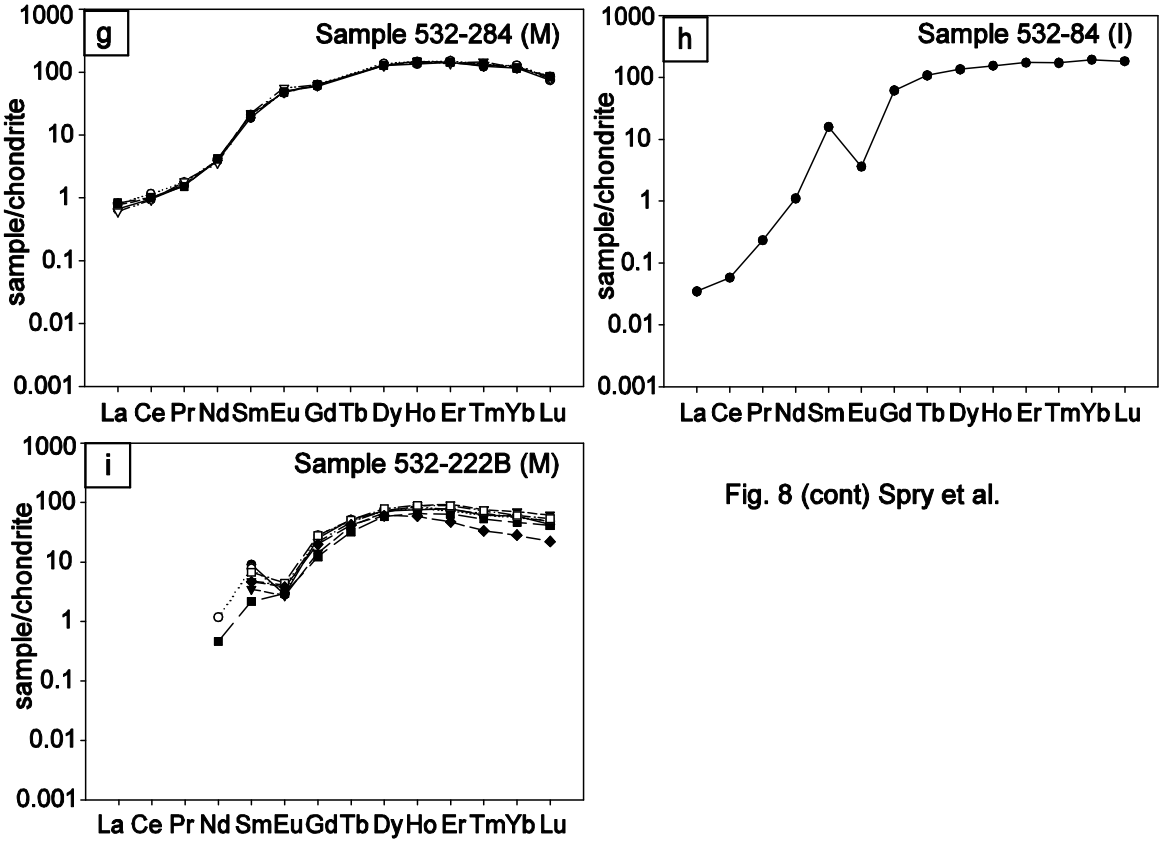

Fig. 8 (cont) Spry et al.

Figure 9
Chondrite-normalized rare earth element patterns of garnet in remobilized quartz garnetite and garnet envelope from the Broken Hill deposit. Sample descriptions are given in Table 1.

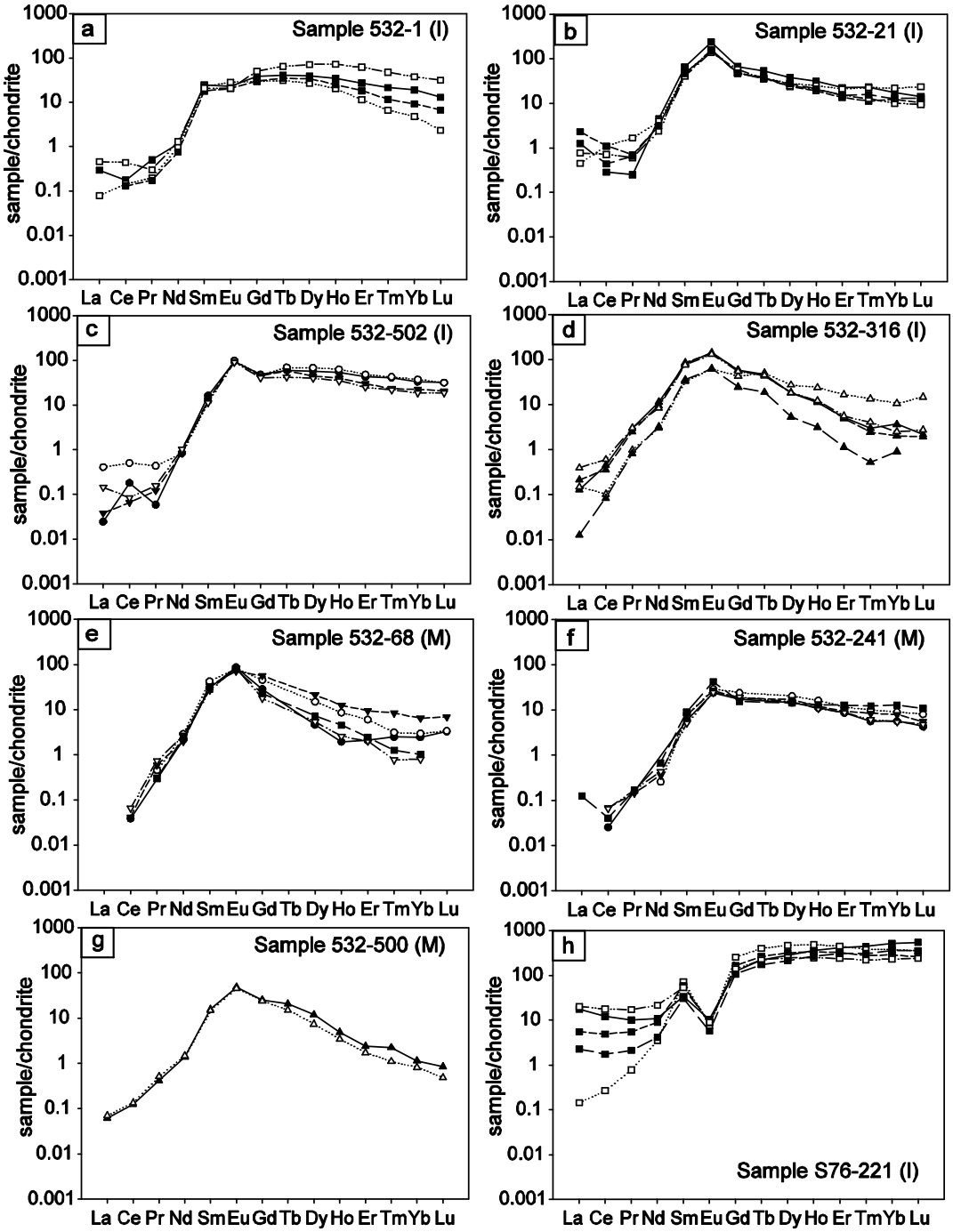

Fig. 9. Spry et al.

Figure 10
Chondrite-normalized rare earth element patterns of garnet in blue quartz-garnet-gahnite rock from B and C lodes from the Broken Hill deposit. Sample descriptions are given in Table 1.

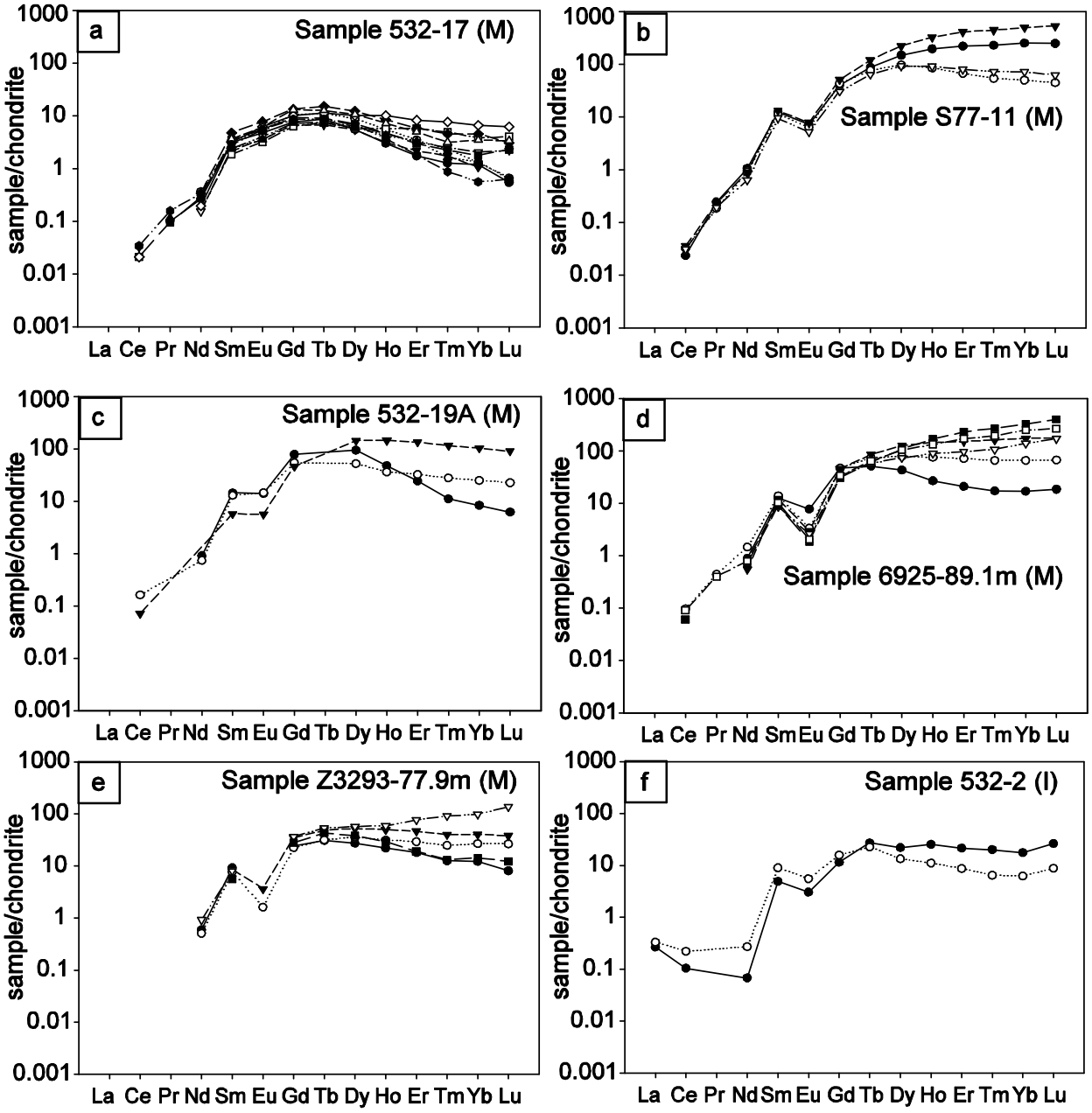

Fig. 10 Spry et al.

APPENDIX TO PAPER

The main data table contains rare earth element concentrations (in ppm) of garnet and apatite in garnet-rich rocks at Broken Hill using laser ablation-inductively coupled plasma-mass spectrometry (LA-ICP-MS). Representative data are given in Table 4 from the paper. A copy of the sample number, lithology, location, and mineralogy table from the paper is included here so that the LA-ICP-MS data can be cross-referenced to this information. The sample numbers in the first column are the same as those listed in Table 1. The data were carried out using a CETAC LSX-500 laser ablation module coupled to a ThermoFinnigan ELEMENT1 ICP-MS instrument at Iowa State University and an Agilent 7500 laser ablation system interfaced with a Merchantek EO-UV laser ablation system at Macquarie University, Sydney. Details of the methodology are given in the paper.

TABLE 1. Lithology, Location and Mineralogy of Garnet-Bearing Rocks Analyzed for REE Studies

Sample	Lithology	Location	Mineralogy[1]	Accessory and trace minerals[1]
Blackw1[2]	Garnetite	Blackwoods pit, hanging wall of 3 lens[5]	Grt, qtz	Mgt, ilm, hem
Blackw4[4]	Garnetite	Blackwoods pit, hanging wall of 3 lens[6]	Grt	Qtz, gn, po, ccp, sp, td, hem
Blackw5[4]	Garnetite	Blackwoods pit, hanging wall of 3 lens[7]	Grt	Qtz, kfs, hm
Blackw6[4]	Garnetite	Blackwoods pit, hanging wall of 3 lens[8]	Grt	Qtz, gn, po, ccp, sp
Kintore 3[2]	Garnetite	Kintore pit, adjacent to 3 lens[9]	Grt	Qtz
Kintore 4[2]	Garnetite	Kintore pit, adjacent to 3 lens[10]	Grt	Qtz
532-29[2]	Garnetite	27 level, 3 lens, 15N stope (NM)[11]	Grt	Qtz, gn, ap, sp, ccp, td
532-82[4]	Laminated garnetite	27 level, 3 lens, 13N stope (NM)[12]	Grt	Qtz, gn, ilm, po, ccp
532-45[3]	Garnetite	27 level, 3 lens, 16 stope (NM)[13]	Grt, sp, qtz	Apy, po, ccp, gn
532-104[3]	Garnetite	27 level, 3 lens, 16 stope (NM)[14]	Grt, sp	Qtz, ccp, gn, py, po
532-117[2]	Garnetite	19 level, 3 lens, 13 stope (NBHC)[15]	Grt	Qtz, chl, bt, ilm, gn, hem
532-119[3]	Garnetite	19 level, 3 lens, 13 stope (NBHC)[16]	Grt	Qtz
532-139[2]	Laminated garnetite	28 level, 3 lens, 14 stope (NM)[17]	Grt	Qtz, po, bt, ilm, ccp, sp, gn, apy
S76-254[3]	Garnetite in ore	27 level, 3 lens, 13 stope (NM)[18]	Grt, gn	Qtz, sp, ccp, apy, po, td
532-283[3]	Garnetite in ore	17 sub-level, A lode, 6 stope (NBHC)[19]	Grt	Qtz, sp, po, gn, ccp
532-313[3]	Garnetite	12 level, A lode (ZC)[20]	Grt, qtz	Sp, gn, po, ccp
6844-47.8[2]	Garnetite	Section 63, 2 lens (NBHC)[21]	Grt	Qtz, bt, ilm, ap
532-285[4]	Hedenbergite-garnet-rock	17 sub-level, A lode, 6 stope (NBHC)[22]	Hd, grt	Qtz, sp, gn, ccp, po, apy, ilm
532-335[2]	Laminated quartz-cummingtonite-garnet rock	17 level, 2 lens (ZC)[23]	Qtz, grt, cum, sp, gn	Wo, cal, ccp, po
532-228B[4]	Massive quartz garnetite	18 level, B lode, H stope (NBHC)[24]	Qtz, grt, bt	St, po, ccp, zrn, ilm, py
532-231[2]	Massive quartz garnetite	28 level, 2 lens (NM)[25]	Qtz, grt	Grn, cal, ep, bt, chl, ap, py, ilm
532-284[3]	Massive quartz garnetite	16 level, A lode (NBHC)[26]	Grt, qtz	Grn
532-298[4]	Massive quartz garnetite	Drill hole 2275 61.2 feet, C lode[27]	Qtz, grt	Grn, po, ilm, gah, ccp, apy
532-303[2]	Massive quartz garnetite	12 level, 1 lens, (ZC)[28]	Qtz, grt	Bt, sp, gn, ccp, po, py, hm
532-304[2]	Massive quartz garnetite	12 level, 1 lens, (ZC)[29]	Qtz, grt	Ilm, bt, sp, gn, po, ccp
532-311[4]	Massive quartz garnetite	12 level, B lode (ZC)[30]	Qtz, grt	Ilm, gn
532-343[4]	Laminated quartz garnetite	20 level, 1 lens, 24 E stope (NBHC)[31]	Grt, qtz	Ccp, ilm, po, sp, gn
532-599[4]	Laminated quartz garnetite	36 level, 2 or 3 lens (NM)[32]	Qtz, grt	Ilm, gn, ep
S76-283[2]	Massive quartz garnetite	13 level, B lode (NBHC)[33]	Qtz, grt,	Bt, po, ms
532-2[3]	Quartz-gahnite-garnet rock	13 level, B lode, W Long (NBHC)[34]	Qtz, gah, grt	Bt, sp, apy, ccp, gn, po
532-17[3]	Garnet-biotite rock	13 level, B lode, W Long (NBHC)[35]	Grt, bt	Gah, qtz, sp, gn, po, ccp, apy
532-19A[4]	Gahnite-garnet-quartz rock	13 level, B lode, W Long (NBHC)[36]	Gah, grt, qtz	Bt, po, sp, ccp, ilm
S77-11[4]	Quartz-garnet-gahnite rock	13 level, B lode, W Long (NBHC)[37]	Qtz, grt, gah	Bt, mgt, po, ccp, apy, chl, ilm
6028-80.1[4]	Quartz-garnet-gahnite rock	Section 41, C lode (NBHC)[38]	Qtz, grt, gah	Bt, ilm, sp, po, gn, ccp, hm
6930-48.4[2]	Garnet-biotite-gahnite rock	Section 41, C lode (NBHC)[39]	Grt, bt, gah	Qtz, sp, po, gn, ccp
Z3293-63.0[2]	Quartz-gahnite-garnet rock	Section 36, C lode (NBHC)[40]	Qtz, grt, gah	Bt, kfs, ms, st, ilm, py, ccp, sp
Z3293-77.9[3]	Quartz-gahnite-garnet rock	Section 36, C lode (NBHC)[41]	Grt, qtz, gah	Bt, ms, ilm, gn, po, ccp
Z3512-67.7[2]	Quartz-gahnite-garnet rock	Section 30, C lode (ZC)[42]	Qtz, grt, gah	Sp, gn, ilm, ccp, po
Z3512-120.2[2]	Quartz-gahnite-garnet rock	Section 30, C lode (ZC)[43]	Qtz, grt, gah	Grn, ccp, po, sp, ilm
532-68[4]	Remobilized quartz garnetite	28 level, 3 lens 15 stope (NM)[44]	Grt, qtz, bt, gn, sp	Ilm, bt, sp, po
532-107[2]	Remobilized quartz garnetite	27 level, 3 lens, 12 stope (NM)[45]	Grt, qtz	Bt, chl, cal, ap, apy, ilm, po
532-241[4]	Remobilized quartz garnetite	28 level, 2 lens (NM)[46]	Grt, qtz	Sp, gn, ccp
532-334[2]	Remobilized quartz garnetite	17 level, 2 lens (ZC)[47]	Grt, qtz, bt	Grn, cp, sp, po
532-500[3]	Remobilized quartz garnetite	38 level, 3 lens, 15 stope (NM)[48]	Grt, qtz	
532-1[4]	Garnet envelope	21 level, lead lode 21 W stope (NBHC)[49]	Grt, qtz, bt, ms	Ilm
532-21[4]	Garnet envelope	27 level, 3 lens 16 stope (NM)[50]	Grt, qtz	Ilm, ap
532-316[3]	Garnet envelope	36 level, 1 lens (NM)[51]	Grt, qz	Mgt, hem
532-502[3]	Garnet envelope	28 level, 3 lens (NM)[52]	Grt, qtz, sp	Td, ccp, gold
S76-221[4]	Garnet envelope	19 level, 2 lens (ZC)[53]	Qtz, grt, bt	Ccp, ilm, po, apy, sp, gn
532-222B[4]	Garnet-sillimanite schist	15 level, B Lode (NBHC)[54]	Grt, sil, bt, qz, st	Ap, ms, po, cp, ilm
532-94[3]	Biotite-muscovite schist	27 level, 3 lens, 13N stope (NM)[55]	Bt, ms, grt, qtz	

[1] Listed in approximate order of abundance; all mineral abbreviations are after Kretz (1983); gah = gahnite; NM = North Broken Hill mine; NBHC = New Broken Hill Consolidated mine; ZC = Zinc Corporation mine; W Long = Western Longitudinal

[2] Whole rock major and REE analysis

[3] LA-ICP-MS analysis of REE in garnet

[4] Whole rock major and REE analysis and LA-ICP-MS analysis of REE in garnet

[5-55] Locations shown in Figure 4

CHAPTER 3

Elemental analysis of automotive filler and caulk by laser ablation inductively coupled plasma mass spectrometry and principal components analysis for use in forensics

A paper to be submitted to the Journal of Forensic Sciences

Josh Messerly, Stan Bajic, David Baldwin, R. S. Houk

Abstract

A study of caulk and automotive filler was done to determine the potential for forensic methods to be developed from these materials. The samples of these materials were prepared and then analyzed by Laser Ablation Inductively Coupled Plasma Mass Spectrometry (LA-ICP-MS). An elemental profile of the samples was produced and evaluated using Principal Components Analysis (PCA). The PCA of filler could differentiate samples by manufacturer and by lot number of both components. The PCA of caulk could differentiate by manufacturer only.

Forensic science uses many different techniques to gain information about a crime scene. One such technique is LA-ICP-MS. This technique allows direct sampling of solids and measurement of their elemental profiles. In this technique, a laser is used to remove a small amount of material that is then transported to the mass spectrometer for analysis. Little or no sample preparation is needed in LA-ICP-MS. The laser is focused onto a small spot (10 to 150 μm) on the sample. The amount of material removed into the mass spectrometer is usually around ng levels per shot. This small amount of material loss is important as both the defendant and the prosecution need to have access to potentially small pieces of evidence. Almost the entire sample survives analysis.

The elemental profile of different materials such as glass (1), paint chips (2, 3), steel (4), and silver (5) has been previously studied. The elemental profiles of material from a vehicle could identify if that vehicle was involved in a hit and run accident, for example. Building materials, such as caulking, may be found on or with a suspect. Matching these materials to others from the crime scene can help determine who was responsible for a crime.

Nearly every vehicle, even new ones, contains some filler. It is used to smooth out dents and bumps before painting. Filler is comprised of two components: polymer resin and a cream hardener. The polyester resin is used in larger amounts than the cream hardener. The hardener acts as a catalyst in creating solid polyester. Each component is manufactured separately and mixed before use.

Caulk is used in a variety of construction projects. It is used to seal joints and cracks. It is also used in waterproofing. Caulk is sold in various containers with the most common being tubes. It also comes in types for different applications, such as mold resistant caulk or waterproof caulk.

Variations in heat, dust levels, and the location where each component is produced can add differences in the amount of trace elements present in each component of filler or caulk. These differences can occur in different lots of material produced in the same location. The variation may only be apparent in the trace elements.

Principal Components Analysis (PCA) was used to analyze data obtained from LA-ICP-MS in this study. PCA compares materials based on their elemental composition using variance in the data (6). This variance is plotted to show similarities or differences between the samples. This can be shown as a two dimensional plot of the variance in a set of results. Each axis shows a principal component that contains a percentage of the variance. The two components with the greatest percentage of the variance in the samples are usually plotted. These figures are called scores plots. PCA can also be used to create a plot of samples compared head to head with a model of another sample. Both methods are used in this

work to find if these materials can be used to either match evidence to a crime scene, or to eliminate evidence from consideration. While matching a suspect to a crime is an obvious goal in forensics, the elimination of suspects can also be of use in narrowing down the number of possible perpetrators.

Methods

Samples of filler were purchased based on their manufacturer and lot number. The samples were prepared according to manufacturer instructions. Filler base to hardener ratio was approximately ten parts base to one part hardener. Samples of caulk were purchased based on their color, manufacturer, intended use, and lot number.

Prepared filler samples and caulking were poured into wooden moulds and the top surface was smoothed by a cleaned glass microscope slide. Stable signals were recorded after four days of hardening.

Instrumental and ablation system parameters are shown in Table 1. The ICP-MS device used to collect data was an ELEMENT 1 ICP-MS produced by ThermoFinnigan. The instrument was tuned daily for maximum sensitivity. In the analysis of each sample, 186 m/z values were monitored. These are shown in Table 2. The laser ablation system used was an LSX-500 produced by Cetac Technologies. It uses a Nd:YAG laser that is frequency quadrupled to 266 nm. Nine m/z scans were taken by the ICP-MS device while the laser system ablated a single line across the sample. Each sample was analyzed on five different days. The PCA comparisons of different samples were done only on data obtained on the same day.

The data obtained from the ICP-MS device were exported into an ASCII file and transferred into PLS – Toolbox software for PCA. The PCA of caulk used the full list of m/z values shown in Table 2.

The list of m/z values used for the analysis of filler is shown in Table 3. Scores plots were generated using this software comparing samples by manufacturer and lot number of their components.

Results and Discussion

Filler results

A sample mass spectrum of filler is shown in Figure 1. In the case of automotive filler, the filler base resin represents a much larger portion of the final filler product. The variance due to the filler base resin was found to dominate the PCA. The base resin elements would overwhelm the contributions from the cream hardener. The filler base resin contains large amounts of Na, Mg, and Al, for example. A LA-ICP-MS analysis of the cream hardener was done separately to determine what elements were present. These elements were included in the PCA along with the trace elements from the filler base. Of the 186 m/z values measured during ablation only 148 were used in the PCA of filler samples.

The PCA scores plot of filler from two different manufacturers is shown in Figure 2. This plot shows that by principal component one (PC1), the two samples of filler that were produced by two different manufacturers are clearly differentiated. Much of the variance (84.58%) in this score plot comes from PC1. This component also shows the clearest differentiation between the samples. Principal component two (PC2) also shows some differentiation. It accounts for 10.53% of the variance in the plot. There is some overlap between the samples in PC2. Combined with PC1, the samples are clearly differentiated.

The PCA scores plot shown in Figure 3 was made using samples created from three different filler base lots produced by the same manufacturer. The filler base was taken from three cans with different lot numbers. Material from each filler base can was mixed with cream hardener from a single tube. This created a comparison of the different filler base lots. This PCA scores plot shows differentiation according to PC1 for all three samples, especially between lots 507291 and 501272. Lots

507291 and 502031 are closer on PC1 but may still be differentiated. Looking at PC1 combined with PC2, lots 507291 and 502031 become clearly differentiated. The scores plot shows clear grouping of the samples by base filler lot number.

The next scores plot, Figure 4, compares two filler bases from different manufacturers with two cream hardeners. The cream hardeners H-A and H-B are from the same lot, but different tubes. The cream hardeners H-412 and H-506 are from different lots. The plot shows that the filler base is the greatest contributor to the variance of the samples. The differences in the filler base give a clear differentiation of Bondo and US Plastics bases. The US Plastics samples are not clearly differentiated from each other, possibly due to each sample containing hardener from the same lot. Both Bondo samples cluster together, but may be differentiated by their hardener using different principal components.

This potential differentiation based on hardener is explored further in Figure 5. Six samples were made using the same filler base resin lot and manufacturer. Each sample was made from tubes of cream hardener with different lot numbers. Every column in the plot shows five samples of the six samples compared to a model of the remaining sample using PCA. This is repeated by using each of the samples as a model and comparing the rest of the samples to it. The Q-residual value shows how closely each sample resembles that model. In this way a direct comparison can be made between samples. The Q-residual value is a number which is generated by the comparison process to show the amount of differentiation between the sample and the model. The larger the Q-residual number, the more different the samples are. The 95 percent and 99 percent confidence limits are shown as lines in the plot with the 99 percent line drawn above that of the 95 percent line. A Q-residual value below that line is indistinguishable from the model at that confidence limit.

This differentiation is shown in Table 4. The numbers shown are the probability that the sample is indistinguishable from the model. A probability of $1x10^{-4}$ would be equivalent to a one in ten thousand chance of the sample being indistinguishable from the model, for example. All of the samples are differentiated from each other using this head to head model. Some samples show a very small probability of being indistinguishable from the other samples in this head to head comparison. Model AJ has the least differentiation from the other samples in this comparison. Its results have a large variance in the score space. The other samples have some resemblance to the model of AJ partly due to this large variance. When sample AJ is compared to the other models, it does not resemble them. This is also due to the large variance.

Caulk Results

The next material that was investigated in this work was caulk. This material differs from the automotive filler in that it does not come in two parts. No mixing is required with caulk. Lot numbers on each tube used were usually different. Some of the tubes of caulk were bound in prepackaged sets. These sets sometimes contained the same or similar lot numbers. The caulk material presented a different type of challenge in this work. The two-part automotive filler provided two materials with potentially different composition. The variations in both components are then mixed in the final material. The caulk samples come from a single lot encoded tube, not the mixing of two materials with individual lot numbers. This may result in less variation, as discussed later. A sample mass spectrum of caulk is shown in Figure 6.

First, PCA was done on caulk samples that were visually indistinguishable, but were from different manufacturers. This PCA scores plot is shown in Figure 7. The caulk was purchased as four tubes of caulk packaged together from each manufacturer. Samples BZ through CC were from lot WC171-1 and were made by Henkel. Samples CD through CG were from lot 16115 and were made by

DAP. As can be seen by this plot, the two manufacturers can be distinguished from each other. The PC1 shows some differentiation between the samples, but the combination of PC1 and PC2 gives even more differentiation.

The next step in the investigation of caulk was a comparison of caulk samples from a single manufacturer. This comparison was done using four tubes of caulk from the manufacturer DAP. This caulk came from a four-pack of two sets of tubes with the same lot number. The lot numbers of the four tubes were same except for the last two digits. The scores plot in Figure 8 shows the PCA results for this set of samples. In the space of this plot, the samples show considerable spread and overlap. This perhaps may be expected with samples that come from the same or similar lot numbers. The red circles shown for the second of the 1430 samples cluster near the lower left portion of the plot, while the black squares of the other 1430 sample are spread out much more than any other sample. The 1453 lot samples are clustered together in the central and upper portion of the plot, and overlap with the black squares of the first 1430 sample. While there may be some small amount of differentiation between some samples with the same or nearly the same lot numbers, no clear difference can be seen.

Conclusion

The two materials tested in this investigation showed some differentiation when subjected to PCA. The automotive filler showed differentiation by both manufacturer and lot number. The combination of filler base resin and cream hardener created a mixing of the small variations of elements contained in each. These variations were present at the lot level. The combination of these variations created a unique signature that allowed for the differentiation of samples by PCA.

The caulking material tested did not have the same level of differentiation as the automotive filler. The different caulks showed differentiation by manufacturer using PCA. They did not, however,

show significant differentiation by lot within an individual manufacturer. This may be of limited interest in forensic study. One possible future investigation of caulking would be to see if environmental factors at the installation site cause a differentiation in the material. Perhaps this could be seen using PCA. Differentiation could also potentially be caused by weathering. Dust or other contaminants could adhere to the outer surface of the caulk, and could add some variance to the model based on the local environment. A combination of manufacturing and environmental variances could give a specific pattern of variance that could be detected in future investigations. These investigations are outside the scope of this project. This investigation focused on the variance caused by the manufacturing process and the preparation of materials for use.

Use of these findings may be of use for the matching of evidence. The differentiation of samples based on lot number or manufacturer presented here does not allow for the matching of evidence by itself. Such matching would require a larger amount of study. Many more analyses would need to be performed and a database of materials would need to be evaluated for such matching. The results presented here is a first step in classifying these materials. These results show the potential of these materials to be of possible future use in forensics.

Acknowledgements

Ames Laboratory is operated for the U.S. Department of Energy by Iowa State University under Contract No. DE-AC02-07CH11358. This work was supported by the U.S. Department of Justice and the Midwest Forensics Resource Center. This study was done with the collaboration of the Wisconsin State Crime Lab in Madison, WI.

References

1. Bajic S J, Aeschliman D B, Saetveit N J, Baldwin D P, Houk R S. Analysis of glass fragments by laser ablation-inductively coupled plasma-mass spectrometry and principal component analysis. J. Forensic Sci. 2005;50:1123-1127.
2. Hobbs A L, Almirall J R. Trace elemental analysis of automotive paints by laser ablation-inductively coupled plasma-mass spectrometry (LA-ICP-MS). Anal. Bioanal. Chem. 2003;376:1265-1271.
3. Deconinck I, Latkoczy C, Guenther D, Govaert F, and Vanhaecke F. Capabilities of laser ablation-inductively coupled plasma mass spectrometry for (trace) analysis of car paints for forensic purposes. J. Anal. At. Spectrom. 2006;21:279-287.
4. Watling R J, Lynch B F, and Herring D. Use of laser ablation inductively coupled plasma mass spectrometry for fingerprinting scene of crime evidence. J. Anal. At. Spectrom. 1997;12:195-203.
5. Devos W, Moor Ch, Lienemann P. Determination of impurities in antique silver objects for authentication by laser ablation inductively coupled plasma mass spectrometry (LA-ICP-MS). J. Anal. At. Spectrom. 1999;14:621-626
6. Geladi P, Grahn H. Multivariate image analysis. Chichester: John Wiley & Sons Ltd., 1996.

Table 1

Instrumental and ablation system parameters

ICP-MS parameters Operated in low resolution mode (m/Δm ≈ 300) Ar cool gas flow rate - 16.00 L/min Ar auxiliary gas flow rate - 0.70 L/min Ar carrier gas flow rate - 1.10 to 1.30 L/min Laser ablation parameters Operated in single line ablation mode Laser spot diameter – 100 μm Shot repetition rate – 2 Hz Laser spot movement rate – 50 μm/second

Table 2

Masses monitored during ablation

Li6, Li7, Be9, B10, B11, Na23, Mg24, Mg25, Mg26, Al27, Ca42, Ca43, Ca44, Sc45, Ti46, Ti47, Ti48, Ti49, Ti50, V51, Cr52, Cr53, Fe54, Mn55, Fe57, Ni58, Co59, Ni60, Ni61, Ni62, Cu63, Zn64, Cu65, Zn66, Zn67, Zn68, Ga69, Ge70, Ga71, Ge72, Ge73, Ge74, As75, Se76, Se77, Se78, Br79, Br81, Se82, Kr83, Kr84, Rb85, Sr86, Rb87, Sr88, Y89, Zr90, Zr91, Zr92, Nb93, Zr94, Mo95, Mo96, Mo97, Mo98, Ru99, Ru100, Ru101, Ru102, Rh103, Ru104, Pd105, Pd106, Ag107, Pd108, Ag109, Cd110, Cd111, Cd112, Cd113, Cd114, In115, Sn116, Sn117, Sn118, Sn119, Sn120, Sb121, Sn122, Sb123, Sn124, Te125, Te126, I127, Te128, Xe129, Te130, Xe131, Xe132, Cs133, Xe134, Ba135, Ba136, Ba137, Ba138, La139, Ce140, Pr141, Nd142, Nd143, Nd144, Nd145, Nd146, Sm147, Sm148, Sm149, Sm150, Eu151, Sm152, Eu153, Sm154, Gd155, Gd156, Gd157, Gd158, Tb159, Gd160, Dy161, Dy162, Dy163, Dy164, Ho165, Er166, Er167, Er168, Tm169, Er170, Yb171, Yb172, Yb173, Yb174, Lu175, Yb176, Hf177, Hf178, Hf179, Hf180, Ta181, W182, W183, W184, Re185, W186, Re187, Os188, Os189, Os190, Ir191, Os192, Ir193, Pt194, Pt195, Pt196, Au197, Hg198, Hg199, Hg200, Hg201, Hg202, Tl203, Pb204, Tl205, Pb206, Pb207, Pb208, Bi209, Th230, Pa231, Th232, U233, U234, U235, U236, U238, ThO248, UO254

Table 3

Masses used in PCA of filler

Ca42, Ca43, Ca44, Sc45, V51, Cr52, Cr53, Mn55, Co59, Ni60, Ni61, Ni62, Cu63, Cu65, Zn67, Ga69, Ge70, Ga71, Ge72, Ge73, Ge74, As75, Se76, Se77, Se78, Br79, Br81, Se82, Kr83, Kr84, Rb85, Sr86, Rb87, Sr88, Y89, Zr90, Zr91, Zr92, Nb93, Zr94, Mo95, Mo96, Ag107, Pd108, Ag109, Cd110, Cd111, Cd112, Cd113, Cd114, In115, Sn116, Sn117, Sn118, Sn119, Sn120, Sb121, Sn122, Sb123, Sn124, Te126, I127, Te128, Xe129, Te130, Xe131, Xe132, Cs133, Xe134, Ba135, Ba136, Ba137, Ba138, La139, Ce140, Pr141, Nd142, Nd143, Nd144, Nd145, Nd146, Sm147, Sm148, Sm149, Sm150, Eu151, Sm152, Eu153, Sm154, Gd155, Gd156, Gd157, Gd158, Tb159, Gd160, Dy161, Dy162, Dy163, Dy164, Ho165, Er166, Er167, Er168, Tm169, Er170, Yb171, Yb172, Yb173, Yb174, Lu175, Yb176, Hf177, Hf178, Hf179, Hf180, Ta181, W182, W183, W184, Re185, W186, Os188, Ir193, Pt194, Pt195, Au197, Hg198, Hg199, Hg200, Hg201, Hg202, Tl203, Pb204, Tl205, Pb206, Pb207, Pb208, Bi209, Th230, Pa231, Th232, U233, U234, U235, U236, U238, ThO248, UO254

Table 4

Probability of sample being indistinguishable from model

	Sample AF	Sample AG	Sample AH	Sample AI	Sample AJ	Sample AK
Model AF	…	$<10^{-14}$	7×10^{-14}	$<10^{-14}$	$<10^{-14}$	2×10^{-7}
Model AG	8×10^{-6}	…	1×10^{-8}	2×10^{-8}	$<10^{-14}$	5×10^{-5}
Model AH	$<10^{-14}$	$<10^{-14}$	…	$<10^{-14}$	$<10^{-14}$	$<10^{-14}$
Model AI	$<10^{-14}$	$<10^{-14}$	$<10^{-14}$	…	$<10^{-14}$	$<10^{-14}$
Model AJ	1×10^{-4}	9×10^{-10}	2×10^{-4}	2×10^{-6}	…	5×10^{-5}
Model AK	$<10^{-14}$	$<10^{-14}$	$<10^{-14}$	$<10^{-14}$	$<10^{-14}$	…

Figure 1
Sample spectrum of filler

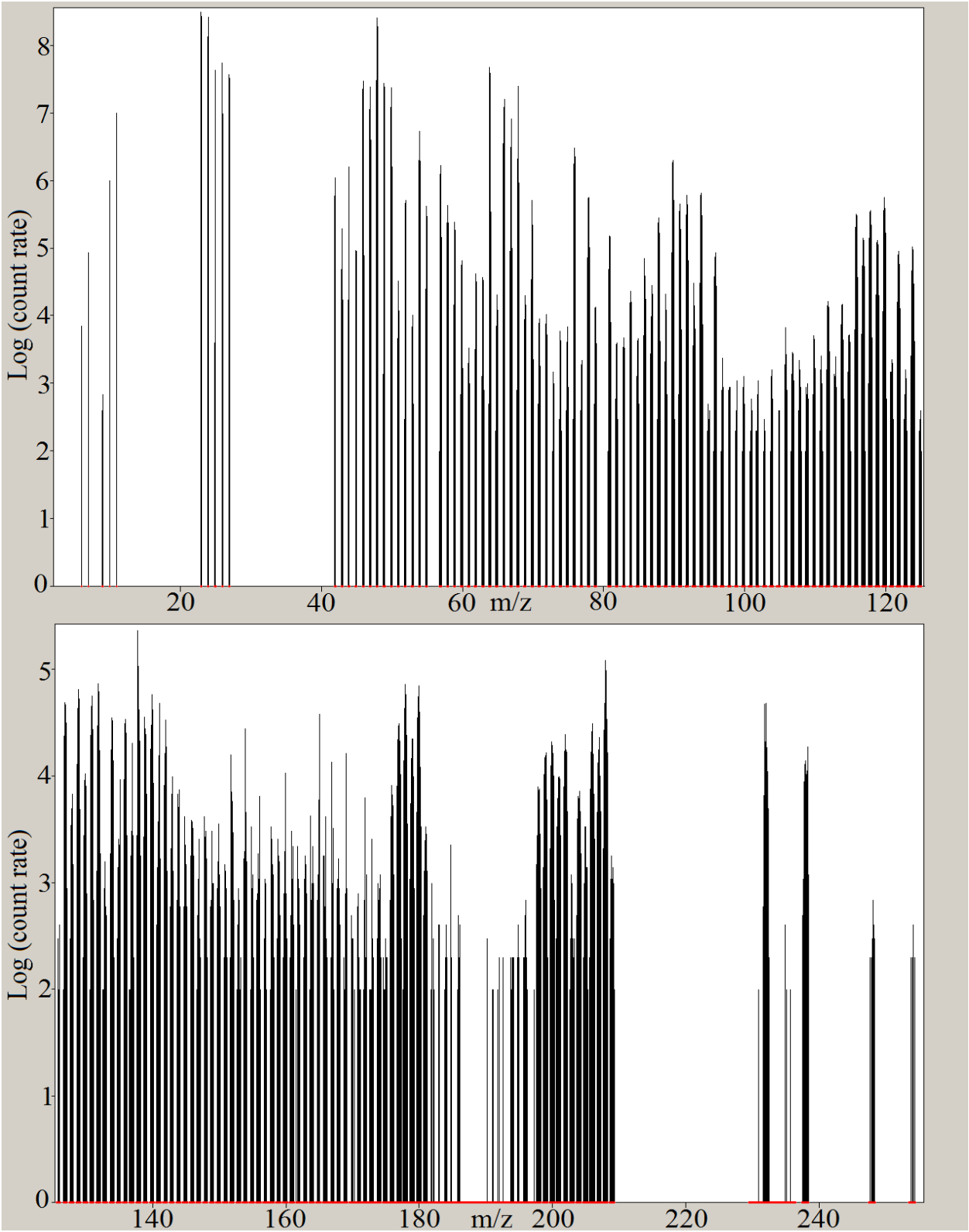
Log (count rate)
0
1
2
3
4
5
6
7
8
20
40
60
m/z
80
100
120
Log (count rate)
0
1
2
3
4
5
140
160
180
m/z
200
220
240

Figure 2

Filler manufacturer comparison

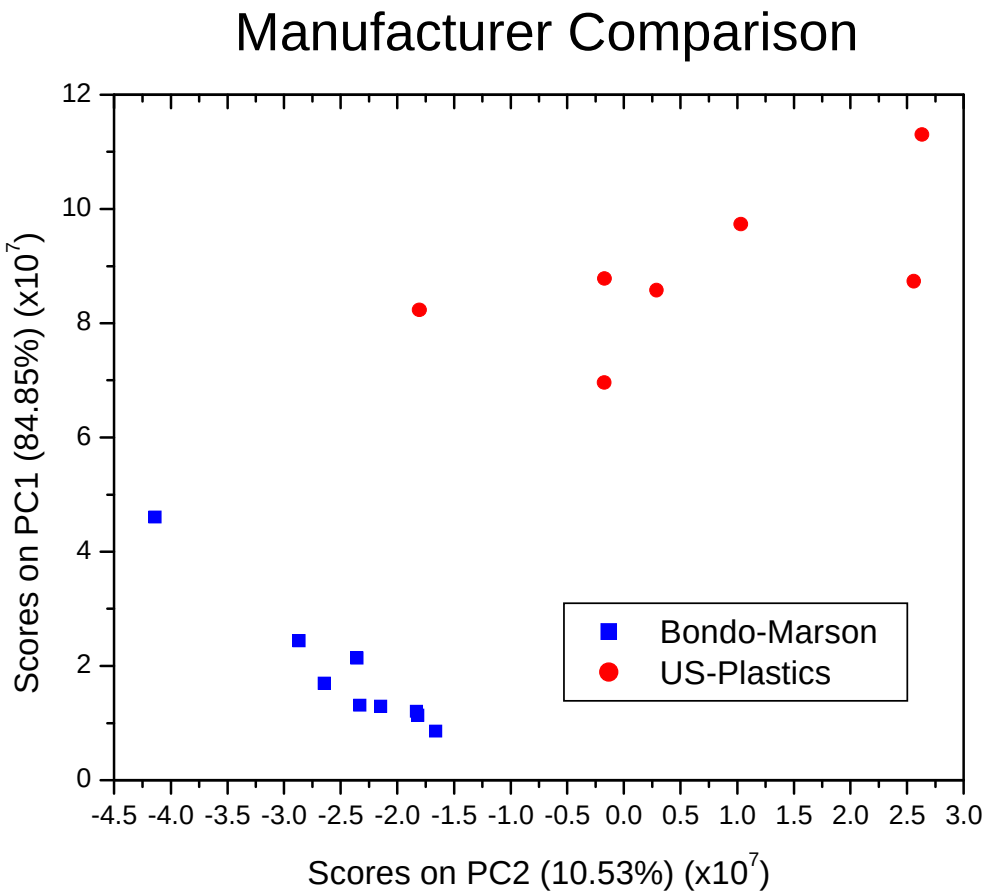

Figure 3

Hardener mixed with different filler base lots

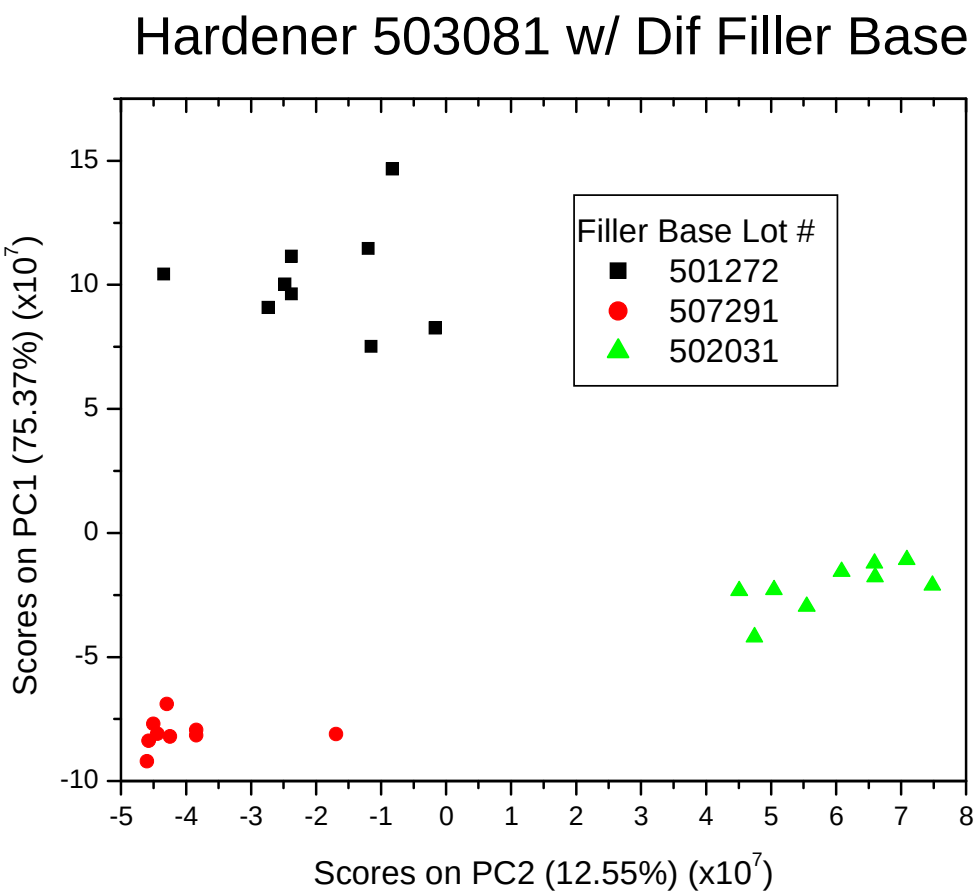

Figure 4

Plot of two manufacturers and two hardeners

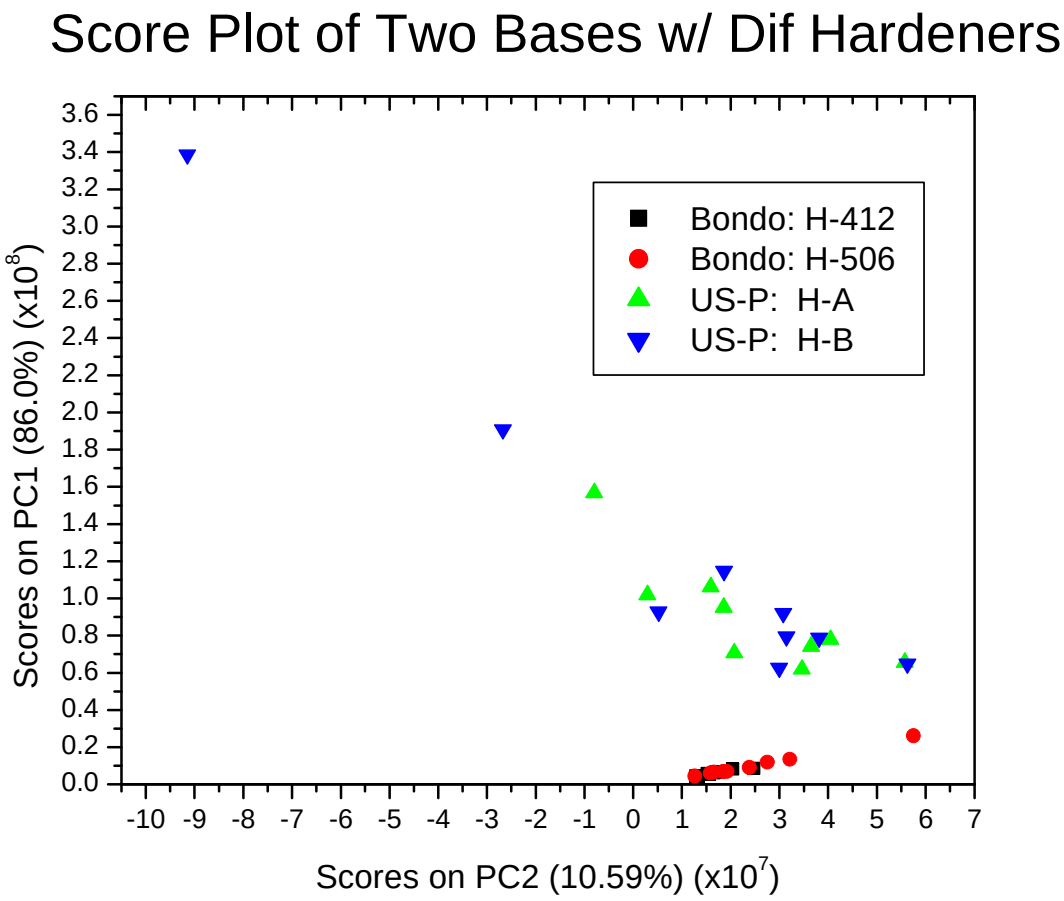

Figure 5

Q-residual comparison

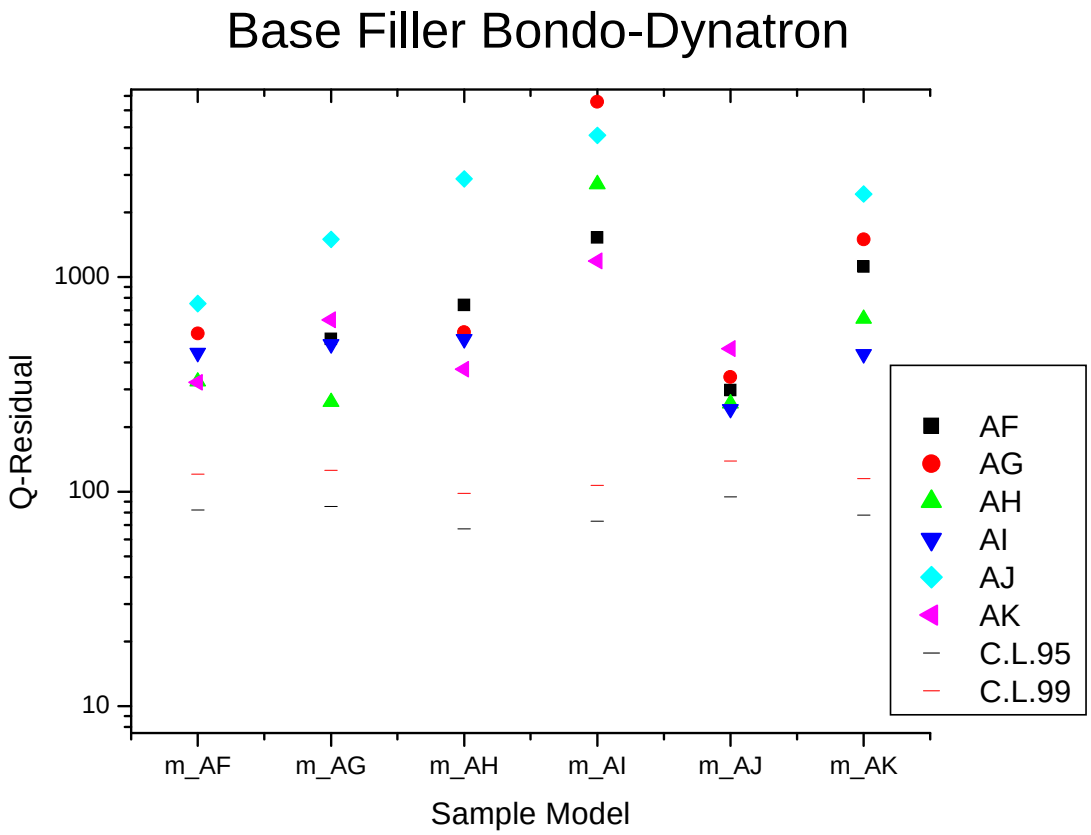

Figure 6

Sample spectrum of caulk

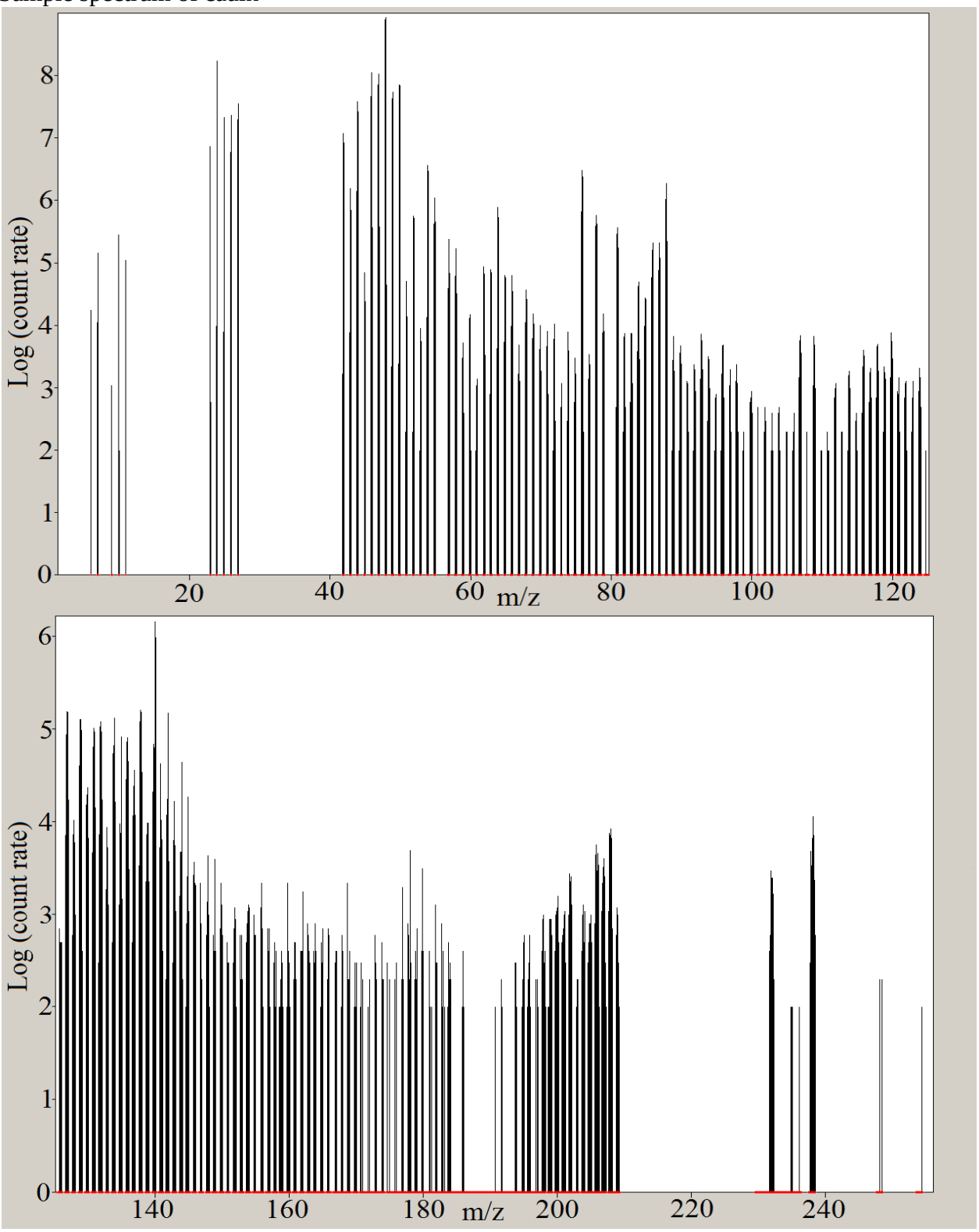

Figure 7
Comparison of two different caulk manufacturers

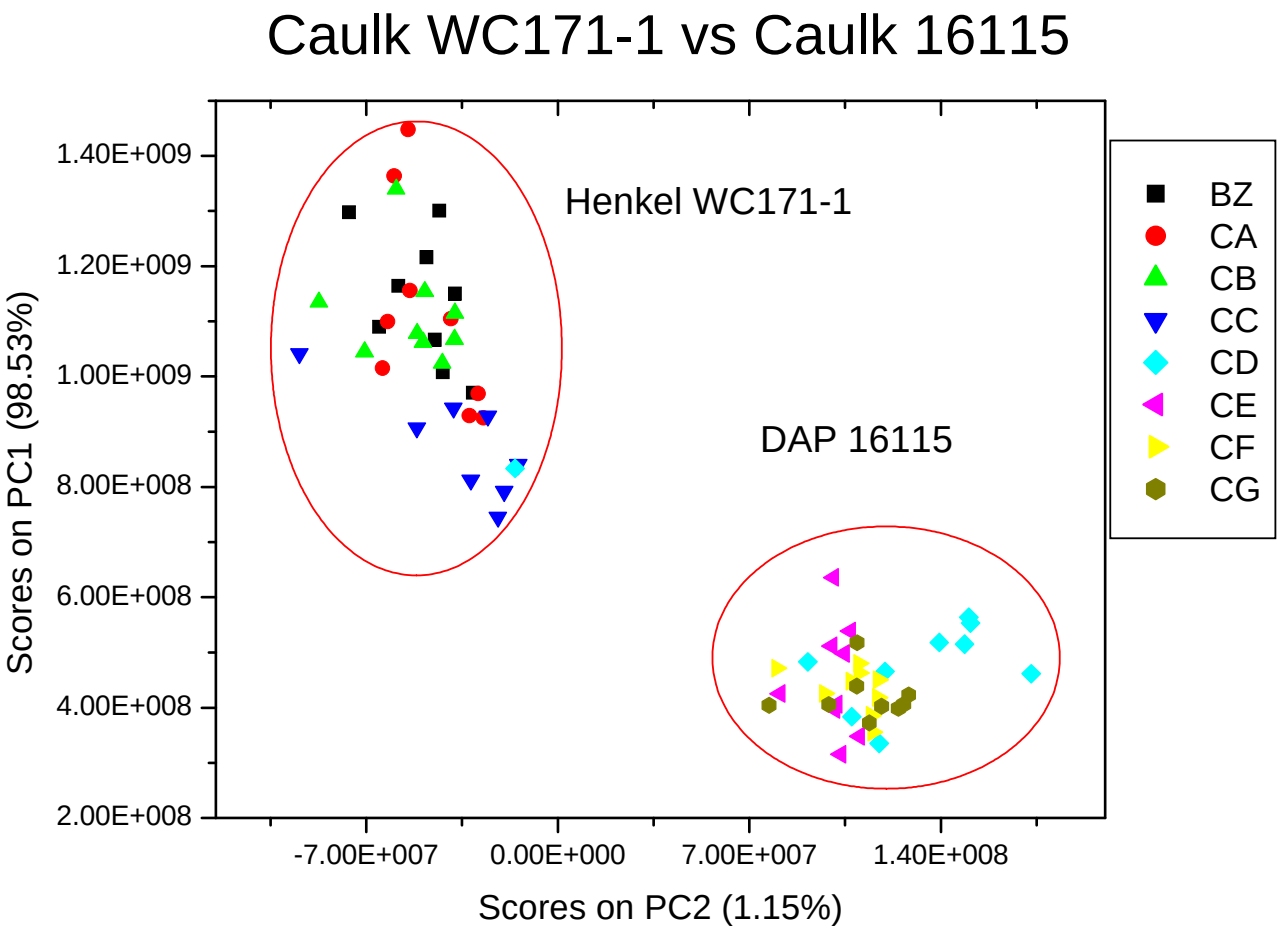

Figure 8
Comparison of lots from one manufacturer

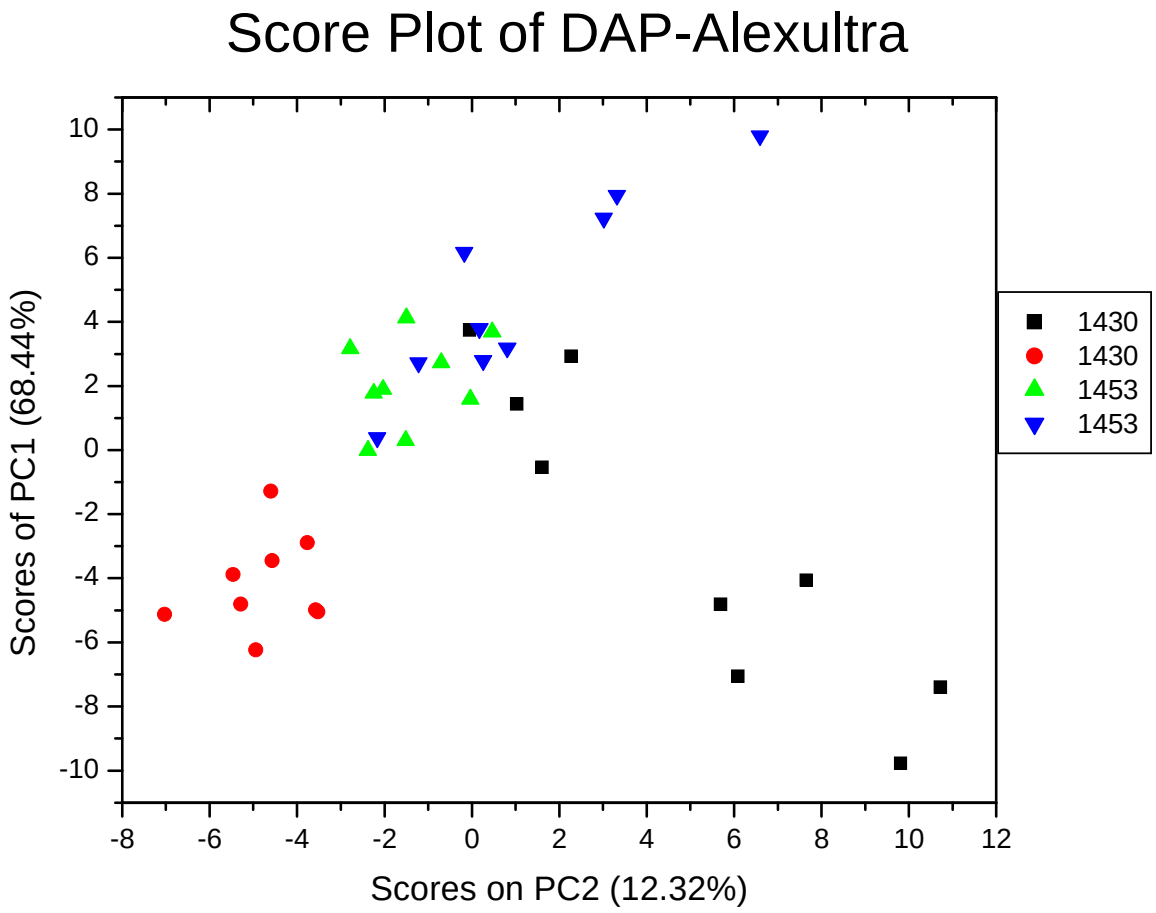

Determination of uranium isotope ratios in particle ensembles

Joshua Messerly, Stan Bajic, Nathan Saetveit, David Baldwin, R. S. Houk

Article prepared for submission to the Journal of Analytical Atomic Spectroscopy

Summary

Particulate ensembles were analyzed to determine their $^{235}U/^{238}U$ ratios. The particle ensembles were fixed in place to provide spatial resolution of particles of interest. Two methods of fixing particle ensembles in place were investigated. A gelatin substrate was used to fix U_3O_8 particles of for analysis. The $^{235}U/^{238}U$ ratios of these samples were determined to 2.9% RSD. The gelatin substrate was also used to fix particles of NIST 610 glass. A sample with the glass particles was also sprayed with a solution of vanillic acid in an attempt to enhance the ablation process. Particle ensembles were also fixed by being coated with collodion solution which was allowed to dry. Vanillic acid was also mixed with the collodion in a second solution. The vanillic acid was did not increase signal during the ablation of particulates on gelatin, but increased ablation signals when used in the collodion experiment.

Introduction

Laser ablation with inductively coupled plasma mass spectrometry (LA-ICP-MS) is a leading tool for analysis of solid samples. The ability to directly analyze a sample with a minimum of preparation is one advantage of this method. The use of LA-ICP-MS removes digestion and dilution steps which may add interferences and errors to the analysis.

One area of interest is to use LA-ICP-MS to analyze ensembles of particles that may be connected with nuclear weapons or dirty bombs. The possible acquisition or development of these types of weapons by terrorists or rogue nations is a real threat in our world today. Fast and accurate identification of possible evidence of these weapons is a needed tool to fight nuclear proliferation. Particle ensembles may be individually separated and dissolved for ICP-MS analysis, but this process is time consuming[1].

Samples of interest may be collected from ambient air on filter media or other means. Once collected and inspected, some particle ensembles may be suspected of containing uranium or other actinides. Accurate and precise isotope ratio measurements in these particles require that only the particle ensembles of interest are ablated and reach the plasma. Spatial resolution of the ensembles without disturbing the other particles present or the supporting matrix is needed to accomplish this.

Ensembles collected on filter paper may be ablated directly, but this presents a problem. The ablation event creates a shockwave that sends vibrations through the filter paper. The effect is similar to a trampoline. This vibration causes particle ensembles outside the ablation zone to bounce up into the carrier gas stream. These ensembles may then be entrained in the carrier gas and swept into the plasma. This leads to ensembles other than the one being ablated entering the ICP.

Pressing powdered materials into a pellet[2], attaching particles to double-sided sticky tape, and mixing the material with a binder are all ways preparing powdered samples for ablation. These preparation methods present problems for the analysis of an individual ensemble of a few particles. Ablation of a pellet does not allow for enough spatial resolution to analyze individual particle ensembles. This is also true of a sample mixed with a binder. Double sided sticky tape may allow individual ensembles to be ablated, but damage to the tape may occur. This may cause ensembles other than the

ensemble of interest to become entrained in the carrier gas. Volatilization of the tape adhesive and melting of the plastic substrate around the ablation site can cause this damage.

One current method of analysis for particle ensembles entails the removal of the particles of interest from the filter medium and suspending them in collodion. Once possibly radioactive material is identified, the particle is cut from the collodion and analyzed by thermal ionization mass spectrometry (TIMS)[3]. Secondary ion mass spectrometry (SIMS) has also been used to analyze particles removed from filter media[4]. These methods are both time and labor intensive. They also require significant manipulation of the sample.

Two methods of trapping particle ensembles for ablation are investigated here. The first method is to trap the ensembles on top of a gelatin based substrate. The second method is to trap the particles on filter paper media by applying a layer of collodion on top of the paper. The particles that were collected on the paper are then trapped by the nitrocellulose layer that is left on the paper.

Gelatin based substrates have been used previously to filter and trap biological materials such as spores[5]. The gelatin then serves as a growth medium for the trapped biological material. In this experiment, the sample powder is either sprayed or sprinkled onto gelatin based media to simulate the gelatin filtration apparatus. The gelatin has the advantage of being sticky; it also absorbs vibrations due to the shockwave produced by the laser ablation event.

Powdered uranium oxide samples containing ^{235}U in depleted, enriched and unknown abundances were analyzed as particle aggregates on the gelatin substrate. The depleted and enriched U_3O_8 samples were nuclear reference materials (CRMS U0002 and U030-A) obtained from New Brunswick Laboratory-USDOE as well as a commercial sample of U_3O_8. Uranium isotope ratios were also determined for NIST 610 ground to a powder with individual particles measuring between 5 and 300 μm. This was sprinkled onto a gelatin-based substrate. In an attempt to enhance the ablation process, the latter samples were

sprayed with a solution of vanillic acid in methanol. The vanillic acid has been shown to absorb at the laser wavelength of 266 nm, and has been shown to increase the ablation efficiency in previous work by Sharp *et al*[6]. It was thought that this extra absorption could possibly improve the precision and/or accuracy of these measurements.

The second part of this experiment used the NIST 610 glass powder on filter media. The particles were fixed onto the filter paper by pouring collodion solution over both and letting it dry. Vanillic acid was also dissolved in the collodion solution as an enhancement in later sets of experiments.

Experimental

Laser ablation was accomplished using a LSX-500 laser ablation system from CETAC Technologies. This system uses a homogenized beam Nd-YAG laser, frequency-quadrupled to a wavelength of 266 nm. The LSX-500 has variable spot sizes available through an adjustable aperture; the spot size was 100 μm in this experiment. The gelatin substrates were ablated with single laser shots on each particle ensemble. The collodion samples required 30 shots at each location. The shots were fired at a rate of 10 Hz. The collodion layer had to be ablated through before reaching the particles of interest. The laser parameters are shown in Table 1.

The first part of this experiment used a particle filtration coil first suggested by Guenther *et al*[7]. The coil was used with the experiments that analyzed U_3O_8. A 15.24 cm long, 20-gauge, stainless steel needle was coiled 4 times and placed in-line between the LSX-500 and the ICP-MS. The needle removed large particles from the ablated aerosol. This reduced the amount of large spikes seen in the transient signal. The coil was not used during the other ablation experiments. This was done in order to judge the effects of vanillic acid and particle entrapment independent of the particle filtration coil. The loss of

signal that accompanies the use of the coil would also adversely affect the measurement of ^{235}U in the NIST 610 powder.

The ICP-MS instrument used during ablation experiments was a ThermoFinnigan ELEMENT 1 ICP-MS. This instrument was operated in low resolution mode for maximum sensitivity. RF operating power of this instrument was set to 1200 W. Other instrumental parameters were optimized on a day to day basis for maximum stability. The instrumental parameters for the ELEMENT are shown in Table 1. The instrument was operated in analog mode for the analysis of U_3O_8 samples, while it was operated in counting mode for the lower uranium levels in the other experiments. For determination of isotope ratios from laser ablation, it was necessary to operate the magnet at a single magnetic field value while scanning the accelerating voltage and m/z transmitted through the electrostatic sector. In an attempt to get as many data points per unit time, the magnet settling time was set to 0.001 seconds instead of the default 0.300 seconds. The longer settling time was not needed as the magnet was kept at a single mass. The faster scanning of the electrostatic sector allows for around 4 data points per second to be recorded. Since laser ablation produces a transient signal, more data points help better define the transient peaks.

Portions of the three U_3O_8 samples were dissolved in a mixture of hydrochloric and nitric acids and then diluted prior to analysis. These solutions were then analyzed by ICP-MS. The ICP-MS used for the solution analysis was an Agilent 4500 ICP-MS device. The instrument was tuned for maximum stability and sensitivity. The RF operating power of this instrument was 1200 W. The operating parameters for the Agilent 4500 are shown in Table 1.

Particle ensembles were captured on a gelatin substrate composed of Knox brand “Gelatine” mixed with purified DI water. This food-grade gelatin is an inexpensive substrate which has a low background for U. The ratio used was about 0.8 g gelatin to about 4.5 mL of DI water in a plastic weighing boat. The samples were heated using an IR heating lamp and mixed with a cleaned plastic

utensil. Bubbles in the gelatin were skimmed off the surface with the utensil before the gelatin set. After cooling to room temperature, particle ensembles of U_3O_8 or NIST 610 glass powder were sprinkled onto the sample surface. The sample surface is sufficiently sticky that the particle ensembles adhere to the surface. The particles also embed themselves a short distance into the substrate. This increases the adhesion. The gelatin samples may be turned upside down and the particles do not fall off.

A particulate standard that was homogenous with regards to uranium was needed in this set of experiments. The U_3O_8 standards could not be used repeatedly due to the small amounts of sample available for these experiments; and the added regulations governing the safe handling of radioactive materials. When ground into a powder, the NIST 610 glass standard provided a surrogate for dust particle ensembles. The NIST 610 glass also contains 461.5 ppm of uranium. This relatively high concentration allows better detection of the ^{235}U isotope. A single NIST 610 glass wafer was ground using an agate mortar and pestle to create the powder. The agate mortar and pestle was first cleaned thoroughly with DI water and then cleaned with dilute nitric acid. The NIST 610 powder was used for the collodion experiments as well as the vanillic acid experiments on gelatin. A blank sample without NIST 610 powder or U_3O_8 particle ensembles was also prepared and analyzed with every analysis to account for the gelatin background. The gelatin background was usually at or very near the instrumental background level.

For a test of the enhancement effect of vanillic acid on ablation, a solution of vanillic acid (Fluka) in methanol was prepared and sprayed onto the sample surface by use of a PFA concentric nebulizer (Elemental Scientific, Inc). The adhesion of the particle ensembles to the gelatin keeps the particles in place during this process. As long as the solution is not allowed to pool significantly on the surface of the gelatin, the particles are not removed. The sample was sprayed with a solution containing 0.75 g vanillic acid in 15.06 g methanol. The sample was sprayed in a back and forth motion over the sample for three minutes. The methanol was allowed to evaporate overnight with the sample covered and placed in a clean

hood. A blank sample of the gelatin sprayed for the same amount of time and in the same manner was also prepared and analyzed.

Ensembles of NIST 610 glass particles were also sprinkled onto the surface of filter paper. Collodion solution was poured onto the sample and the paper was rotated so the solution would cover the area with the glass powder. This was repeated on another piece of filter paper that had powdered NIST 610 on it, but the solution of vanillic acid in collodion was poured onto the paper. To create the solution, about 0.76 g of vanillic acid was added to 16.05 g of collodion. This created a saturated solution with excess undissolved vanillic acid present. The solution was allowed to settle and the solution was decanted off the sediment. Two blank filter paper samples were made without powdered NIST 610. One was created with collodion alone; the other had the collodion and vanillic acid solution.

Results and discussion

Isotope ratios were measured in three samples of U_3O_8. These samples contained different levels of $^{235}U/^{238}U$. Two samples were certified reference materials from New Brunswick Laboratory and contained $^{235}U/^{238}U$ at 0.017% and 3.00% respectively. The third sample was a commercial sample of U_3O_8 with no certified isotopic information. The solution analysis results are shown in Table 2. The measured $^{235}U/^{238}U$ values of the NRMs are in agreement with the NBL certified values. The $^{235}U/^{238}U$ value for the lab sample is 0.22%, indicating that this sample is depleted in ^{235}U. A commercial ICP standard solution of 10 ppb uranium was also analyzed for comparison and yielded a $^{235}U/^{238}U$ value of 0.72%. The literature value for $^{235}U/^{238}U$ in natural uranium is 0.725%.

After the solution measurements were made, the solid U_3O_8 standards were analyzed on the gelatin substrate. The gelatin is seen to be a good substrate for laser ablation since particle ensembles can

be ablated without disturbing other particles near the site or far from it. An image of a gelatin substrate with dust particle ensembles is shown in Figure 1. The labeled ensemble is targeted for ablation. In the image shown in Figure 2, the particle has been ablated. The other particles are not disturbed by the laser shockwave.

Three replicates of ten shots per replicate were made. A representative time resolved intensity plot is shown in Figure 3. The spikes that appear on top of the base laser ablation signal are mainly due to the presence of large particles[9]. The coils filter out many, but not all large ablated particles. The instrument had to be operated in analog mode because the samples of pure U_3O_8 created large intensity ablation transients. A sample mass spectrum of peak intensity ablation of the enriched standard is shown in Figure 4. The intensity of the signal generated by pure U_3O_8 could be in excess of $1x10^9$ counts per second. If this was the case, the signal would begin to move out of the linear dynamic range of the instrument. All shots that produced signals greater than $1x10^9$ counts per second were discarded because of this limitation.

Results of the analysis are shown in Table 2. The ablation results of the two standard samples of U_3O_8 showed agreement with their certified values and dissolved analysis values. The precision of the enriched standard was very good (2.9% RSD). The precision of the depleted standard was not as good at 9.6%. This may be due to the very small ratio in the depleted uranium. A spike in the ^{235}U signal would cause a greater proportional difference in the ratio of the depleted sample. The ablation results for the commercial lab sample show good precision and agreement with the solution measurement. The counting statistics of the ^{235}U signal in the depleted sample show that the best precision possible is 0.13% in this analysis. A plot of the measured ratio from the laser ablation experiment vs. the actual value (certified value or solution measurement) is shown in Figure 5.

The next part of this investigation focused on improving the ablation characteristics of this experiment further. It also focused on a second way of capturing and fixing particle ensembles. The standard used to simulate dust or other particulate ensembles was powdered NIST 610 glass. This glass has been found to have a uniform distribution of uranium, though the $^{235}U/^{238}U$ ratio of 0.2381% is somewhat depleted[8]. The instrument was run in counting mode for both masses so an unbiased ratio could be calculated. Instrumental parameters such as carrier gas flow rate and detector voltage were adjusted so that the ^{238}U signal would not overwhelm the detector in counting mode.

The samples of gelatin with NIST 610 glass were ablated with a coating of vanillic acid. The spray coated the surface of the gelatin and created a white coating around the NIST 610 powder on the surface of the sample. A sample of NIST 610 powder on gelatin with no coating was also ablated. The results from both coated and uncoated NIST 610 glass particles are shown in Table 3. Both analyses showed worse precision than the previous U_3O_8 experiments. The $^{235}U/^{238}U$ ratios from the coated and uncoated gelatin samples were also somewhat higher than the ratio given for the NIST 610 standard. The ^{235}U data was very close to the background, and this may be the reason why the values were off somewhat. Many fewer data points were calculated to have ^{235}U signal above the detection limit. The counting statistics for the ^{235}U data in both measurements gave an estimated precision of 1.5%.

The addition of the vanillic acid onto the sample did not improve the precision of the analysis. Both sample sets showed similar precision. A time resolved plot of ablation transients without vanillic acid and with vanillic acid is shown in Figures 6 and 7 respectively. The vanillic acid coated particles generally had lower intensity ablation transients than the ones that were not coated. Apparently the coating absorbed some of the laser radiation before it can ablate the particle ensemble of interest. Multiple laser shots may be needed to ensure the full ablation of the particle. This may cause a problem due to the particle possibly becoming fractured or driven farther into the gelatin by the initial laser shot.

Coating the particles with vanillic acid may not be needed if the particles are much smaller than the laser spot.

The collodion experiment used a different method of trapping and preparing the particle ensembles for ablation. The collodion experiments were done using a similar methodology as the gelatin experiments. Collodion samples made with vanillic acid were analyzed along with collodion samples that did not contain vanillic acid. The collodion samples required that the laser be fired 30 times to dig through the collodion layer before reaching the particle ensembles. This is similar to the method used to analyze fluid inclusions in geological samples[10]. Time resolved ablation plots of collodion without and with vanillic acid is shown in Figure 7 and Figure 8 respectively. The collodion experiments generally had higher ablation transients than the single shot analysis done on the gelatin samples. This is likely due to the extra shots on each particle ensemble.

Results for the collodion ablation are also shown in Table 3. This data shows a similar effect to the experiments done on the gelatin substrate. There was little effect on the precision of the analysis by using the vanillic acid over collodion alone. There was a 4 to 5 fold increase in signal from the samples that had vanillic acid dissolved in the collodion. This meant that more particles that were ablated had ^{235}U levels above three times the standard deviation of the background. Fewer data points were discarded because of this signal enhancement. This is a potential advantage since particles suspected of containing uranium may be of a limited number in a sample.

Conclusions

This study has investigated the ability of LA-ICP-MS to analyze discreet particle ensembles containing uranium. The gelatin substrate was investigated for its suitability in ablation of particle ensembles. It was found to be a useful tool for analysis of U_3O_8 ensembles while providing good

precision on a scanning ICP-MS device. The method of pouring collodion onto filter paper provided a second way to entrap and ablate particle ensembles. The ensembles were not as easily recognized for ablation as in the gelatin method, though. Larger transients are seen in the collodion experiments most likely due to more laser shots. Enhancement with vanillic acid is seen to increase ablation transients when mixed with the collodion. Enhancement is not seen in single shot ablation on the gelatin, due to the vanillic acid absorbing some of the laser radiation.

Acknowledgements

Ames Laboratory is operated for the U.S. Department of Energy by Iowa State University under Contract No. DE-AC02-07CH11358. This work was supported by the USDOE, Office of Defense Nuclear Nonproliferation, Office of Nonproliferation Research and Engineering, NA-22.

References

1. X. Z. Zhang, F. Esaka, K. T. Esaka, M. Magara, S. Sakurai, S. Usuda, K. Watanabe, *Spectrochim. Acta, Part B*, 2007, 62, 1130-1134.
2. Z. Stefánka, R. Katona, Z. Varga, *J. Anal. At. Spectrom.*, 2008, 23, 1030-1033.
3. S. Baude, R. Chiappini, Proceedings of Symposium of International Safeguards, Vienna, Austria, 2001.
4. G. Tamporini, M. Betti, V. Forcina, T. Hiernaut, B. Giovannone, L. Kock, *Spectrochim. Acta, Part B*, 1998, 53, 1289-1302.
5. K. Hess, in *Environmental Sampling for Unknowns*, CRC Press, Inc., Boca Raton, FL, 1996, pp. 52-54.

6. C. O'Connor, M. R. Landon, B. L. Sharp, *J. Anal. At. Spectrom.*, 2006, 22, 273-282.

7. M. Guillong, H. Kuhn, D. Guenther, *Spectrochim. Acta, Part B*, 2003, 58B, 211-220.

8. J. Kane, *Geostand. Newsl.*, 1998, 22, 7-13.

9. D. C. Perdian, S. J. Bajic, D. P. Baldwin, R. S. Houk, *J. Anal. At. Spectrom.*, 2008, 23, 235-335

10. D. Guenther, A. Audetat, R. Frischknecht, C. Heinrich, *J. Anal. At. Spectrom.*, 1998, 13, 263-270.

Table 1
Instrumental parameters

ICP-MS parameters for laser ablation
Tuned daily for best stability
Carrier gas flow rate – 1.00 to 1.200 L/min
Cool gas flow rate – 16.00 L/min
Auxiliary gas flow rate – 0.70 L/min
ICP-MS parameters for Uranium solution measurements
Tuned for best sensitivity and stability
Carrier gas flow rate – 1.00 to 1.10 L/min
Cool gas flow rate – 14 to 16 L/min
Auxiliary gas flow rate – 1 to 1.5 L/min
Laser ablation parameters
Frequency quadrupled Nd:YAG laser at 266 nm
Laser spot size – 100 μm
Laser repetition rate for collodion experiment – 10 Hz
Laser shots for collodion experiment – 30 shots

Table 2
Gelatin and solution analysis of U_3O_8 samples

	Laser Ablation Measurement $^{235}U/^{238}U$ % (RSD)	Solution Measurement $^{235}U/^{238}U$ % (RSD)	Standard Certified Value $^{235}U/^{238}U$ % (RSD)
Depleted U_3O_8 Standard	0.020 (9.3%) n=29	0.0176 (3.4%)	0.01755 (0.28%)
Commercial U_3O_8 Sample	0.23 (4.3%) n=29	0.23 (4.3%)	Not available
Enriched U_3O_8 Standard	3.15 (2.9%) n=30	3.11 (1.9%)	3.137 (0.064%)
Commercial 10 ppb U Standard		0.72 (5.6%)	

Table 3
Enhanced ablation results

	NIST 610* particles $^{235}U/^{238}U$ %	NIST 610* particles with vanillic acid $^{235}U/^{238}U$ %
Particles on gelatin	0.269 (14% RSD) n=18	0.257 (13% RSD) n=9
Particles on filter paper with collodion	0.238 (5.8% RSD) n=19	0.244 (5.6% RSD) n=28

*NIST 610 glass standard has a $^{235}U/^{238}U$ ratio of 0.2381%

Figure 1
Image taken before ablation of particle ensemble

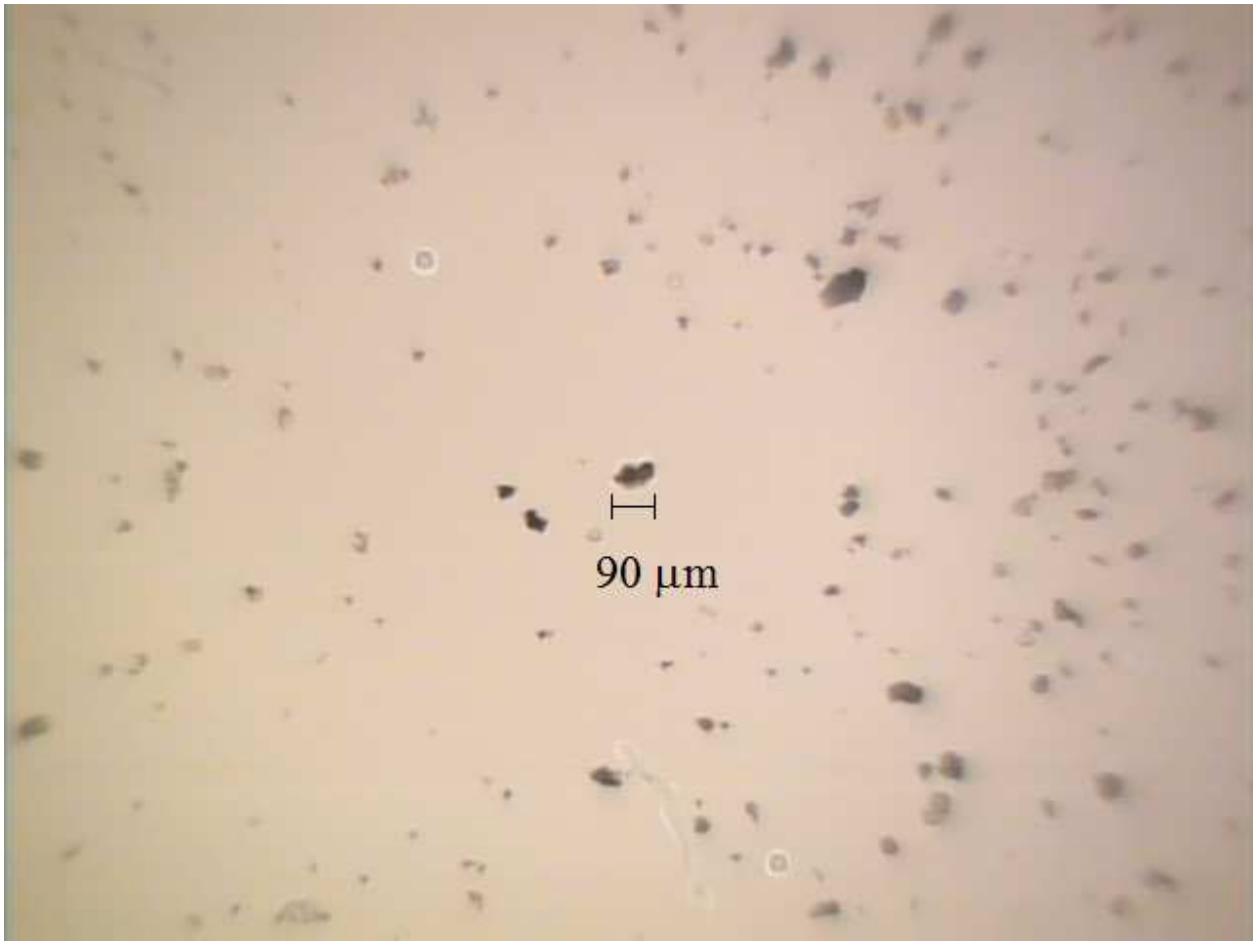

Figure 2
Image taken after ablation of particle ensemble

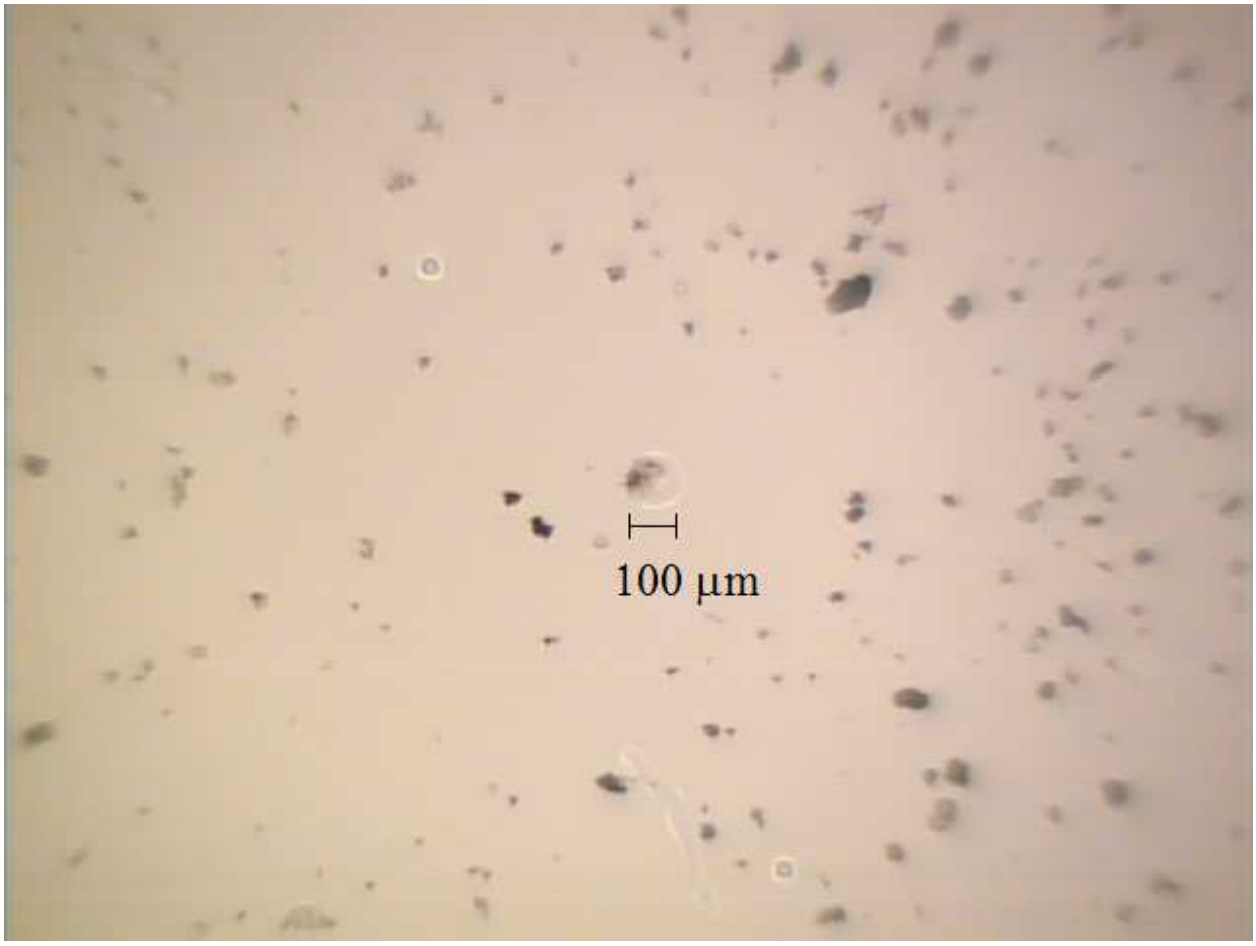

Figure 3
Time resolved plots of uranium oxide analysis

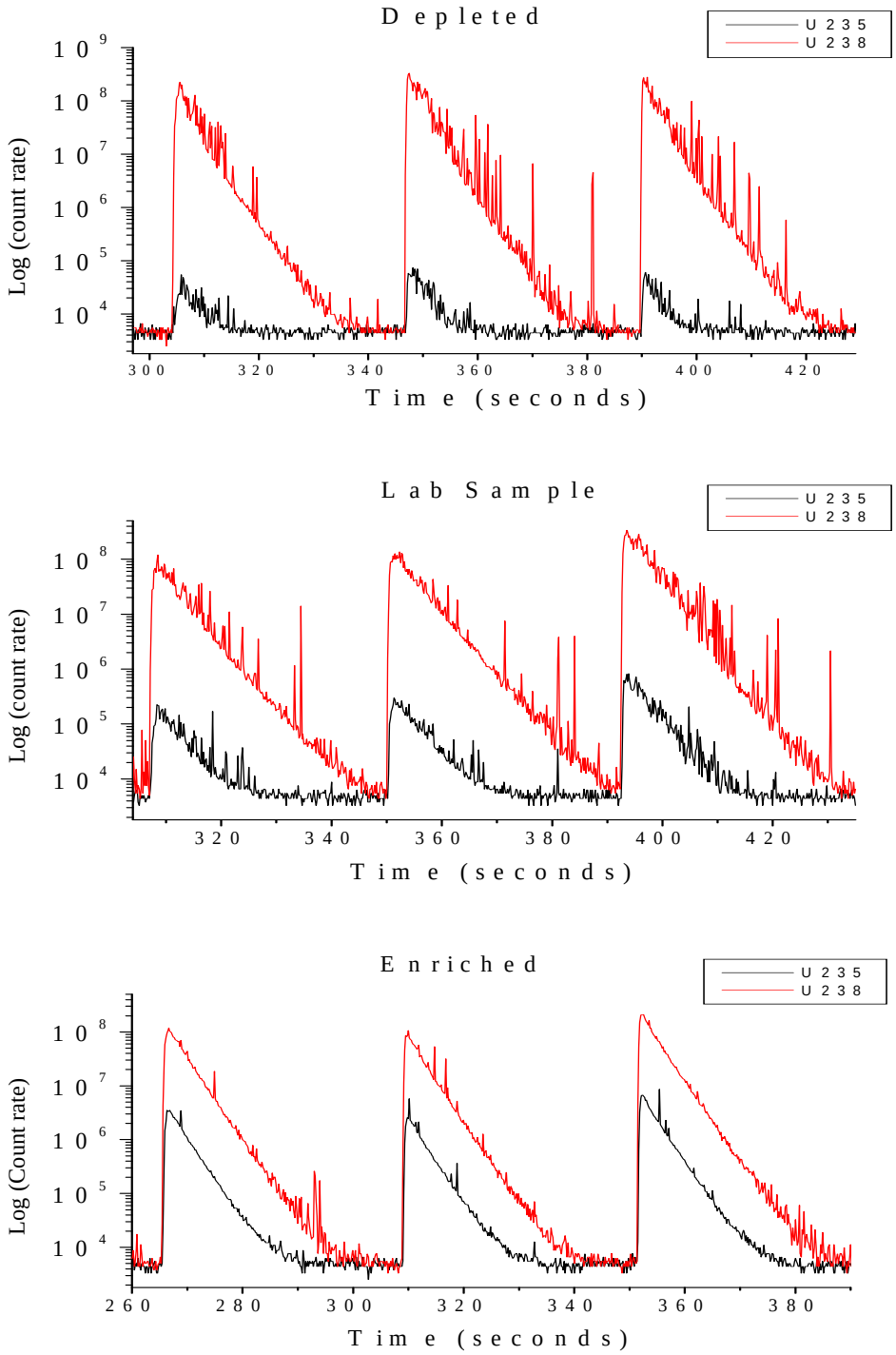

Figure 4
Sample spectrum at peak transient intensity for single shot ablation of a single enriched uranium particle ensemble on gelatin

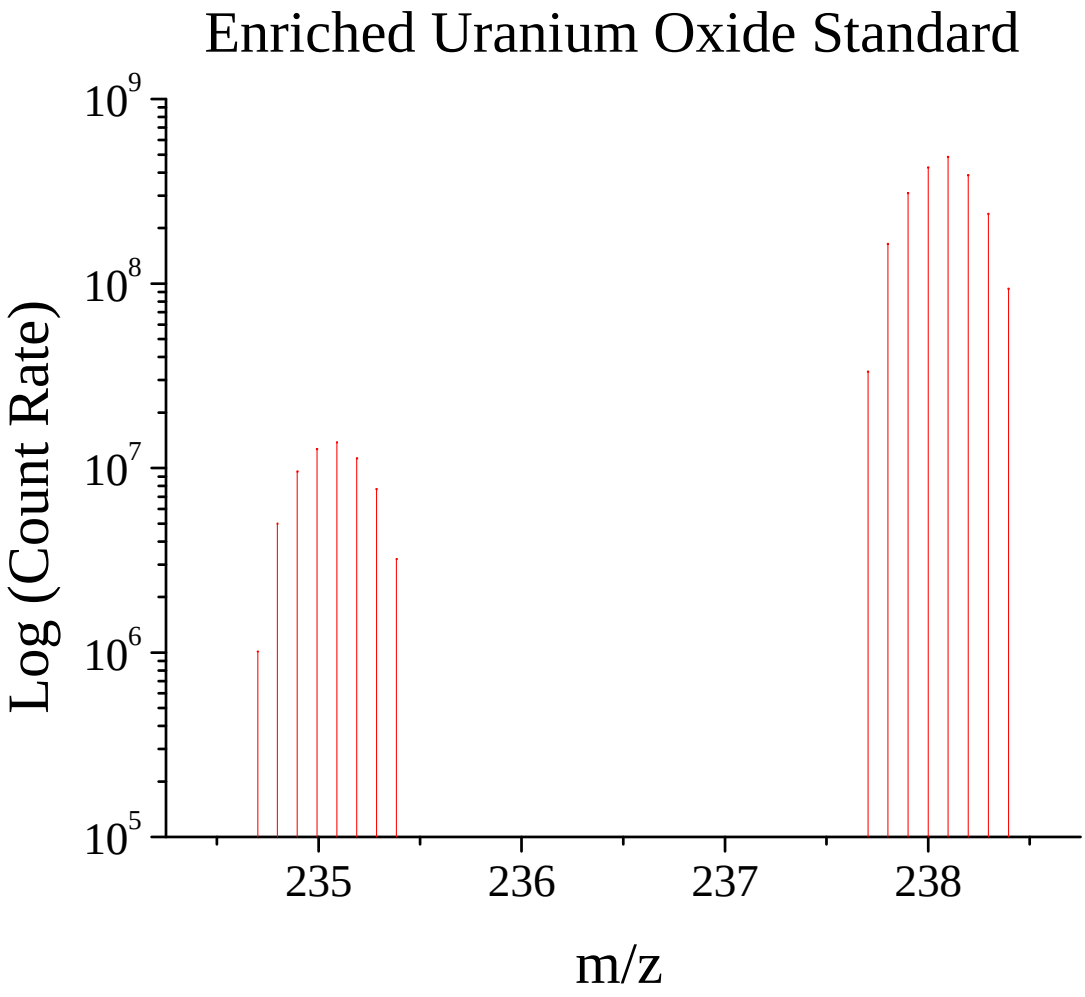

Figure 5
Plot of $^{235}U/^{238}U$ ratio determined by laser ablation vs actual $^{235}U/^{238}U$

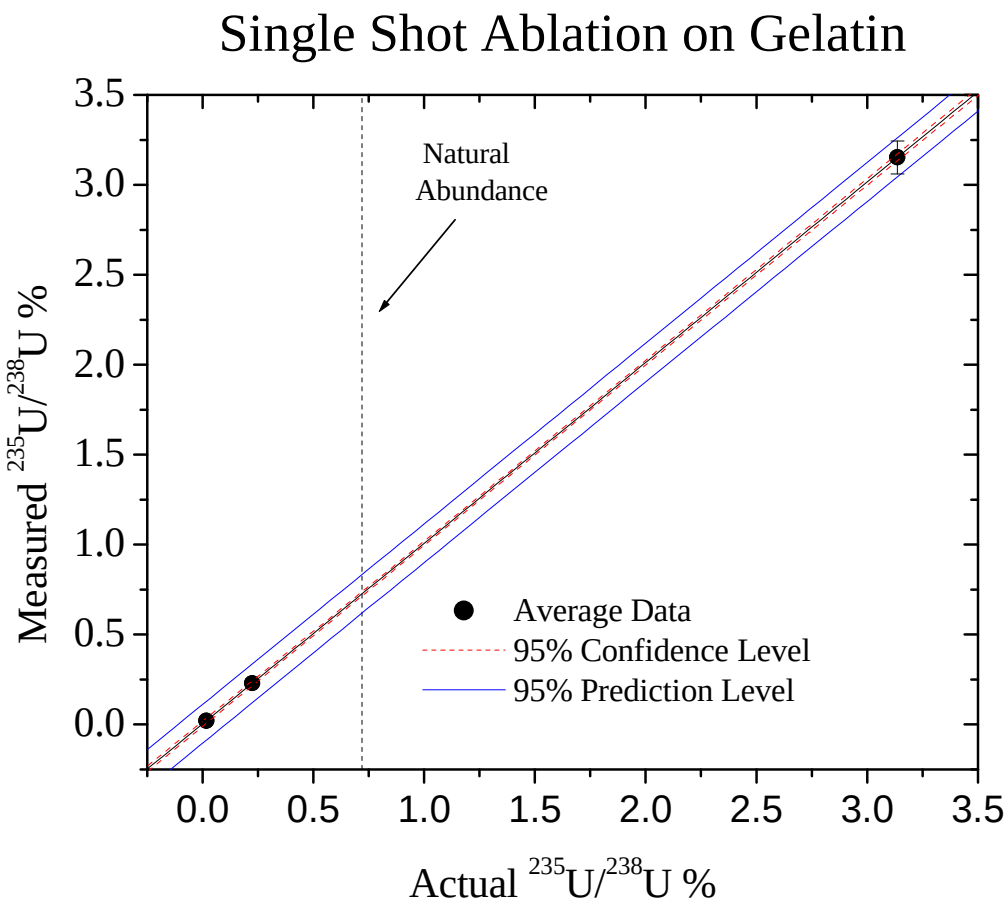

Figure 6
Plot of ablation transients on gelatin with no vanillic acid

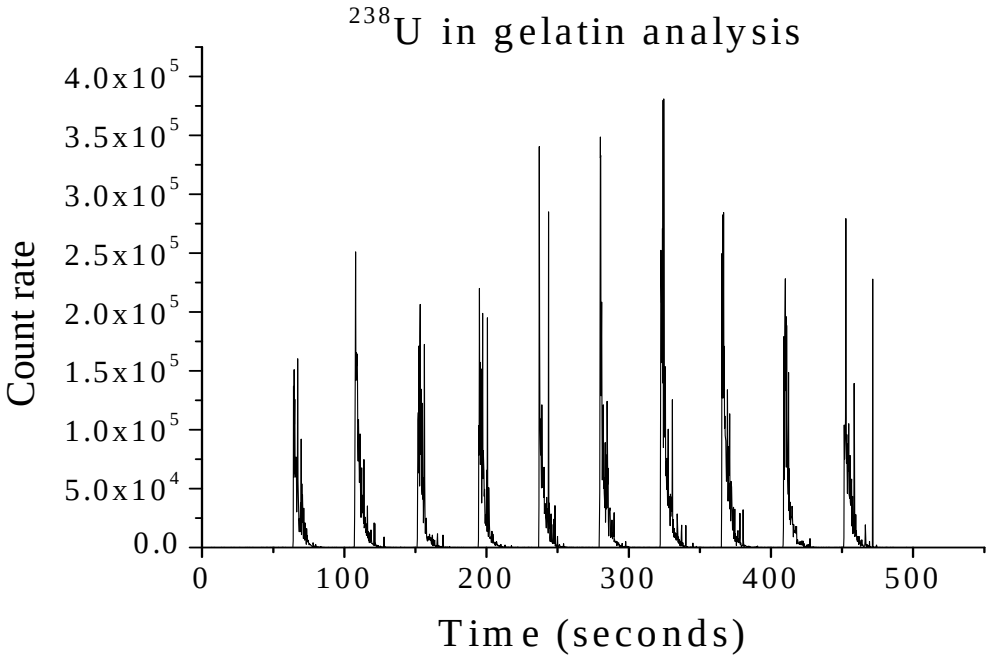

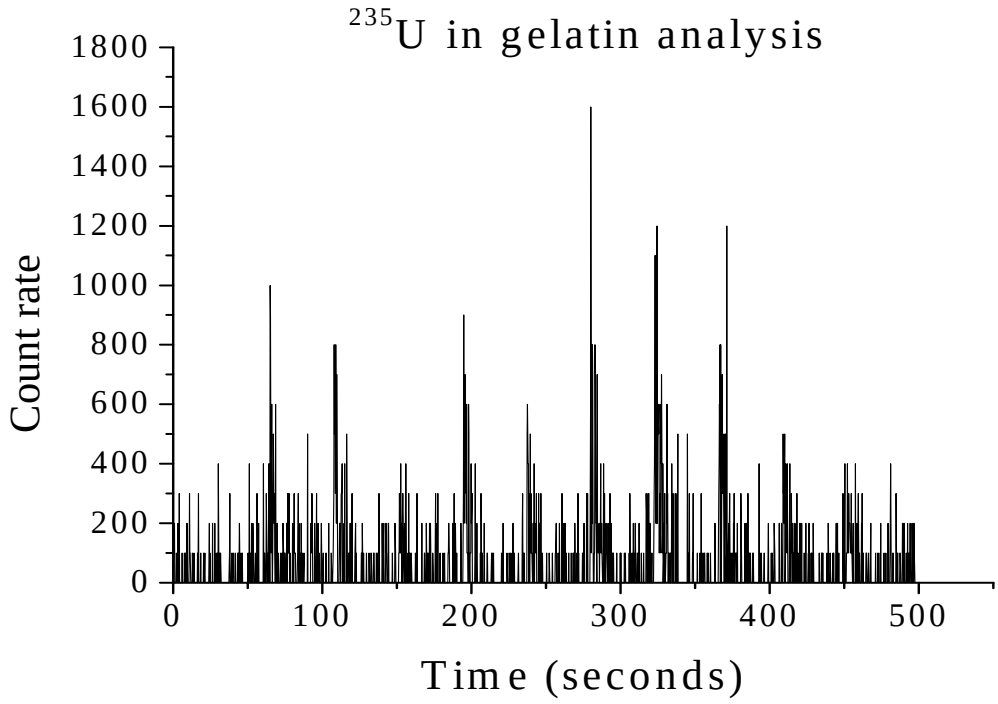

Figure 7
Plot of ablation transients of NIST 610 with vanillic acid on gelatin

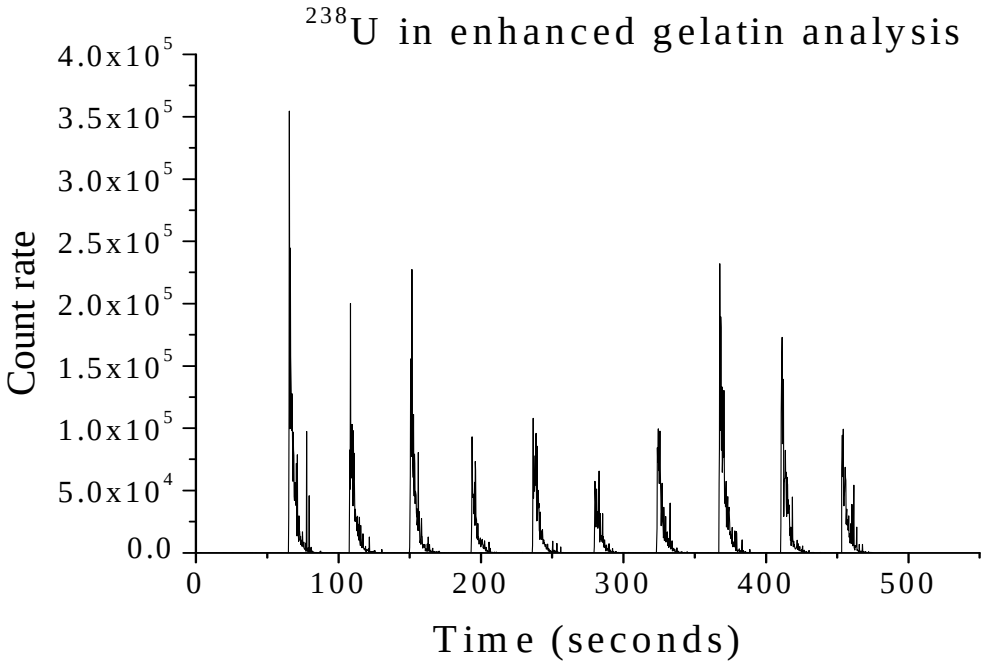

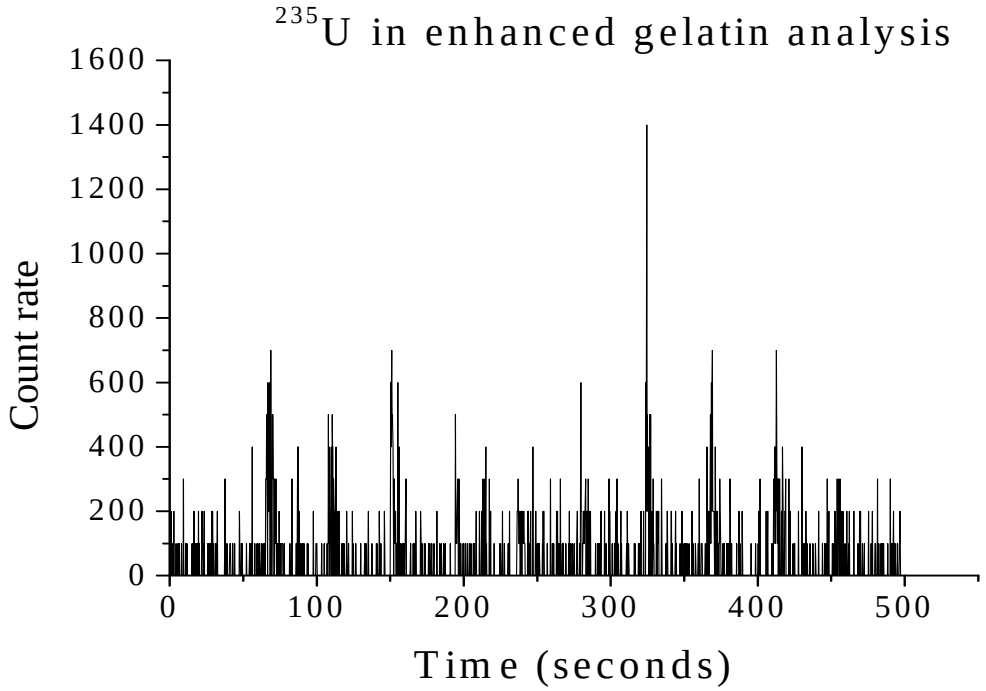

Figure 8
Plot of ablation transients of NIST 610 particles fixed in collodion without vanillic acid

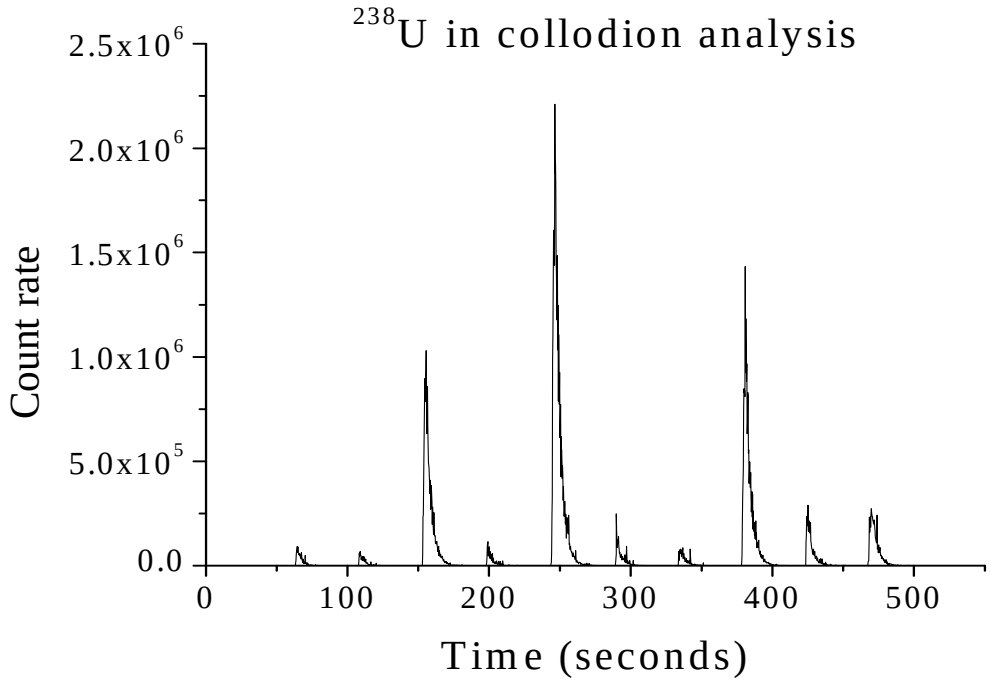

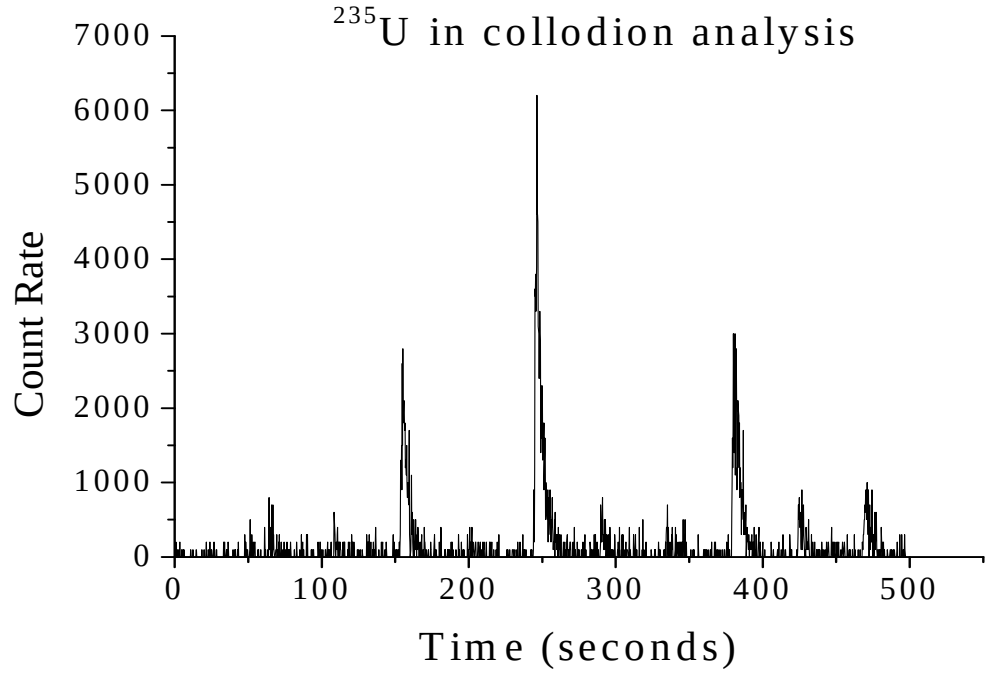

Figure 9
Plot of ablation transients of NIST 610 particles fixed in collodion with vanillic acid

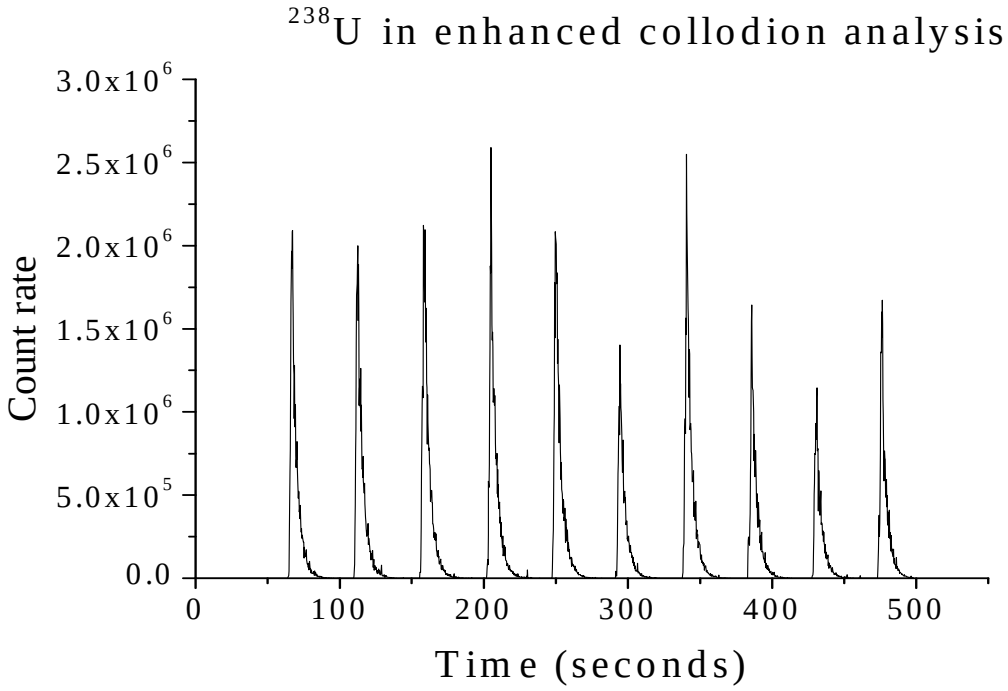

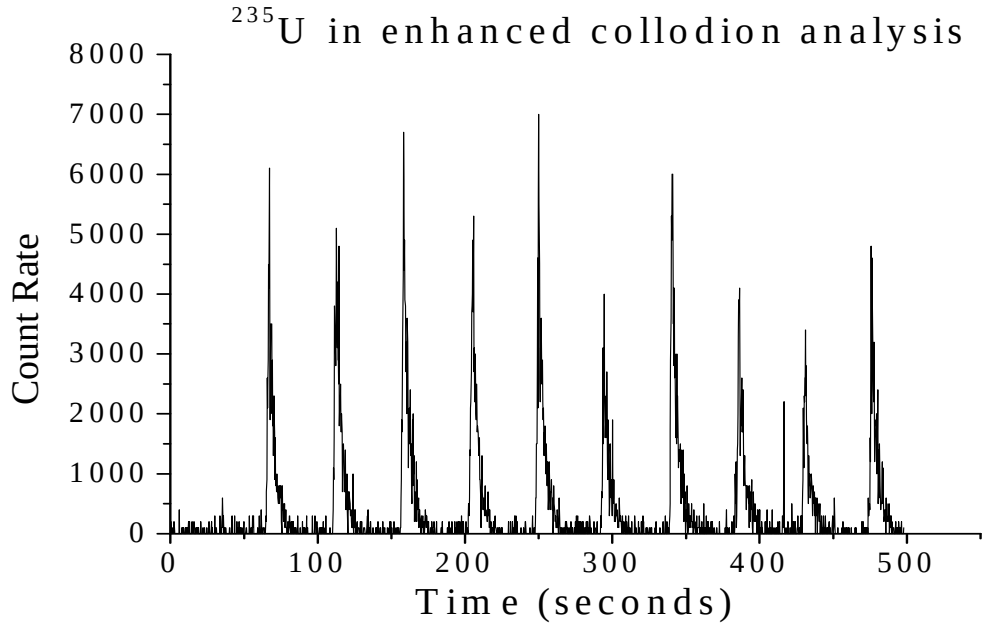

Chapter 5 – Conclusions

This dissertation focused on new applications of laser ablation inductively coupled plasma mass spectrometry (LA-ICP-MS). The diverse fields that were investigated show the versatility of the technique. In Chapter 2, LA-ICP-MS was used to investigate the rare earth element (REE) profiles of garnets from the Broken Hill Deposit in New South Wales, Australia. The normalized REE profiles helped to shed new light on the formation of deposits of sulfide ores. This information may be helpful in identifying the location of sulfide ore deposits in other locations. New sources of metals such as Pg, Zn, and Ag, produced from these ores, are needed to sustain our current technological society.

The application of LA-ICP-MS presented in Chapter 3 is the forensics analysis of automotive putty and caulking. The elemental analysis of these materials was combined with the use of Principal Components Analysis (PCA). The PCA comparison was able to differentiate the automotive putty samples by manufacturer and lot number. The analysis of caulk was able to show a differentiation based on manufacturer, but no clear differentiation was shown by lot number. This differentiation may allow matching of evidence in the future. This will require many more analyses and the construction of a database made up of many different samples.

The 4th chapter was a study of the capabilities of LA-ICP-MS for fast and precise analysis of particle ensembles for nuclear nonproliferation applications. Laser ablation has the ability to spatially resolve particle ensembles which may contain uranium or other actinides from other particles present in a sample. This is of importance in samples obtained from air on filter media. The particle ensembles of interest may be mixed in amongst dust and other particulates. A problem arises when ablating these particle ensembles directly from the filter media. Dust

particles other than ones of interest may be accidentally entrained in the aerosol of the ablated particle ensemble. This would cause the analysis to be skewed. The use of a gelatin substrate allows the ablation a particle ensemble without disturbing other particles or the gelatin surface. A method to trap and ablate particles on filter paper using collodion was also investigated. The laser was used to dig through the collodion layer and into the particle ensemble. Both of these methods fix particles to allow spatial resolution of the particle ensembles. The use of vanillic acid as a possible enhancement to ablation was also studied. A vanillic acid coating of the particles fixed on top of the gelatin substrate was not found to have any positive effect on either signal intensity or precision. The mixing of vanillic acid in the collodion solution used to coat the filter paper increased ablation signal intensity by a factor of 4 to 5. There was little effect on precision, though. The collodion on filter paper method and the gelatin method of resolving particles have shown themselves to be possible tools in fighting proliferation of nuclear weapons and material.

Future applications of LA-ICP-MS are only limited by the imagination of the investigator. Any material that can be ablated and aerosolized is a potential material for analysis by LA-ICP-MS. Improvements in aerosol transport, ablation chamber design, and laser focusing can make possible the ablation and analysis of very small amounts of material. This may perhaps lead to more possible uses in forensics. A similar method to the one used in Chapter 3 could perhaps be used to match drug residue to the place of origin. Perhaps a link could be made based on the elements leached from the soil by plants used to make drugs. This may have a specific pattern based on where the plant was grown. Synthetic drugs are produced in clandestine laboratories that are often times very dirty. The dust, debris, and unique materials in the lab environment could create enough variance to perhaps match drugs produced there to

samples obtained off the street. Even if the match was not strong enough to be evidence, the knowledge that many samples of a drug are being produced from a similar location could help law enforcement find and shut down the lab.

Future nuclear nonproliferation research would also be helped by the ability to get more analyte signal from smaller and smaller amounts of material. One possible future line of research would be to find a way to make the collodion layer as thin as possible so less laser shots are needed to get to the particle of interest. Collodion and gelatin analysis could also be used for environmental applications where spatial resolution of particles is needed. Individual particles could give information about the contaminants present in a given location. The wide versatility of LA-ICP-MS makes it a useful tool for nearly nondestructive analysis of a variety of samples and matrices.

ACKNOWLEDGEMENTS

This work was performed at Ames Laboratory United States Department of Energy; operated Iowa State University under Contract No. DE-AC02-07CH11358. This work was funded by the National Science Foundation, a Society of Economic Geologists Hugh E. McKinstry Student Research Grant, an Iowa State University College of Liberal Arts and Sciences Research grant, the United States Department of Justice, and the Midwest Forensics Resource Center. Additional support was provided by the United Stated Department of Energy, Office of Defense Nuclear Nonproliferation, Office of Nonproliferation Research and Engineering, NA-22.

I would like to thank Professor Houk for his patience and guidance during my time at Iowa State. Many thanks to the past and present Houk group members for their ideas and efforts to keep our instrumentation working. I thank my parents, siblings, friends, and my girlfriend Khara for their support during these years of work; and for knowing that I would finish when the finish line seemed distant. This dissertation is also dedicated to the memory of Darlene and Irvin Block, as well as Kay and John Messerly.